The Dissertation Committee for Maika Karen Gambús Ordaz Certifies that this is the approved version of the following dissertation:

A FIELD STUDY TO ASSESS THE VALUE OF 3D POST-STACK SEISMIC DATA IN FORECASTING FLUID PRODUCTION FROM A DEEPWATER GULF-OF-MEXICO RESERVOIR

Committee:

Carlos Torres-Verdín, Supervisor

Larry W. Lake

Robert Tatham

Sanjay Srinivasan

Kamy Sepehrnoori

A FIELD STUDY TO ASSESS THE VALUE OF 3D POST-STACK SEISMIC DATA IN FORECASTING FLUID PRODUCTION FROM A DEEPWATER GULF-OF-MEXICO RESERVOIR

by

Maika Karen Gambús Ordaz, B.S., M.Sc.

Dissertation

Presented to the Faculty of the Graduate School of
The University of Texas at Austin
in Partial Fulfillment
of the Requirements
for the Degree of

Doctor of Philosophy

The University of Texas at Austin

May 2005

Dedication

To my parents, brothers, and sisters
for everything they have given to me.
To my husband, for all the support, patience, and love,
and the loving memory of my mother-in-law, Maria Nicolasa de Hernández.

Acknowledgements

I would like to express my most sincere gratitude and appreciation to my supervising professor, Dr. Carlos Torres-Verdín. His patience, understanding, constant guidance, suggestions and his way to make me develop the research work have made my stay at The University of Texas at Austin a wonderful experience. I extend my appreciation to Professor Larry Lake for his comments and suggestions on this dissertation. Thanks also go to Dr. Kamy Sepehrnoori, Dr. Robert Tatham, and Dr. Sanjay Srinivasan for being part of the dissertation committee.

I am grateful to Centro de Información, Educación y Desarrollo S.A. (CIED) for awarding me a scholarship and to La Universidad del Zulia for giving me the opportunity to pursue doctoral studies at The University of Texas at Austin.

I would like to extend my gratitude to UNOCAL Corporation for releasing the data set reported in this dissertation and to Fugro-Jason and Schlumberger for their generous donation of the software used to carry out the post-stack seismic inversion and multiphase flow simulations, respectively. The work reported in this dissertation was partially funded by UT Austin's Research Consortium on Formation Evaluation, jointly sponsored by Anadarko Petroleum Corporation, Baker Atlas, ConocoPhillips, ExxonMobil, Halliburton, the Mexican Institute for Petroleum, Schlumberger, Shell International E&P, and TOTAL. The Schlumberger Foundation also provided partial support in the form of a fellowship.

I would like to thank my office mates at the Formation Evaluation Research

Group, especially to Omar Varela and Omer Alpak for their help in a great variety of ways.

My deepest appreciations go to Arturo Contreras and Omar Alan Vicencio for their valuable help at the crucial stages of the research work.

Finally, I want to express my heartfelt thanks to my friend Nelson Jaramillo who has been a source of great encouragement at all times and to my husband Rafael for his constant belief and his patience, friendship, and support. I am deeply obliged to my parents Angela Graciela y Jorge Eliécer for always believing in me and for pushing me to go ahead and not to give up, and to my brothers and sisters, Jorge Kewin, Jorge Luis, Mayra, and Anggie Karolina for their friendship and confidence. To all my family, I express my gratitude for their understanding during those times when I had to be far from them.

A FIELD STUDY TO ASSESS THE VALUE OF 3D POST-STACK SEISMIC DATA IN FORECASTING FLUID PRODUCTION FROM A DEEPWATER GULF-OF-MEXICO RESERVOIR

Publication No.________________

Maika Karen Gambús Ordaz, Ph.D.
The University of Texas at Austin, 2005

Supervisor: Carlos Torres-Verdín

This dissertation describes a study undertaken to appraise the reliability of spatially complex hydrocarbon reservoir models constructed with the use of 3D post-stack seismic amplitude data and well logs. Developments center about the interpretation of data acquired in an active hydrocarbon field in the deepwater Gulf of Mexico. The availability of measured time records of fluid production and pressure depletion provides an independent way to quantify the accuracy and reliability of several methods commonly employed to construct static reservoir models. We make use of geostatistical inversion to construct spatial distributions of porosity and permeability that simultaneously honor well logs and 3D post-stack seismic amplitude data. The constructed reservoir models are compared against models constructed with standard geostatistical procedures that do not make use of seismic amplitude data or else that use a simple statistical correlation between reservoir properties and seismic-inverted acoustic impedances. We perform multi-phase fluid-flow simulations to assess the consistency of the constructed reservoir models against the measured time record of flow rates of gas/water and shut-in well pressures. For the hydrocarbon field under consideration, the joint stochastic inversion of well logs and 3D post-stack seismic amplitude data consistently yields the closest match to dynamic measurements of fluid production and pressure depletion. Our study also compares the influence of petrophysical and rock-fluid parameters on the reliability and accuracy of the predicted fluid production against the influence of spatial variability of porosity and permeability.

Table of Contents

PROBLEM STATEMENT AND BACKGROUND INFORMATION

STATIC MODEL

DYNAMIC RESERVOIR MODEL

List of Tables

List of Figures

PROBLEM STATEMENT AND BACKGROUND INFORMATION

Chapter 1: Introduction

1.1 Problem Statement

The central goal of reservoir characterization is to provide as detailed as possible quantitative static and dynamic descriptions of a reservoir. To accomplish this goal, data acquired at different locations in the reservoir, with different lengths of spatial resolution, and obeying different types of physics, are integrated in a manner that is consistent with a geological framework. A large uncertainty in much of the data available to forecast reservoir performance stems from the fact that, in general, geological media exhibit a high degree of spatial variability. In addition, because of the high cost associated with the acquisition of subsurface measurements, fundamental petrophysical parameters such as permeability and porosity, are usually measured/estimated only at a few locations. Laboratory measurements of rock-fluid properties such as irreducible water saturation, wettability, capillary pressure, and relative permeability are even scarcer given their high cost and low reliability. The combination of significant spatial heterogeneity with a relatively sparse and small number of measurements leads to uncertainty about the values of inter-well petrophysical properties and, therefore, to uncertainty in predicting fluid production with time. Such an adverse situation is exacerbated by the nonlinear nature of the phenomena governing fluid production and pressure depletion in hydrocarbon reservoirs.

This dissertation is specialized to the analysis of a gas/condensate and oil field reservoir located in the deepwater Gulf of Mexico, offshore the coast of Louisiana. We pursue two specific objectives:

- To quantitatively integrate seismic amplitude data in the construction of static reservoir models and to assess the impact of such integration in the prediction of dynamic reservoir behavior after the onset of production.
- To quantify the effect of uncertainty in rock-fluid parameters on the predicted time record of fluid production, especially in relation to uncertainty in the spatial distribution of porosity and permeability.

To accomplish the above objectives, we consider three different statistical procedures to construct spatial distributions of reservoir porosity and permeability, namely,

(a) Sequential Gaussian simulation honoring well-logs,

(b) Collocated sequential Gaussian co-simulation honoring well-logs and linear correlations between seismic-inverted acoustic impedance and both porosity and logarithm of permeability, and

(c) A 3D geostatistical inversion procedure that simultaneously honors 3D seismic amplitude data and well logs.

1.2 Literature Review

To the author's knowledge, the first suggestion of the quantitative integration of 3D seismic data and well logs can be traced back to Journel and Huijbregts (1978).

However, in their first work, they only showed the methodology and basic concepts of geostatistics applied to mining problems.

Estimation of porosity based on regression formulas between well-log acoustic impedance and porosity was reported by Maureau and Van Wijhe (1979). They applied such regression formulas to infer spatial distributions of porosity from seismic-derived acoustic impedances.

Doyen (1988) cokriged average values of porosity at well locations with seismic attributes. This approach explicitly enforced the same spatial variability of seismic attributes to the estimated inter-well porosity. However, it was Haas and Dubrule (1994) who first provided a complete technical description of the method and who first presented experimental validation results. They suggested relating multiple realizations of acoustic impedance to petrophysical properties such as porosity and permeability. The ensuing estimation technique was referred to as geostatistical inversion. Debeye et al. (1996) presented a similar methodology to delineate sands and estimate reservoir properties based on geostatistical inversion for lithology and porosity.

Many authors have illustrated the methodology to generate petrophysical distributions by honoring simultaneously well logs and seismic amplitude data under a geostatistical framework (Pendrel and Van Riel, 1997; Torres-Verdín et al., 1999; Grijalba-Cuenca et al., 2000). However, these methods do not explicitly honor dynamic measurements such as oil and gas production.

Kelkar et al. (1996) presented a systematic procedure for integrating 3D seismic data and single-phase production data for reservoir characterization. Subsequently, Landa et al. (1997) described a mathematical procedure to estimate reservoir distributions of porosity and permeability indirectly linked to seismic amplitude data and dynamic fluid production measurements. Permeability distributions were computed deterministically based on the assumption of a linear relationship between porosity and logarithm of permeability. Landa et al.'s (1997) procedure considered different numerical approaches to solve the inverse problem, including gradient-based methods and simulated annealing. More recently, Varela et al. (2002) developed a global inversion algorithm for the estimation of inter-well elastic and petrophysical parameters using pre-stack seismic amplitude data and well logs. Varela et al.'s (2002) reservoir models are amenable to numerical simulation of fluid production. However, their algorithm was validated and tested only on synthetic data. More recently, time-lapse seismic data have been acquired and interpreted to gain insight to the dynamic behavior of producing hydrocarbon reservoirs (Al-Najjar et al., 1999; Merkel et al., 2001; Waggoner et al., 2002)

In this dissertation, we make use of the three strategies described earlier to construct stochastic realizations of spatial distributions of porosity and permeability. Subsequently, these realizations are subject to numerical simulation of multiphase fluid flow to assess their agreement with the measured time records of fluid production and pressure depletion. Rock-fluid and fluid properties are assumed the same for all of the cases. Therefore, discrepancies in the numerically simulated fluid production are attributed to the procedure employed to populate porosity and permeability in the inter-well region. Finally, we assess the variability and reliability of the constructed reservoir models by systematically quantifying the relative influence of the assumed seismic-petrophysical correlation parameters and rock-fluid properties on the simulated time records of fluid production. Such an exercise provides a methodology to quantify the relative benefits of post-stack 3D seismic amplitude data in reducing uncertainty compared to information necessary to constrain petrophysical variables and fluid properties.

1.3 Outline

This dissertation is divided into three major sections. The first section includes Chapters 1, 2, and 3. Chapter 2 is a brief review of the data set released for the purposes of this dissertation. It summarizes the information about the seismic survey, the acquisition parameters of the post-stack seismic data, well logs, and core data. Also, petrophysical analysis is performed to calculate effective porosity, permeability and fluid saturation. Chapter 3 formulates the inverse problem for integrating post-stack seismic and well logs, and to estimate spatial distributions of acoustic impedance.

The second section consists of Chapter 4, which makes use of geostatistical techniques to construct inter-well spatial distributions of petrophysical properties (i.e. porosity and permeability). The last section comprises Chapters 5, 6, and 7. Chapter 5 emphasizes the reservoir and fluid description, while Chapter 6 describes the numerical simulations performed in order to achieve the closest match between the time records of fluid production simulated for the statistical models generated in Chapter 4 and the measured time records of fluid production. In Chapter 7, a detailed study is undertaken to quantify the value of seismic data in the construction of reservoir models and to assess the impact of such models in the forecast of hydrocarbon production.

Finally, Chapter 8 summarizes the overall conclusions of this dissertation and provides recommendations for future research work.

Chapter 2: The Data Set and Petrophysical Analysis

The objective of this chapter is to describe both the geographical location of the hydrocarbon field under consideration, and the structural and stratigraphic framework. It also provides a detailed description of the available post-stack seismic amplitude data, well-logs, core data, and ancillary reservoir information (thickness, average properties). Finally, a petrophysical study is undertaken to estimate effective porosity, permeability, and fluid saturation.

2.1 The Data Set

This dissertation is specialized to the analysis of a gas/condensate and volatilized oil field reservoir located in the deepwater Gulf of Mexico, offshore the coast of Louisiana.

Figure 2.1 is a plan view of the spatial coverage of the 3D post-stack seismic data. Well locations are overlain on a color-coded seismic RMS (root-mean-square) amplitude map calculated across the main flow unit in the reservoir. The areal coverage of Figure 2.1 is 3.14 Km^2 (778 acres), included in a 6.25 Km x 3.99 Km seismic cube. A total of 183 cross-lines and 122 in-lines constitute the available seismic data over the area of study. The 3D post-stack seismic data consist of traces sampled at 4 ms in the frequency band between 10 and 60 Hz, with a central frequency of 28 Hz (Table 2.1).

The zone of interest is located between 8860 ft (2700 m) and 9830 ft (2996 m) below the sea bottom (the average seawater column is 176 ft). Geological and geophysical interpretation was performed on the 3D seismic amplitude data. Numerous areas of bypassed hydrocarbon potential were discovered as a result of this effort. A sealing fault separates the two segments of the main flow units in the reservoir, here referred to as GNP2RA and GNP2RB. Our study is focused to the west side of the fault that limits the GNP2RB reservoir. A total of 36 cross-lines and 15 in-lines constitute the available data set over an area of approximately 153 m^2 (38 acres) that includes the GNP2RB reservoir.

From well-log measurements, it is found that the average P-wave velocity is approximately 8404 ft/s (2562 m/s), whereupon the tuning wavelength is approximately equal to 75 ft (23 m). Since the thickness of the vertical hydrocarbon column ranges between 1100 and 1300 ft, it becomes immediately clear that post-stack seismic amplitude data have the vertical resolution necessary to identify individual sand units.

Exploration targets are Lower Pliocene upper slope sands interpreted as amalgamated channel deposits flanked by a salt dome. Reservoir sands are unconsolidated and amalgamated turbidite deposits, most likely pounded in an interslope basin on the southern flank of the salt dome. The reservoir is a structural closure with bounding faults radiating out from the salt dome. Due to the proximity of the salt dome, reservoir sands exhibit dip angles of up to 27° thereby making seismic amplitude preservation and well ties considerably difficult. Two exploratory wells and sixteen development wells were drilled after the initial discovery; however, only two of them, A8, and A9ST, were completed across the GNP2RB reservoir. Figure 2.2 shows the locations of wells A8 and A9ST superimposed on a cross-section of the 3D post-stack seismic amplitude data. In that figure, black lines identify the intersection of the two seismic horizons that mark the lower and upper boundaries of the GNP2RB reservoir.

2.2 Petrophysical Analysis

In order to estimate petrophysical parameters such as porosity, permeability, and water saturation across the GNP2RB reservoir, we performed standard calculations on the available well-log measurements. Table 2.2 is a summary of some basic petrophysical parameters measured and/or calculated from well logs.

An iterative procedure between density porosity, neutron porosity, and fluid saturations (gas, oil, and water) was used to calculate the effective porosity that agrees with rock-core porosity measurements. Figure 2.3 is a flow chart that schematically describes the use of density porosity, neutron porosity, and electrical resistivity measurements to estimate effective porosity and water saturation. The calculated porosity was derived assuming presence of sand, shale, and fluids (gas, oil, and water) via the equation (Bassiouni, 1994)

$$f = \frac{r_b - r_{ma} - V_{sh}(r_{sh} - r_{ma})}{S_w r_w + S_o r_o + S_g r_g - r_{ma}}, \qquad (2.1)$$

where f is the calculated porosity, r_b is bulk density, r_{ma} is matrix density, and r_{sh} corresponds to the density of pure shale. Moreover, r_w, r_o, and r_g represent water, oil, and gas density, respectively, while S_w, S_o, and S_g represent water, oil, and gas saturation, respectively.

In equation (2.1), V_{sh} corresponds to the volumetric concentration of shale (per unit rock volume) and is calculated from the gamma ray measurements through the formula

$$V_{sh} = \frac{GR - GR_{\min}}{GR_{\max} - GR_{\min}}, \tag{2.2}$$

where $GR_{\min}$ is the minimum gamma-ray reading across the cleanest sand and $GR_{\max}$ is the maximum gamma-ray reading (refer to Table 2.2). The density of hydrocarbons in equation (2.1) is estimated from the cross-over between matrix-corrected neutron porosity and density porosity (Bassiouni, 1994).

We used the Simandoux equation (Bassiouni, 1994) to calculate water saturation, i.e.,

$$S_w = C\frac{R_w}{f^2}\sqrt{\frac{5f^2}{R_wR_t} + \frac{V_{sh}}{R_{sh}^2} - \frac{V_{sh}}{R_{sh}}}\ , \tag{2.3}$$

where R_w, R_t, R_{sh} represent connate water resistivity, deep resistivity reading, and shale resistivity, respectively, and C is a constant equal to 0.405. Pickett plots (Bassiouni, 1994) were used to estimate the apparent water resistivity (R_{wa}). The electrical resistivity of connate water was estimated at 0.017 O-m. Figure 2.4 is a composite well-log display of wireline data acquired along well A8. The upper panels in that figure show, from left to right, the gamma ray log, the deep and shallow resistivity logs, the density log, the density and neutron porosity logs, and the compressional sonic log across the GNP2RB reservoir. Gas-bearing flow units are readily identified from the crossover between the density and neutron porosity logs. The thickness of the reservoir penetrated by the well is approximately 500 ft.

There is not a unique and straightforward method to estimate permeability from well logs. However, simple relationships between porosity and permeability exist for unconsolidated sands (Lake and Carroll, 1986). To estimate well-log permeability, we assumed a relationship between porosity and irreducible water saturation similar to that of Tixier and Timur (Balan et al., 1995). Rock-core measurements were available to calibrate the estimation of permeability. The mathematical expression for permeability is given by

$$k = g \frac{f^{a}}{S_{wi}{}^{b}} , \qquad (2.4)$$

where g, a, and b are parameters calculated with a multiple regression analysis of rock-core laboratory measurements. In equation (2.4), k is the calculated permeability and S_{wi} is irreducible water saturation, here assumed constant and equal to 12%. The lower panels in Figure 2.4 show, from left to right, the gamma ray log, the calculated shale volume, the calculated permeability, the calculated porosity, and the calculated water saturation across the GNP2RB reservoir. Both reservoir porosity and permeability are relatively large (27% and 354 mD, respectively.)

Figure 2.5 is a cross-plot of porosity and logarithm of permeability. In that figure, the solid blue line represents the linear trend estimated from multiple regression analysis of the rock-core measurements, whereas the colored points correspond to actual rock-core measurements. The solid red line is included as reference and describes a 50%-perturbation of the rock-core trend to be subsequently used in this dissertation for sensitivity analysis.

2.3 Summary

This chapter presented a general description of the field data set and estimated petrophysical properties, such as effective porosity, permeability, and gas, oil, and water saturations. The next chapter introduces some basic concepts used for seismic modeling.

Table 2.1: Summary of acquisition parameters of the post-stack seismic data used in this dissertation.

SEISMIC ACQUISITION PARAMETER	**VALUE**
Number of in-lines and cross-lines	183 cross-lines x 122 in-lines
Subset of in-lines and cross-lines across the reservoir	36 cross-lines x 15 in-lines
Seismic time range	0 – 3.0 s
Time sampling interval	4 ms
Line Separation	24.6 m
Frequency Range	5 – 80 Hz
Central Frequency	28 Hz
Average compressional wave velocity	8404 ft/s

Table 2.2: Summary of the measured and calculated well-log data available for the study reported in this dissertation. Refer to the Nomenclature section for a definition of the variables listed in the table.

WELL	**GRmax gAPI**	**GRmin gAPI**	**f $_N$(sh) %**	**f $_D$(sh) %**	**R(sh) ohm-m**
A8	147.27	33.09	37.7	16.3	0.6
A9ST	89.19	34.85	40	16	1
A10ST	131.66	42.91	34.75	14.64	0.81
A11ST2	127.08	42.76	55.2	19.5	0.7
WELL	**R_t(ws) ohm-m**	**f (ws) %**	**R_{wa}* ohm-m**		**R_w(Pickett)* ohm-m**
A8	0.211	0.265	0.0182		0.0196
A9ST	0.211	0.27	0.0189		0.0173
A10ST	0.27	0.26	0.0225		0.0301
A11ST2	0.21	0.27	0.0189		0.0213

*Calculations performed without correction for temperature.

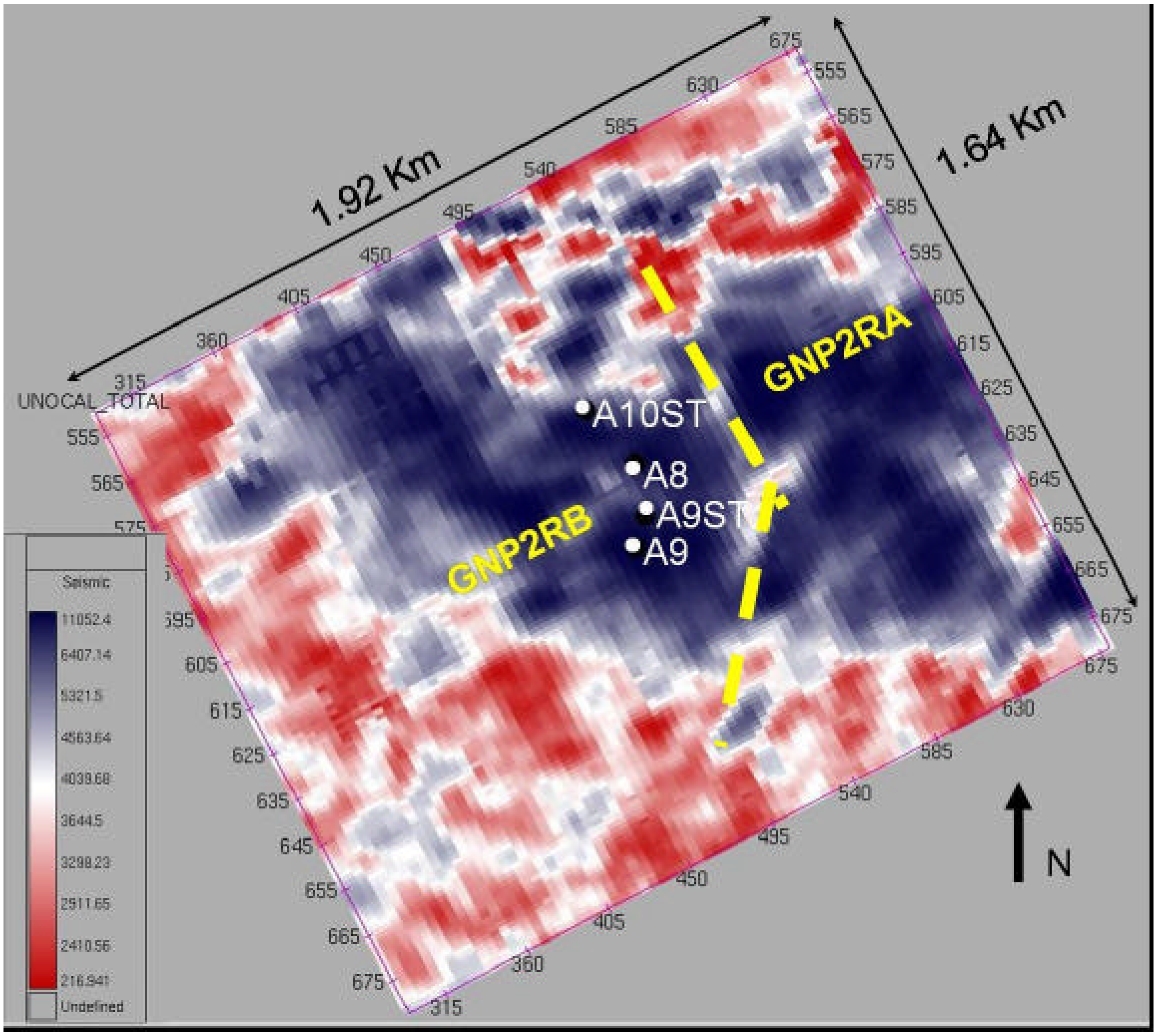

Figure 2.1: Plan view of the spatial coverage of the 3D post-stack seismic data. The figure shows the four well locations in white, superimposed to a color-coded seismic RMS (root-mean-square) amplitude map extracted within the seismic-time bounds of the main sand reservoir (GNP2RB). Dark blue and red describe high and low RMS seismic amplitudes, respectively. The dashed-yellow lines indicate the location of the sealing fault that divides the GNP2RA and GNP2RB reservoirs.

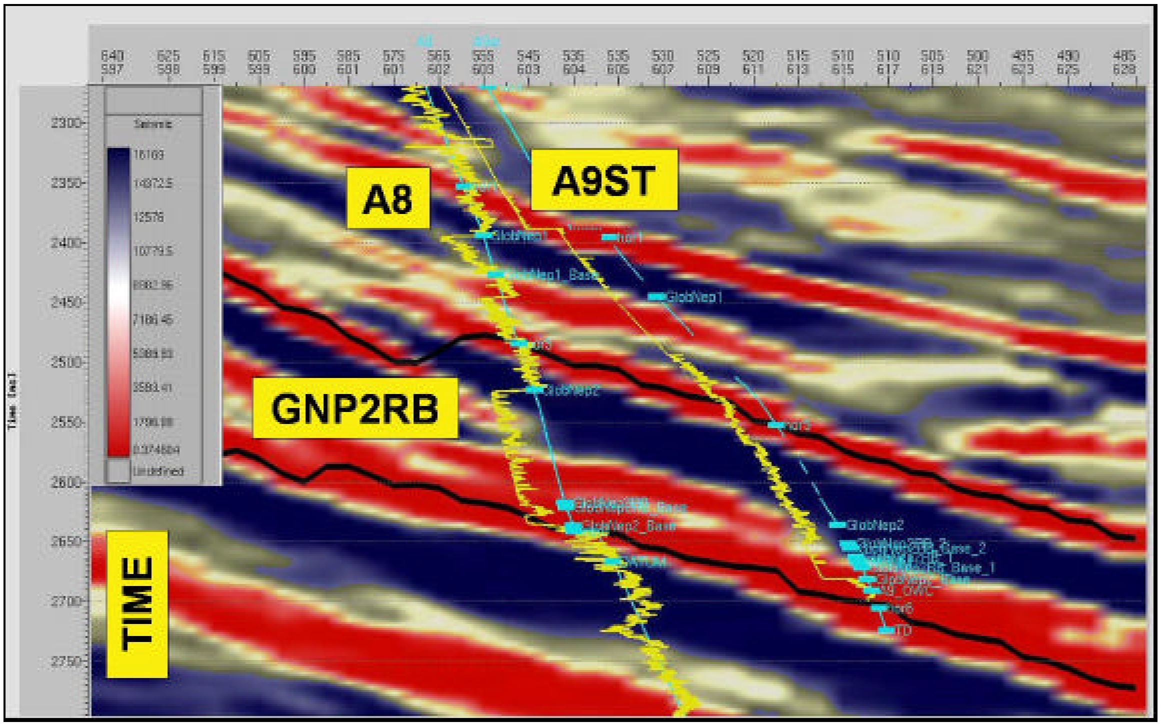

Figure 2.2: Cross-section of the post-stack seismic data showing the trajectories (light blue) and gamma-ray logs (in yellow) of two of the wells (A8 and A9ST) that penetrate the GNP2RB reservoir. The black lines describe seismic horizons that define the upper and lower boundaries of the GNP2RB reservoir.

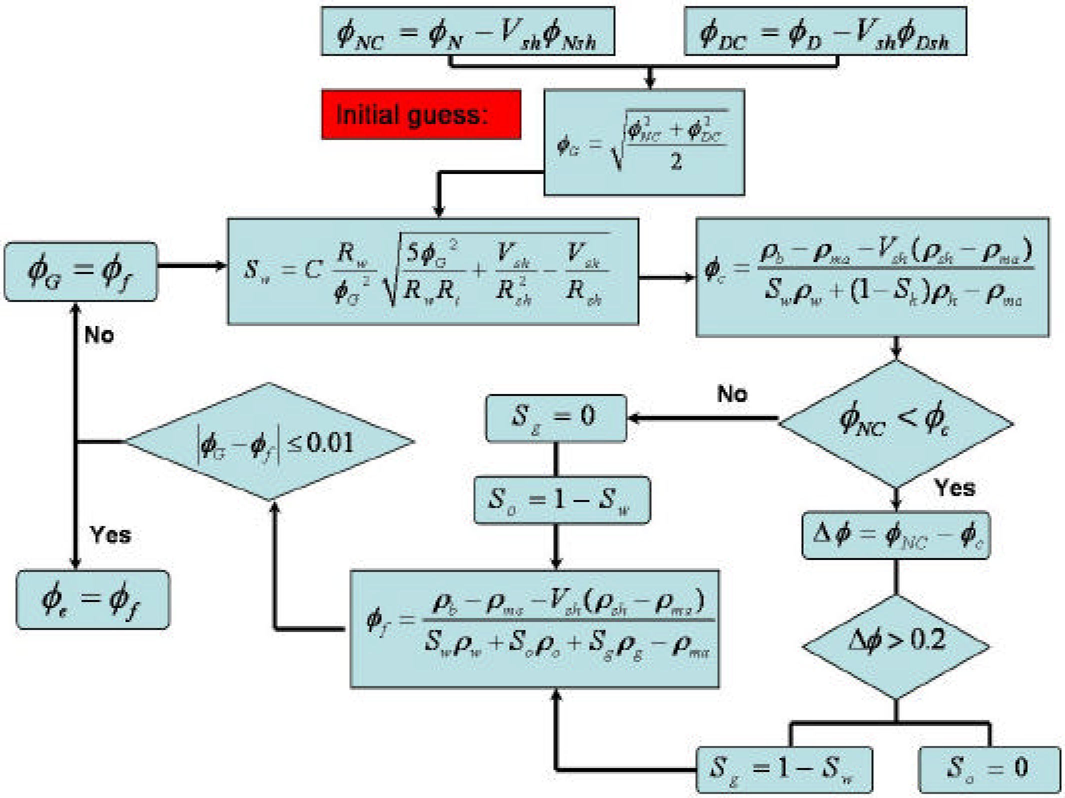

Figure 2.3: Flowchart describing the iterative method used in this dissertation to estimate effective porosity and fluid saturations (water, gas, and oil) from well logs. The process is initialized with an estimate of effective porosity obtained from shale-corrected neutron porosity (sandstone matrix) and shale-corrected bulk density logs. Water saturation is calculated with the Simandoux shaly-sand saturation equation. Subsequently, porosities are calculated from bulk-density logs using an expanded relationship between density and porosity that includes the effect of shale concentration and water saturation. Hydrocarbon densities are calculated from the cross-over of shale-corrected neutron porosity and the previous estimate of porosity. The calculated hydrocarbon densities are then substituted into a more general relationship between bulk density and porosity that includes fractional hydrocarbon saturations, thereby yielding a new estimate of effective porosity. This process is repeated until no significant changes are found in the estimated values of effective porosity and fluid saturations. The iterative process above does not consider the presence of mud-filtrate invasion and neglects differences in radial length of investigation and vertical resolution of the various well-log measurements involved in the calculation.

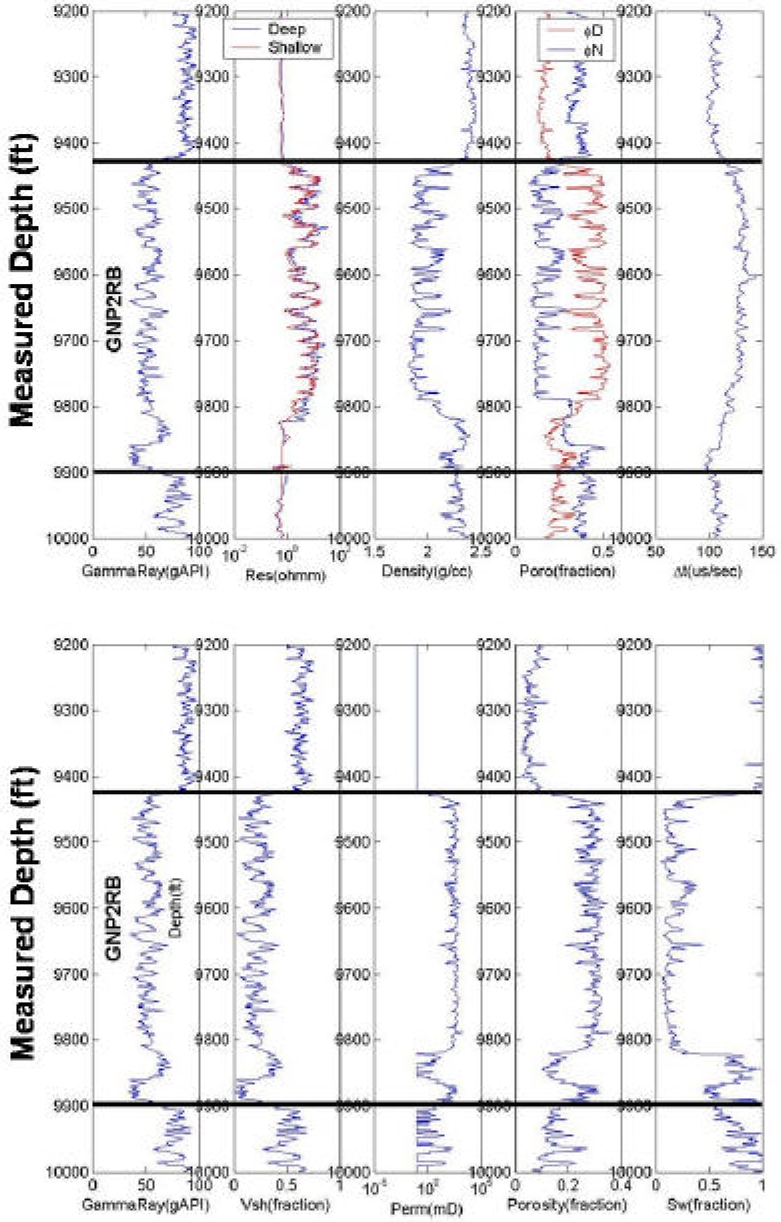

Figure 2.4: Description of the well-log measurements in well A8 and their petrophysical interpretation across the GNP2RB reservoir. From left to right, the upper panels describe the gamma ray, deep and shallow resistivity, bulk density and neutron porosities, and P-wave slowness. The lower panels describe, from left to right, the gamma-ray log, the calculated shale volume, the calculated permeability, the calculated porosity, and the calculated water saturation.

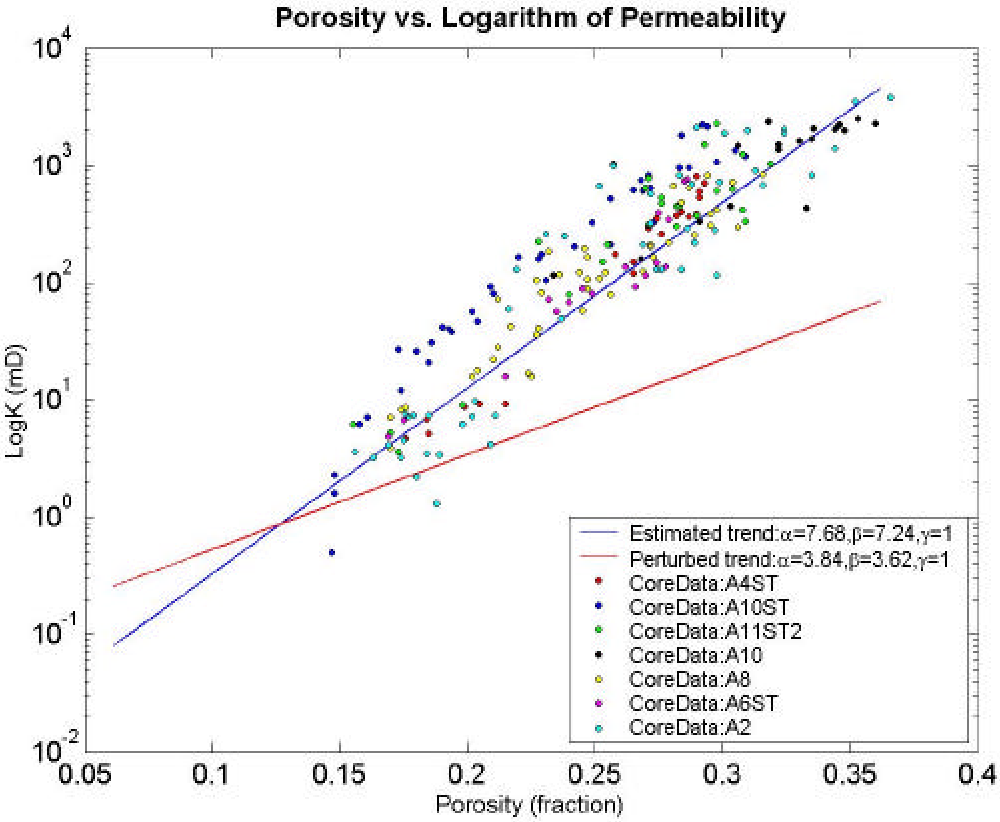

Figure 2.5: Cross-plot of porosity and logarithm of permeability constructed with rock-core laboratory measurements. The solid blue line describes the linear trend inferred from regression analysis, while the solid red line describes a 50%-perturbation trend used to assess the sensitivity of the linear correlation to the length of support of the rock-core measurements (Sensitivity Analysis No. 3; refer to case GI-5 in Table 7.1).

Chapter 3: Seismic Modeling

This chapter describes the inverse problem considered through this dissertation, as well as the method to transform seismic amplitude data to acoustic impedances.

3.1 Formulation of the Inverse Problem

Much has been written and many case histories published describing the utility of seismic amplitudes for detecting gas accumulation, channel sands, stratigraphic traps, etc. While the analysis and interpretation of seismic amplitudes have great merit, it is difficult to integrate them directly into reservoir models for engineering purposes, such as for flow simulations and volumetric calculations. Therefore, a method is required for converting these aggregate seismic amplitude responses into underlying layer properties. Such a method is referred to as seismic inversion (Bashore et al., 1993), and consists of estimating acoustic impedance (the product of bulk density and P-wave velocity) from variations of seismic amplitude as a function of vertical travel time.

3.2 Numerical Simulation of Post-stack Seismic Data

Inversion requires some form of constraint for stabilization due to both presence of noise and non-uniqueness of the solution. The most basic and commonly used one-dimensional model to describe post-stack seismic data is the convolutional model, written as

$$s(t) = w(t) * r(t) + n(t)\,, \tag{3.1}$$

where t is two-way vertical travel time, $s(t)$ is the post-stack seismic trace sampled at a constant time interval, $w(t)$ is the scaled wavelet, $r(t)$ is the reflection coefficient, and $n(t)$ is additive noise. The reflection coefficient across an interface is related to acoustic impedance, $Z_p(t)$, through

$$r(t) = \frac{Z_p(t+\Delta t) - Z_p(t)}{Z_p(t+\Delta t) + Z_p(t)}\,, \tag{3.2}$$

where Δt is the time sampling interval,

$$Z_p(t) = \rho(t) V_p(t)\,, \tag{3.3}$$

$\rho(t)$ is bulk density and $V_p(t)$ is P-wave velocity. Well log curves are measured in depth but they are transformed to the seismic travel time domain using the information contained in checkshot tables. A valid checkshot table consist of at least vertical time and depth columns. Moreover, P-wave velocity logs are calculated from sonic logs.

Each trace in a migrated post-stack seismic cube is described with a one-dimensional relationship of the type given by equation (3.1). The first step in seismic inversion is to estimate the wavelet. For this purpose, acoustic impedances are calculated from well-log data and are subsequently transformed from depth to seismic two-way travel time. Comparison between the measured and numerically simulated seismic amplitudes provides a way to estimate the wavelet. Adjustments to the depth-time transformation are often necessary to achieve an acceptable tie between well logs and seismic amplitudes. In this dissertation, seismic wavelets were estimated for each of the wells that included acoustic impedance measurements. Figure 3.1 shows the wavelets estimated for the project.

The second step of the seismic inversion process is to use the estimated wavelet to estimate acoustic impedances.

3.3 From Seismic Amplitudes to Acoustic Impedance

The particular algorithm used in this study to invert acoustic impedances from post-stack seismic data is due to Debeye and Van Riel (1990), and is referred to as Constrained Sparse Spike Inversion (CSSI). Rather than solving directly for reflectivity coefficients, Debeye and Van Riel (1990) pose the solution of the inverse problem to yield band-limited acoustic impedances subject to time-dependent value-range constraints. Specifically, the inversion is posed as the minimization of the cost function

$$C[Z(t)] = \int \left[s(t) - w(t) * r(t) \right]^2 dt + l \int \left| r(t) \right| dt \, , \qquad (3.4)$$

subject to

$$a(t) \leq Z(t) \leq b(t) \, ,$$

where l is a user-defined regularization (stabilization) parameter and $a(t)$ and $b(t)$ are user-defined lower and upper bounds on $Z(t)$, respectively, enforced in the minimization process. In equation (3.4), the choice of an absolute value norm for $r(t)$ and a quadratic norm for the seismic misfit, $s(t) - w(t) * r(t)$, in the cost function is made to minimize Gibbs-type oscillations in $r(t)$ and, therefore, to reduce the effects of wavelet side lobes on the estimation of both $r(t)$ and $Z(t)$ (Oldenburg et al., 1983). The lower and upper bounds, $a(t)$ and $b(t)$, are determined from available well-log data, whereas the regularization parameter is chosen by trial and error inversions performed in the vicinity of well trajectories.

A specific problem arises in the inversion of seismic amplitudes into acoustic impedance: the lack of low frequency components in both the post-stack seismic data and the reflectivity function. Because of this, the inverted acoustic impedances do not exhibit a low-frequency component, or trend of compaction (the drift typically seen in P-wave velocity logs with increasing depth due to compaction). The only way to include the compaction trend in the inverted band-limited acoustic impedances is to interpolate it from the compaction trend measured along existing wells (Grijalba-Cuenca et al., 2000). Addition of the compaction trend to inverted band-limited acoustic impedances yields the so-called inverted total acoustic impedances. The latter can be thought of as a smooth version of the wireline acoustic impedance log that would otherwise be acquired in a vertical well drilled at a particular trace location in the seismic cube (Grijalba-Cuenca et al., 2000).

Figure 3.2 is a cross-plot of the pseudo-impedance logs extracted from the cube of seismic-inverted acoustic impedances along well trajectories and the actual acoustic impedance log measured in the same wells. The correlation coefficient is 0.84. Such a relatively high correlation between the inverted and actual impedance well logs suggests that seismic amplitudes are reliable to estimate inter-well acoustic impedance. It remains to ascertain whether acoustic impedance correlates with petrophysical properties.

Figure 3.3 is a 3D rendering of the area of study showing existing well trajectories superimposed on an inverted acoustic impedance time horizon computed from the RMS value of acoustic impedance across the GNP2RB reservoir. In the figure, the areal extent of the reservoir remains enclosed by structural faults as well as by stratigraphic boundaries; reservoir units coincide with anomalies of low acoustic impedance.

3.4 Summary

This chapter described the procedures and assumptions used in the dissertation to transform seismic amplitude data to acoustic impedances.

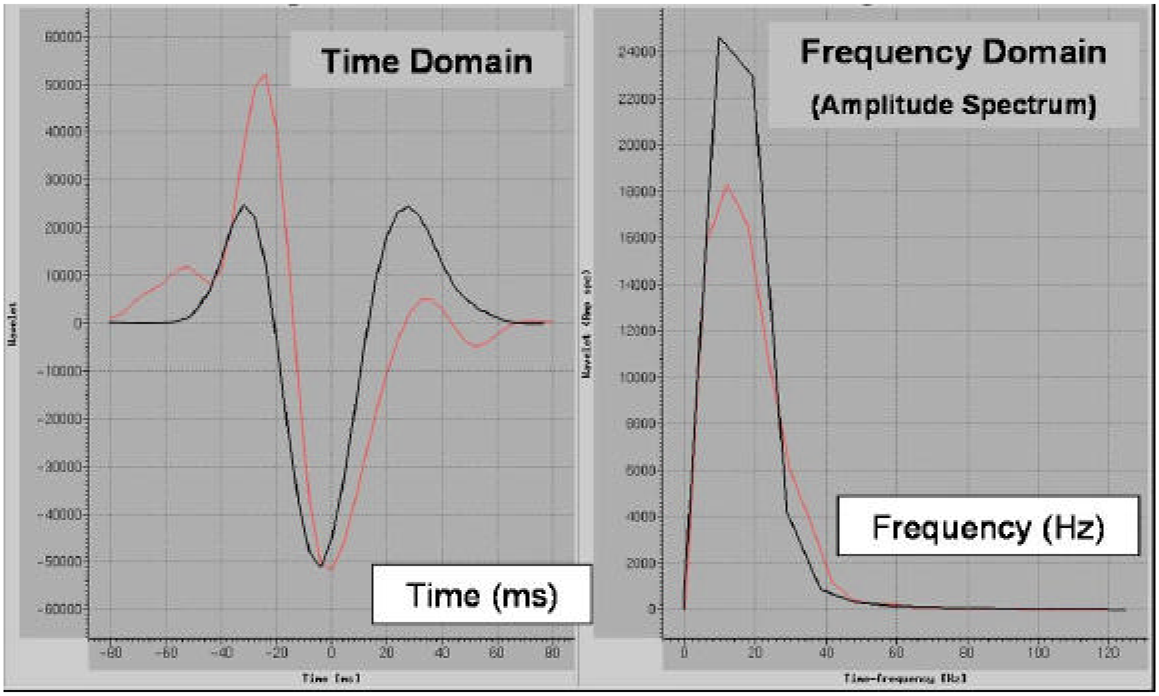

Figure 3.1: Plots of the time- and frequency-domain expressions of the estimated seismic wavelets from the post-stack seismic amplitude data. The solid black line describes the average wavelet estimated from wells that included density and P-wave velocity logs (A10, A10ST, A8), while the solid red line describes the wavelet estimated from density and P-wave velocity logs acquired in well A10ST only. The latter wavelet is used in conjunction with Sensitivity Analysis No. 6 (GI-11; refer to Chapter 7; Figure 7.9).

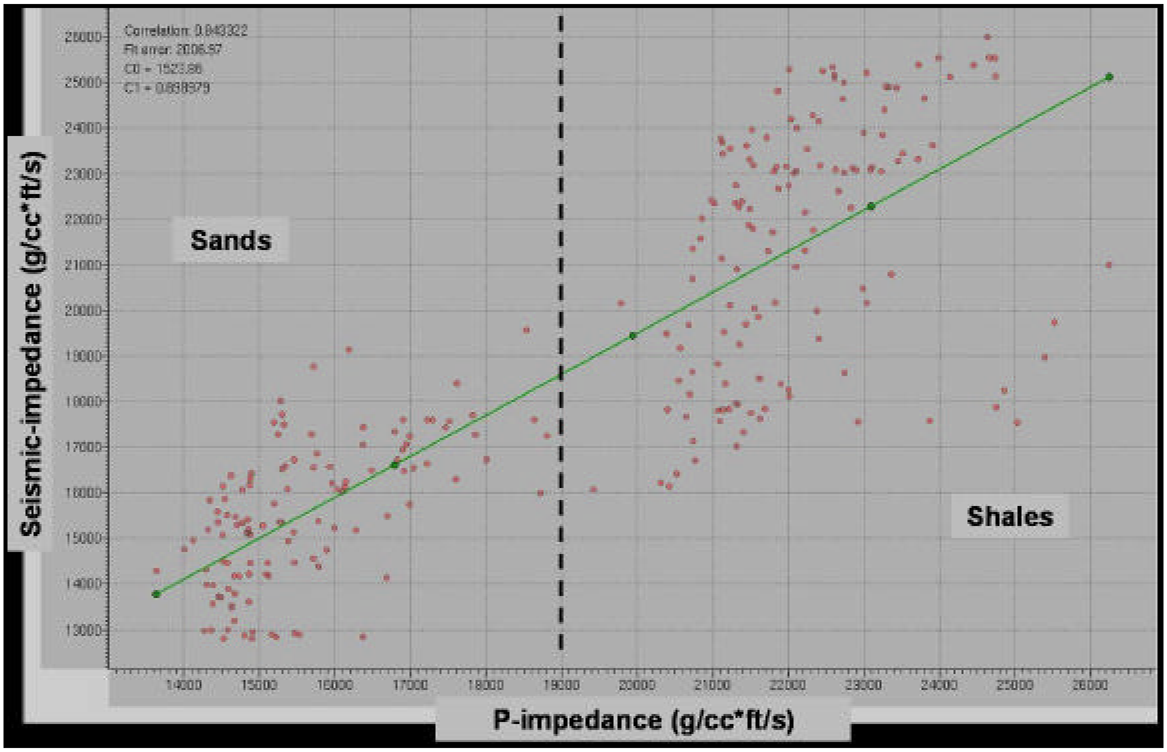

Figure 3.2: Cross-plot of the pseudo acoustic impedance (P-impedance) logs extracted from the seismic-inverted acoustic impedance volume and the impedance logs derived from the sonic and bulk density logs at wells A10st and A8. Wells A10st and A8 are the only ones that include well-log measurements of both bulk density and P-wave velocity across the GNP2RB reservoir.

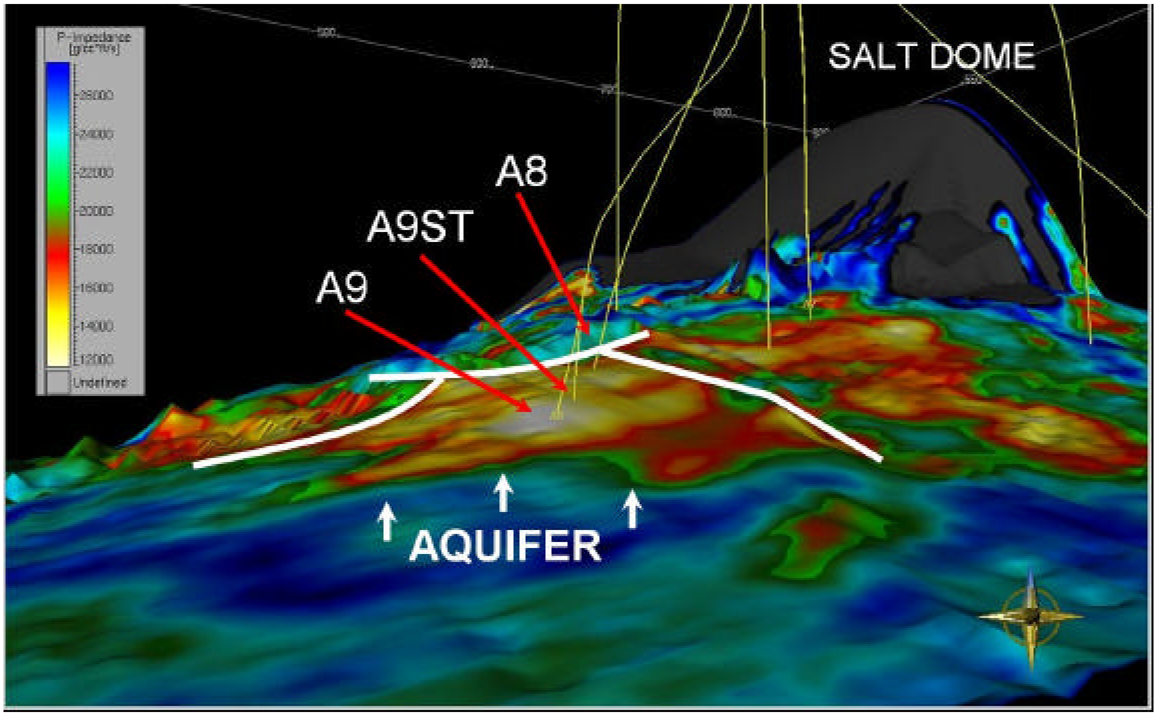

Figure 3.3: Three-dimensional view of the seismic-inverted acoustic impedance cube. The figure shows existing well trajectories in yellow and a color-coded acoustic impedance time horizon. Inverted acoustic impedances across the GNP2RB reservoir were used to construct the color-coded time horizon; low values of acoustic impedance are shown in yellow and high values in blue. The GNP2RB reservoir is a closure of bounding faults and is bounded down-dip by an active aquifer that is responsible for pore-pressure support in the GNP2RB reservoir.

STATIC MODEL

Chapter 4: Geostatistics for Seismic Data Integration

This chapter describes a methodology to quantitatively link seismic-inverted acoustic impedances to well log measurements. Such a methodology is used for the estimation of inter-well spatial distributions of porosity, and permeability. Moreover, a geostatistical inversion technique is compared to standard gestatistical techniques conventionally used to populate inter-well petrophysical properties. The latter include ordinary kriging and co-kriging methods based on sequential Gaussian simulation.

4.1 Acoustic Impedance and its Relationship to Petrophysical Parameters

In order to perform simulations of fluid production with time, it is necessary to construct cellular models where values of porosity and permeability are assigned to every simulation cell. We now proceed to explore whether these two inter-well petrophysical properties can be estimated from seismic-inverted acoustic impedances.

Figures 4.1 and 4.2 are cross-plots constructed to assess whether a statistical correlation exists between acoustic impedance and porosity and permeability. Good quality sands exhibit low values of acoustic impedance (i.e. 14,000 – 20,000 g/cc*ft/s) while poor quality sands and shales exhibit high values of acoustic impedance. The correlation coefficient is approximately –0.95 and –0.91 for acoustic impedance vs. porosity, and acoustic impedance vs. logarithm of permeability, respectively. Such relatively strong correlations confirm that seismic-inverted acoustic impedance may be used to interpolate porosity and permeability in the inter-well region.

Figure 4.3 is a cross-plot of the impedance logs (calculated from the sonic and bulk density logs) and the shale volume derived from the gamma ray logs (refer to equation 2.2), across the GNP2RB reservoir. Separate clouds of points in this cross-plot represent the two main lithological facies (sands and shales), where low values of acoustic impedance correspond to sands and high values of acoustic impedance correspond to shales. The cross-plot confirms that acoustic impedance can be used to discriminate between sands and shales.

Figure 4.4 is a cross-plot of acoustic impedance and calculated water saturation. Again, the GNP2RB reservoir sands are associated with low values of acoustic impedance. The cross-plot indicates that acoustic impedance alone cannot discriminate between the different saturating fluids involved (volatile oil, condensate gas, and water). No correlation exists between water saturation and acoustic impedance. Only at the lowest range of the water saturation scale does acoustic impedance exhibit a small decrease below the otherwise flat trend.

The above observation confirms that acoustic impedance strongly correlates with porosity and poorly correlates with water saturation (refer to Appendix C for a more detailed analysis of this technical issue). Finally, the same cross-plots indicate that shale concentration in the GNP2RB reservoir sands does not correlate with acoustic impedance. From the previous analysis, we can conclude that spatial variations of acoustic impedance within the GNP2RB reservoir primarily correlate with spatial variations of porosity and permeability.

4.2 Geostatistical Estimation Techniques

Geostatistical estimation techniques make use of histograms and spatial variograms (or auto-correlations functions) to describe the spatial continuity and smoothness of reservoir parameters away from existing measurement locations. Figure 4.5 describes the spatial continuity model (semi-variogram) used in this dissertation to interpolate acoustic impedance.

Because seismic data involve spatially dense measurements across the reservoir, we estimated the range of the lateral semi-variograms (separately for the in-line and cross-line directions) from seismic-inverted acoustic impedances. This estimation was performed following the embedding geometry and proportional sedimentary layering imposed by the two seismic horizons that mark the upper and lower boundaries of the GNP2RB reservoir. On the other hand, due to the high vertical resolution of well logs, we estimated the vertical range of the semi-variogram from acoustic impedance well logs. Figure 4.5 also shows the normalized histogram constructed with the complete set of available measurements of acoustic impedance. This normalized histogram exhibits a bimodal distribution corresponding to the two main lithology types (sands and shales).

To understand the contribution of post-stack seismic amplitude data in the construction of static reservoir models, and to analyze potential difficulties and limitations of different geostatistical methods used to construct reservoir models, in this dissertation we consider the following classes of constructed reservoir models:

1. A homogeneous reservoir model,
2. 3D reservoir models constructed with the use of two standard geostatistical techniques, namely,
   (a) Sequential Gaussian simulation of well-logs, and
   (b) Collocated sequential Gaussian co-simulation of well-logs and seismic-inverted acoustic impedances.
3. 3D reservoir models constructed with a geostatistical inversion technique that simultaneously honors 3D seismic amplitude data and well logs.

The construction of a homogeneous and isotropic reservoir model requires of one single couplet of porosity and permeability. Accordingly, we constructed this homogeneous fluid-flow simulation model using average porosity and permeability values of 27% and 354 mD, respectively (refer to Figure 4.6). Such a reservoir model provides a quantitative reference to compare the influence of the spatial variability of porosity and permeability against the influence of fluid and rock-fluid properties in the dynamic behavior of the reservoir after the onset of production.

4.2.1 Conventional geostatistical interpolation of well logs and core data using Sequential Gaussian Simulation

Deutsch and Journel (1998) state that Sequential Gaussian Simulation (SGS) is probably the most flexible technique used to model reservoir heterogeneity and to quantify uncertainty. We implemented this procedure to construct stochastic realizations of reservoir porosity and permeability constrained by lithology. Figure 4.6 shows that the distributions of porosity and logarithm of permeability sampled from well logs exhibit a bimodal statistical behavior due to the existence of two main lithologies: sands and shales. To honor these distributions, we populated inter-well porosity and logarithm of permeability in the GNP2RB reservoir following two sequential steps: (a) geostatistical simulation of the facies (two possible outcomes: sands and shales) and (b) Gaussian simulation of porosity and logarithm of permeability within each of the simulated facies.

The geostatistical simulation of the two facies is based on synthetic litho-type logs. The latter are constructed from the shale-volume log by imposing a cut-off that discriminates between sand and shales (i.e. 0.45). Figure 4.7 shows normalized histograms sampled from the constructed litho-type logs for wells A9ST, A8, A10ST, and A11 (upper panel) and for the simulated litho-type volumes geostatistically inverted for the two facies (lower panel). These normalized histograms are used to estimate the probability of occurrence, p, for the two facies, namely 58% for sands and 42% for shales. We make use of sequential indicator simulation (Lortzer and Berkhout, 1992) to assign a litho-type to each cell in the geostatistical grid. This process requires of spatial semi-variograms for each litho-type. The upper panel of Figure 4.8 shows the sampled semi-variogram for sands, where the corresponding sill (0.25) was estimated from the relationship (Lortzer and Berkhout, 1992),

$$sill = p(1-p)\,. \tag{4.1}$$

4.2.2 Collocated co-simulation of seismic-inverted acoustic impedance and well logs

For the case of Gaussian collocated co-simulation (CSGS), seismic-inverted acoustic impedances constitute a secondary input that remains statistically correlated with both porosity and logarithm of permeability (Figures 4.1 and 4.2). Accordingly, the Gaussian simulations of porosity and permeability are constrained by their local correlation with acoustic impedance.

4.2.3 Joint stochastic inversion of well logs, acoustic impedance and 3D post-stack seismic data (post-stack geostatistical inversion)

Geostatistical inversion (GI) is a stochastic inversion procedure that honors the available 3D seismic amplitude data, the well logs, the assumed semi-variograms, and a global normalized histogram (or probability density function). Seismic amplitude data are honored in an iterative manner. First, porosity and logarithm of permeability are populated in the reservoir using SGS. The populated values of porosity and logarithm of permeability are transformed to acoustic impedance using pre-defined statistical correlations. This transformation is then used to simulate the seismic post-stack seismic data trace-by-trace via the one-dimensional convolutional model given by equation (3.1). Subsequently, a metric of the global seismic misfit error is calculated with the sum of squared differences between the simulated seismic traces and the measured seismic traces over the complete post-stack seismic cube.

The latter metric defines the global seismic misfit. Minimization of the global seismic misfit is achieved in a monotonic fashion through a sequence of iterations. Each iteration consists of a random walk through the entire seismic cube. The random walk is performed in both seismic time and lateral location. Simulations of both porosity and permeability are performed for the particular location designated by the random walk followed by the corresponding transformation to acoustic impedance and calculation of the global seismic misfit. Simulated annealing is used to decide whether to accept or reject the simulated acoustic impedance at a particular location in the seismic cube in view of: (a) the change in global seismic misfit due to that simulation and (b) the prescribed criterion for global misfit reduction from iteration to iteration. An iteration is deemed complete when simulations of porosity and logarithm of permeability have been accepted or rejected at all the nodes in the seismic cube (Grijalba-Cuenca et al., 2000). The inversion comes to an end when the global seismic misfit has decreased to a prescribed lower bound or else when the number of iterations has reached a prescribed maximum. Independent inversions of porosity and permeability can be obtained by starting the process over with independent initial realizations of porosity and permeability via SGS (iteration no. zero). An important feature of geostatistical inversion is that the vertical resolution of the inverted distributions can be adjusted anywhere between the vertical resolution of well logs and seismic data.

4.3 Summary

We performed thirty independent geostatistical inversions of acoustic impedance, porosity, and logarithm of permeability within the GNP2RB reservoir enforcing the same vertical resolution as the seismic data (4 ms). Figure 4.9 shows plan views of the correlation between the measured and the numerically simulated post-stack seismic data as a function of the number of iterations (minimum correlation is zero and maximum correlation is one). The first map (iteration zero) corresponds to the seismic correlation associated with SGS (here used to initialize the inversion). Subsequent iterations entail a monotonic increase in the seismic correlation. For the last iteration (iteration no. 35), the correlation has reached the final value of 0.95.

Unless otherwise noticed, all the reservoir models constructed with the SGS, CSGS, or GI techniques described in this dissertation made use of the same semivariogram models (shown in Figure 4.8) to populate reservoir porosity and logarithm of permeability between wells. Moreover, the simulations of porosity and logarithm of permeability were preceded by the simulation of lithology (two possible outcomes: sands or shales).

Spatial distributions of porosity and permeability rendered by SGS, CSGS, and GI were transformed from seismic time to depth using the available distribution of interval P-wave velocities. We generated a P-wave velocity cube from the interpolation of P-wave velocity logs, previously transformed from measured depth to true vertical depth (TVD). In addition, the conversion from seismic time to depth was guided by the two seismic horizons marking the lower and upper boundaries of the GNP2RB reservoir. The transformation enforced a uniform sampling interval in depth via the relationship

$$\bar{V} = \frac{\Delta h}{\Delta t}, \tag{4.2}$$

where $\bar{V}$ is the average P-wave velocity of 8404 ft/s (2562 m/s) obtained from well-log measurements across the GNP2RB reservoir, Δt is the time sampling interval (4 ms), and Δh is the calculated depth sampling interval, in this case equal to 34 ft (10 m). Figure 4.10 graphically compares cross-sections of porosity in the seismic-time and depth domains. As observed from that figure, all the features of the spatial distributions of porosity have been preserved by the seismic time-to-depth transformation (refer to Chapter 6 for details about the used grid dimensions). Figure 4.11 is a composite display of seismic-time cross-sections of seismic amplitudes, geostatistically-inverted acoustic impedance, lithology, porosity, and logarithm of permeability, shown here merely for comparison purposes.

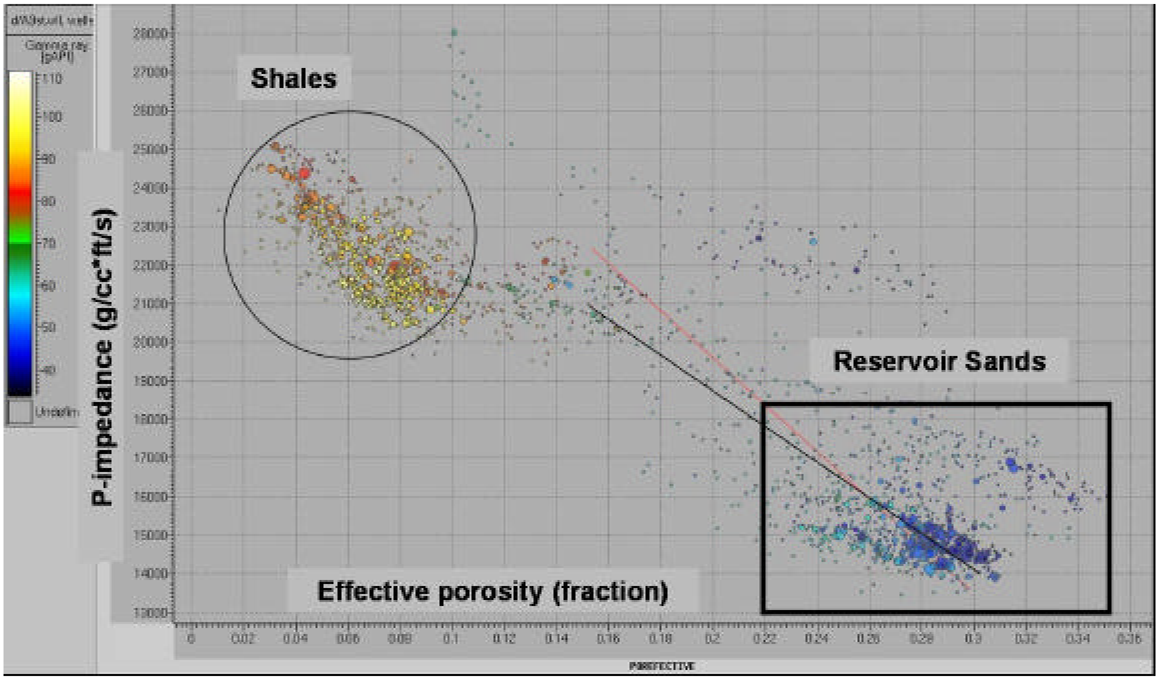

Figure 4.1: Cross-plot of acoustic impedance and effective porosity constructed with well-log data from wells A10st and A8. Points in the cross-plots are color-coded using the corresponding value of gamma-ray log. High values of gamma-ray log are shown in yellow and low values in dark blue. The black line in the figure was constructed from linear regression analysis using only well-log data acquired across sands (the correlation coefficient (R^2) is –0.95). The red line, on the other hand, describes a linear trend used to assess the sensitivity of the estimated effective porosity to a perturbation in the acoustic impedance-effective porosity linear correlation (the correlation coefficient for this line is -0.92).

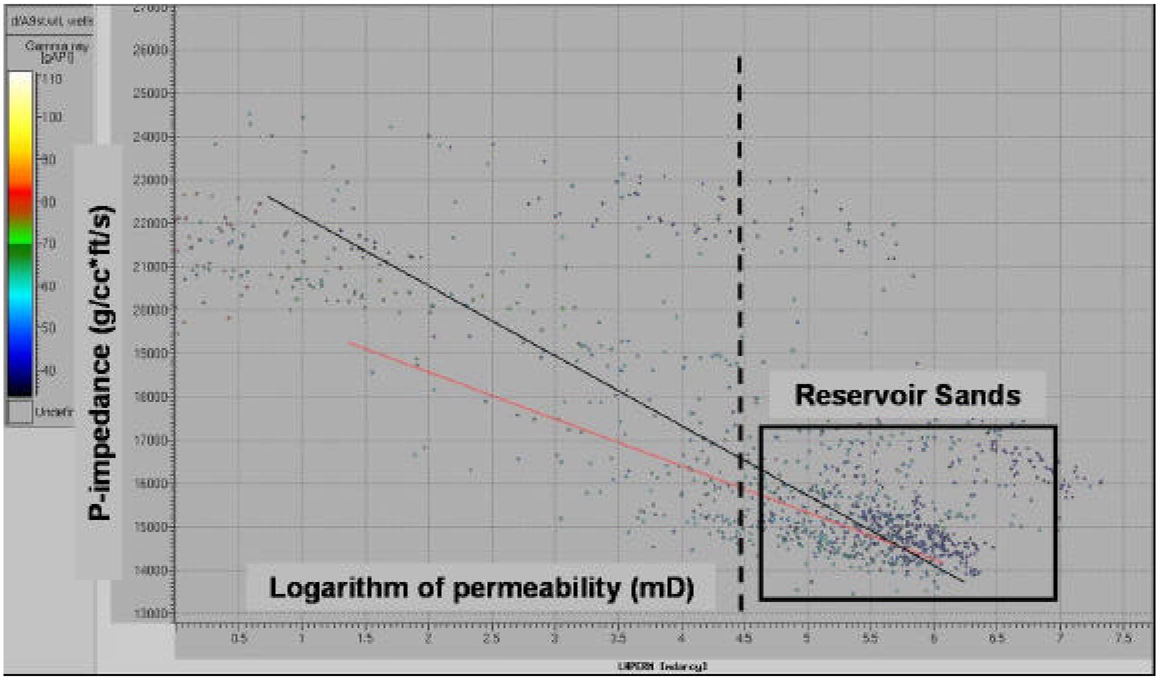

Figure 4.2: Cross-plot of acoustic impedance and logarithm of permeability constructed with well-log data from wells A10st and A8. Points in the cross-plots are color-coded using the corresponding value of gamma-ray log. High values of gamma-ray log are shown in yellow and low values in dark blue The black line in the figure was constructed from linear regression analysis using only well-log data acquired across sands (the correlation coefficient, R^2, is –0.92). The red line, on the other hand, describes a linear trend used to assess the sensitivity of the estimated logarithm of permeability to a perturbation in the acoustic impedance-logarithm of permeability linear correlation (the correlation coefficient of this line is -0.83).

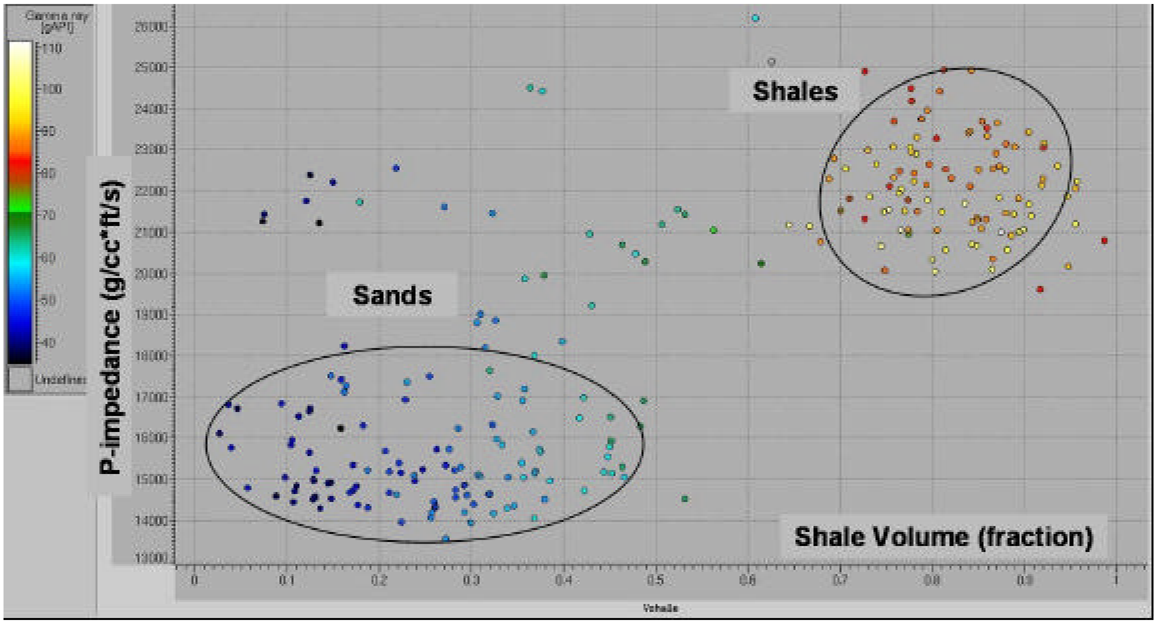

Figure 4.3: Cross-plot of shale volume and acoustic impedance. Acoustic impedance was calculated as the product of P-wave velocity and bulk density logs acquired in wells A10st and A8. The shale-volume log was calculated from the gamma ray logs acquired in the same wells across the GNP2RB reservoir. This cross-plot emphasizes that acoustic impedance permits discrimination of the two main lithological facies (sands and shales). The lowest values of acoustic impedance are associated with sands and the highest values are associated with shales.

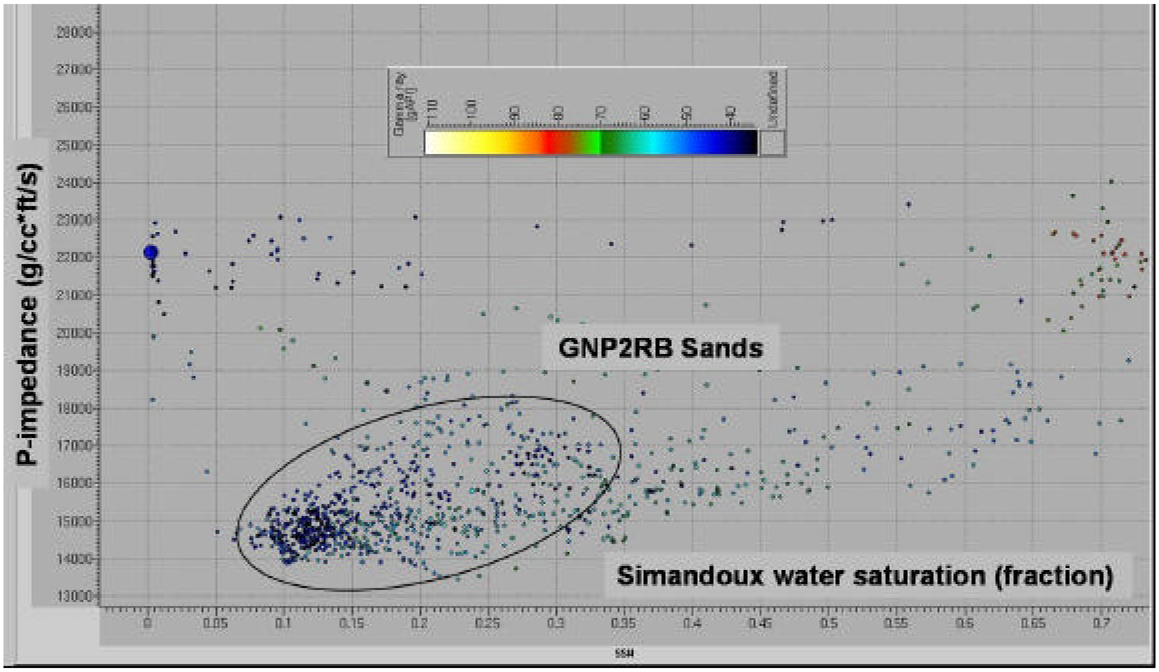

Figure 4.4: Cross-plot of acoustic impedance and Simandoux water saturation constructed with well-log data acquired in wells A10st and A8 within sand units only. Well-log data measured across the GNP2RB reservoir are enclosed by the black ellipse. This cross-plot indicates that acoustic impedance alone cannot be used to uniquely identify saturating fluids. However, the cross-plot indicates that the lowest acoustic impedance values are associated with gas-saturated sands.

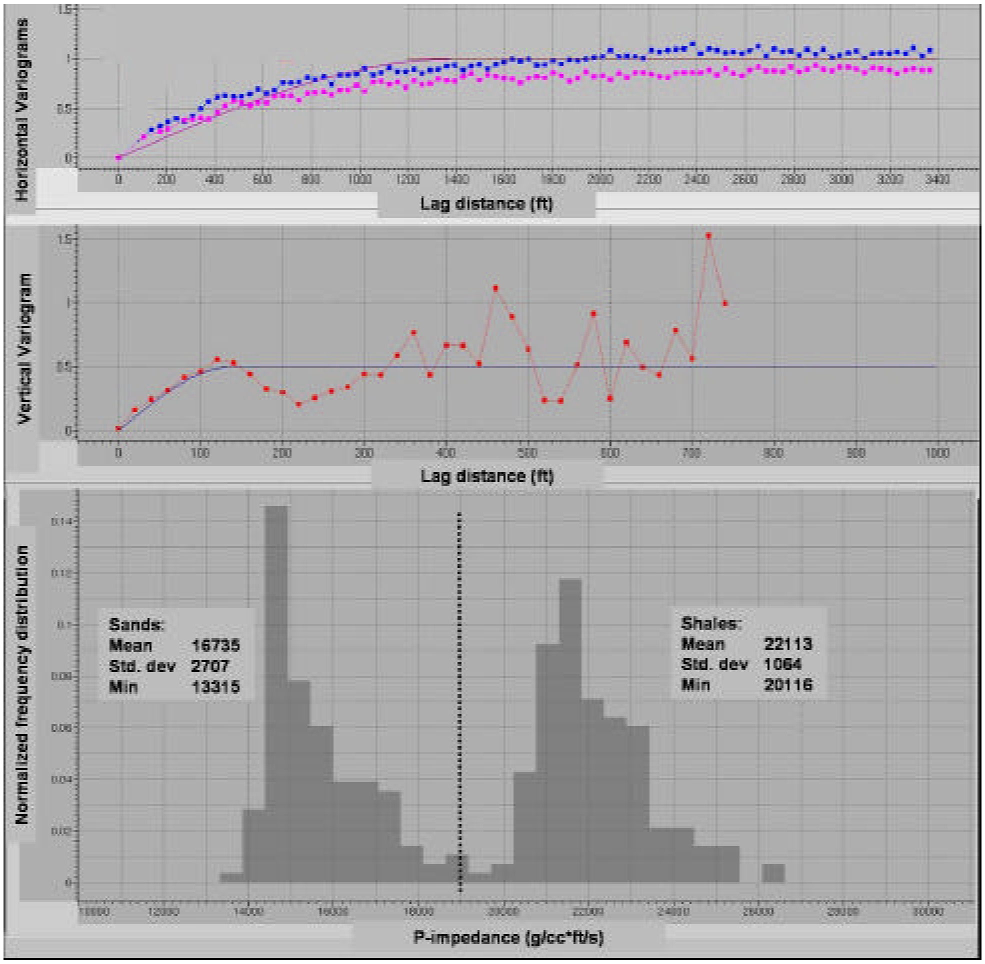

Figure 4.5: Spatial continuity model (semi-variogram) used to populate acoustic impedance in the inter-well region of the GNP2RB reservoir. The top panel describes the sampled (discrete points) and modeled (continuous lines) horizontal semi-variograms in the in-line and cross-line seismic directions. The model semi-variograms were derived from a spherical model of range and sill equal to 1400 ft and 1, respectively. Sampled semi-variograms were constructed using seismic-inverted acoustic impedances. The panel in the middle describes the sampled (discrete points) and modeled (continuous line) vertical semi-variograms. Well-log acoustic impedances were used to construct the sampled vertical semi-variogram, whereas the modeled vertical semi-variogram was constructed using a spherical model of range and sill equal to 140 ft and 0.5, respectively. The lower panel is a normalized histogram constructed with well-log acoustic impedances. A bimodal behavior in the histogram emphasizes the two main lithology types (sands and shales) across the GNP2RB reservoir.

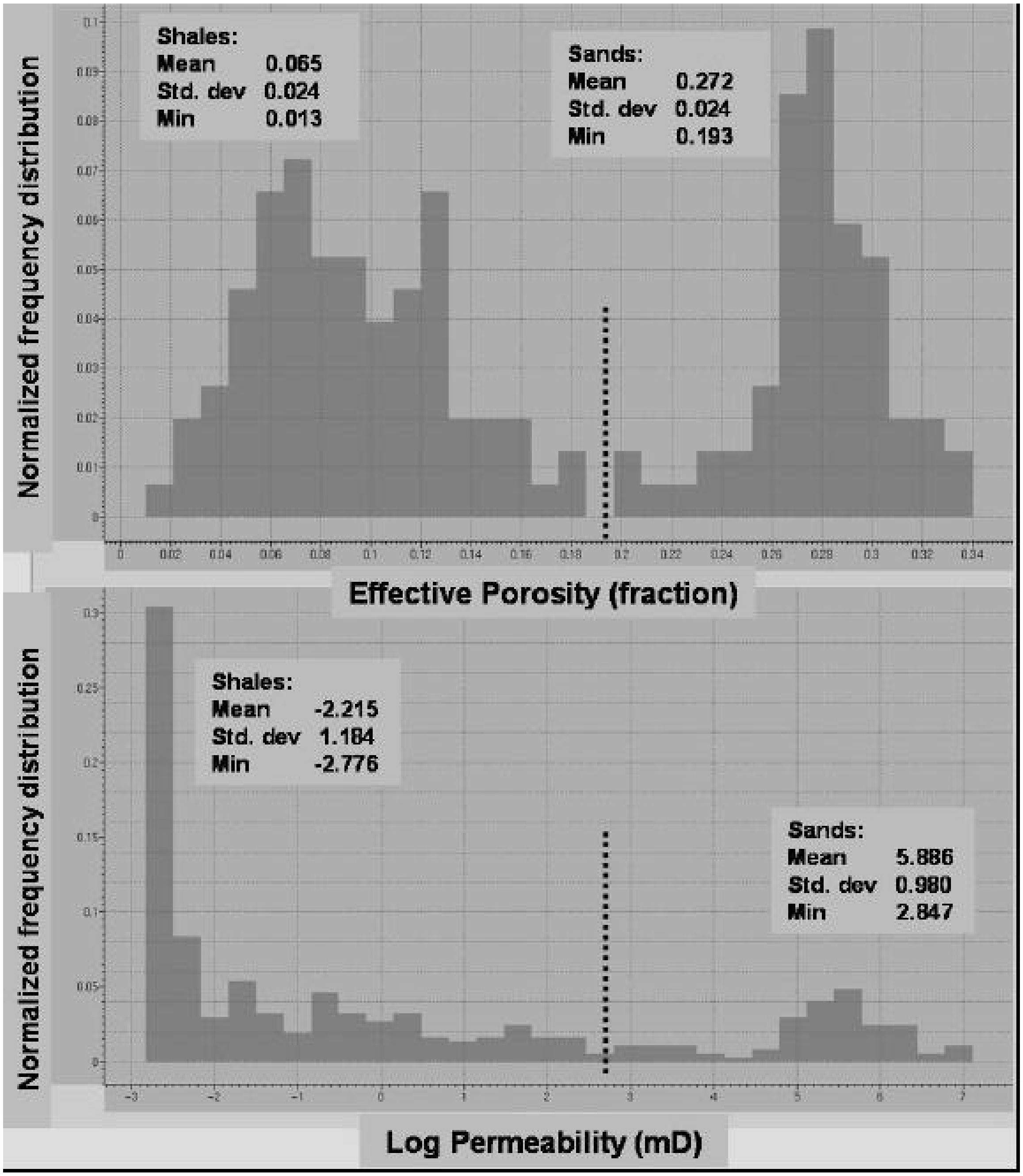

Figure 4.6: Normalized histograms of effective porosity (upper panel) and logarithm of permeability (lower panel) constructed with well-log data acquired in wells A10st and A8 across the GNP2RB reservoir. The bimodal behavior of both normalized histograms indicates that lithology discrimination (sands or shales) can be performed with a simple cut-off on both effective porosity and logarithm of permeability.

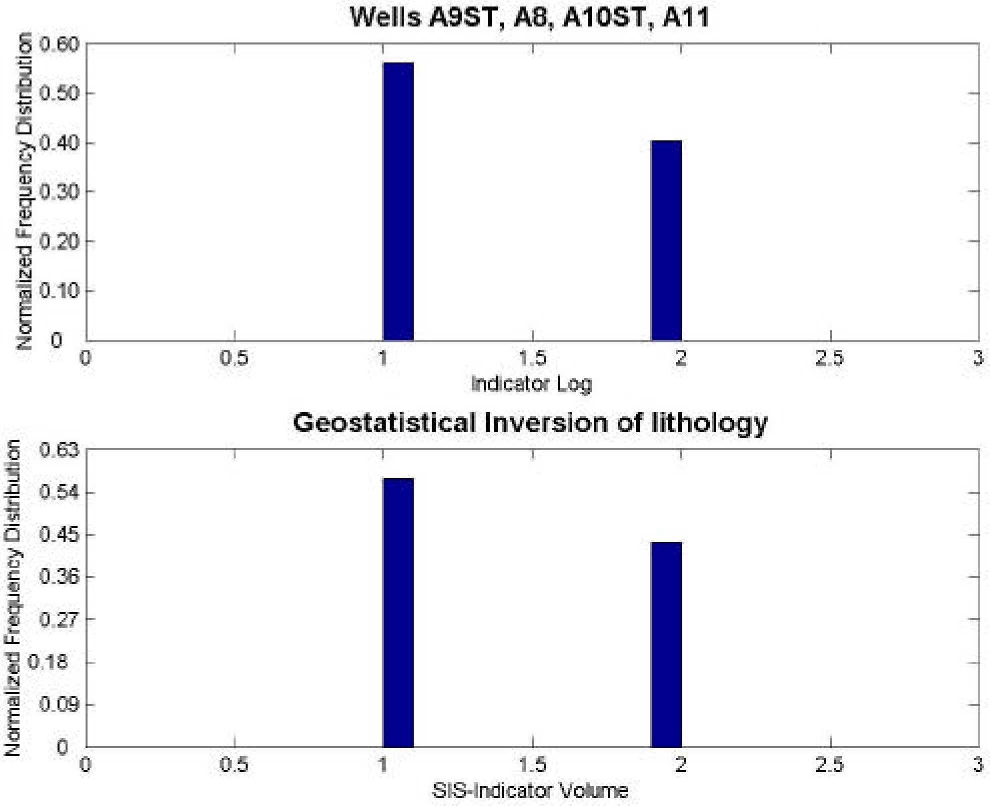

Figure 4.7: Histogram of facies (sands and shales) sampled from litho-type logs synthesized in wells A9ST, A8, A10st and A11 across the GNP2RB reservoir (upper panel) and from geostatistically inverted litho-type volumes. The synthesis of litho-type logs was performed by enforcing a cut-off value on the synthetic volume-of-shale log (i.e. Vsh = 0.45). Two possible outcomes are present: sands (1) or shales (2).

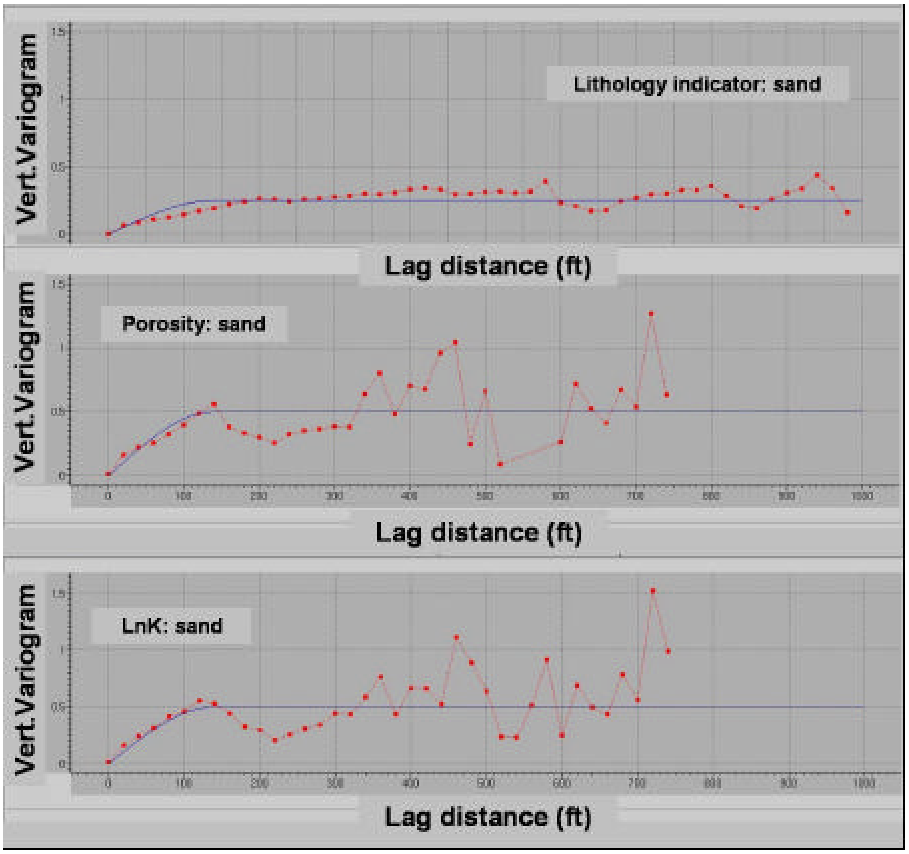

Figure 4.8: Spatial continuity model (semi-variogram) used to populate lithology, porosity, and logarithm of permeability in the inter-well region of the GNP2RB reservoir. The upper panel describes the sampled (discrete points) and modeled (continuous line) vertical semi-variograms used to describe the spatial variability of sand units. The modeled vertical semi-variogram was constructed using a spherical model of range and sill equal to 140 ft and 0.25, respectively. The middle panel describes the sampled (discrete points) and modeled (continuous line) vertical semi-variogram for porosity within sand units. In this panel, the modeled vertical semi-variogram was constructed using a spherical model of range and sill equal to 140 ft and 0.5, respectively. The lower panel describes the sampled (discrete points) and modeled (continuous lines) vertical semi-variogram for the logarithm of permeability within sand units. In this last panel, the model semi-variogram was constructed using a spherical model of range and sill equal to 140 ft and 0.5, respectively. For all the cases, vertical semi-variograms were sampled from well logs and lateral semi-variograms from the cube of seismic-inverted acoustic impedances. Lateral semi-variograms were modeled using a spherical semi-variograms of range and sill equal to 1400 ft and 0.5, respectively.

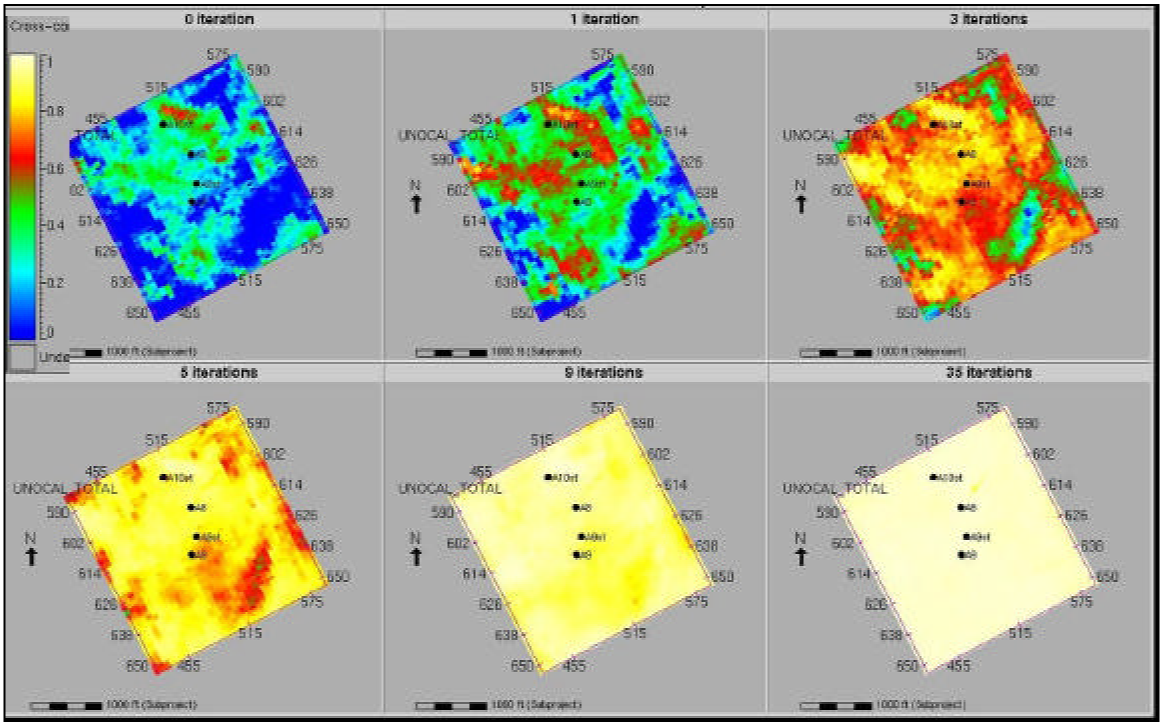

Figure 4.9: Maps of the correlation between measured and simulated post-stack seismic data as a function of the number of iterations in the geostatistical inversion of inter-well acoustic impedance. The maps show well locations in black and seismic correlation in color-coded values. Low values of seismic correlation are shown in dark blue and high values in yellow. Geostatistical inversion is initialized (iteration no. 0, upper left-hand panel) with a realization rendered by sequential Gaussian simulation (SGS). As the number of iterations increases the seismic correlation increases between existing well locations. At the last iteration (iteration no. 35, lower right-hand panel), the seismic correlation achieved by geostatistical inversion is nearly perfect across the GNP2RB reservoir.

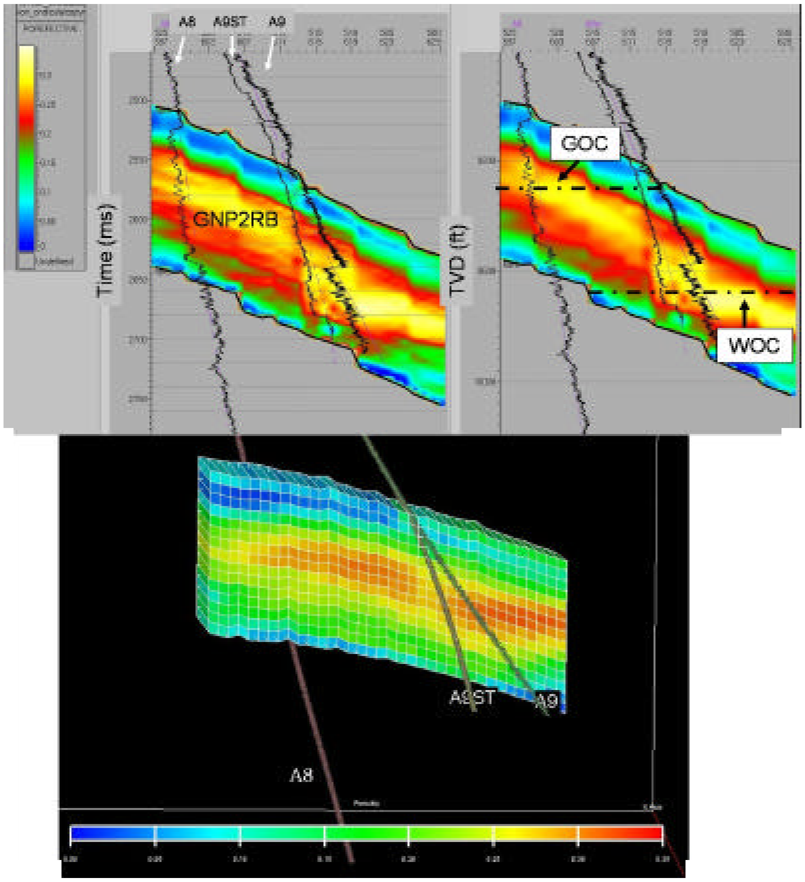

Figure 4.10: Cross-section of the mean of thirty geostatistically inverted porosity models showing the trajectories (shown in purple) and gamma ray logs (shown in in black) of three of the wells (A8, A9, and A9ST) across the GNP2RB reservoir. The upper left-hand and right-hand panels show the mean value of porosity in the seismic-time and depth domains, respectively. Black dashed lines indicate the location of water-oil and gas-oil contacts. The lower panel shows the corresponding cross-section of the cellular reservoir simulation model (y and z directions) consisting of 15x36x15 reservoir cells in the x, y, and z directions, respectively. Porosity values for each cell in this panel are color coded, with the lowest and largest porosity indicated in dark blue and yellow, respectively. Notice that the upper and lower boundaries of the cellular reservoir model conform to the geometrical embedding imposed by the seismic horizons that mark the upper and lower boundaries of the GNP2RB reservoir. Well A9 was drilled down-dip of well A8 to locate the water-oil contact (WOC, located 9763’ TVD), whereas well A9 was junked and re-drilled up-dip (well A9st) away from the WOC and completed in the same sand penetrated by well A8.

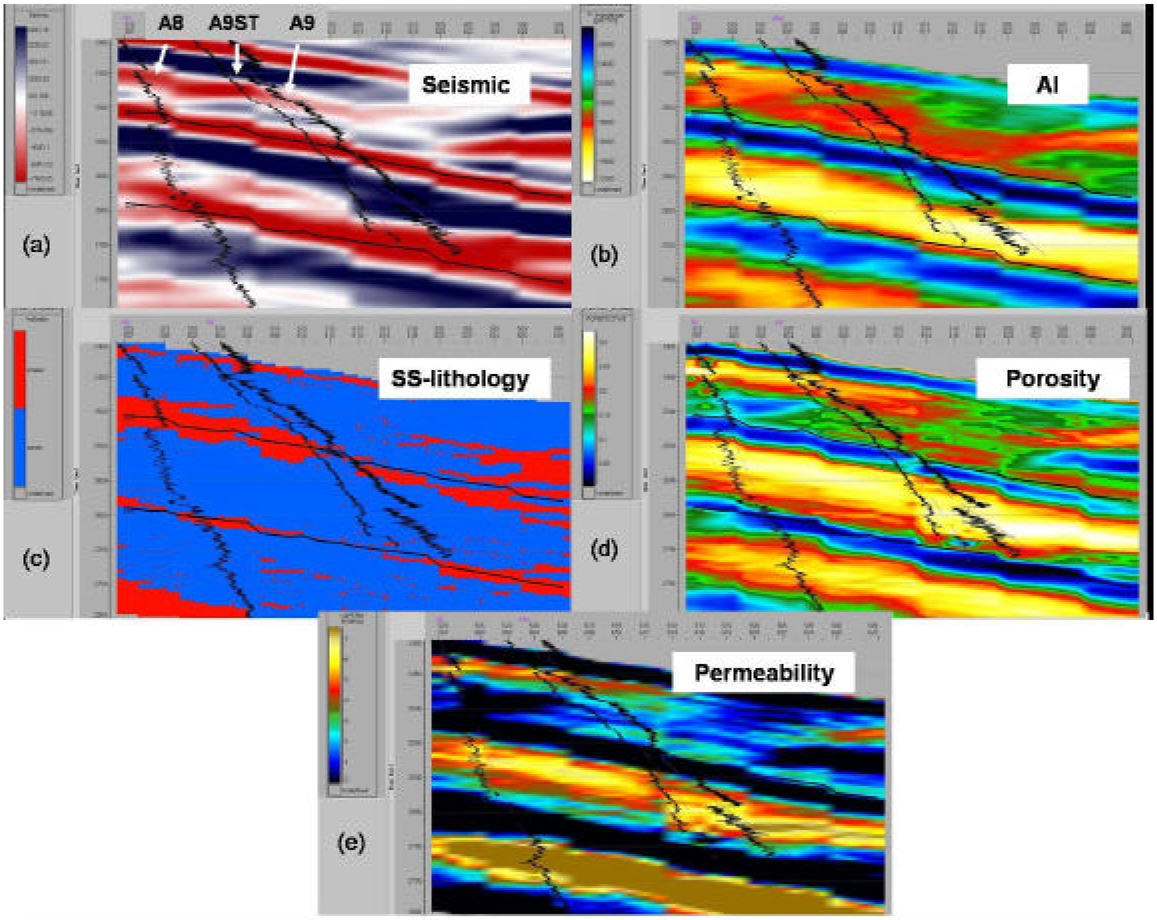

Figure 4.11: Cross-sections of (a) post-stack seismic data (upper left-hand panel), (b) geostatistically inverted acoustic impedance (upper right-hand panel), (c) inverted sand-shale lithology (middle left-hand panel), (d) porosity (middle right-hand panel), and (e) logarithm of permeability (lower panel). The cross-sections indicate the trajectories of three wells (A8, A9, and A9ST) penetrating the GNP2RB reservoir. Thin black lines describe the seismic horizons that define the upper and lower boundaries of the GNP2RB reservoir.

DYNAMIC RESERVOIR MODEL

Chapter 5: Reservoir and Fluid Description

There is more than one single production mechanism during the pressure-depletion life of the reservoir under study. The major production mechanism is water-drive by an external aquifer, although solution gas or dissolved gas drive and gas cap expansion are also responsible for primary fluid production. To diagnose the existence of a water-drive, the observation of monotonically increasing water production was not the only clue; we employed material balance equations to determine water influx (refer to Appendix B). Figure 5.1 describes the results of the material balance calculations indicating the predominant production drive mechanisms and the calculated water influx.

Figure 5.2 shows the time records of the gas-oil ratio produced from the two wells completed in the zone under consideration. From production measurements, it is found that the gas cap contains condensates of about 50° API gravity; therefore, the volatilized oil-gas ratio is in the range of 0 - 52 stb/MMscf. Figure 5.3 shows the cumulative oil, gas, and water production for each well plus the time record of static reservoir pressure for the entire reservoir.

Walsh and Lake (2003) define black oils as those having initial gas-oil ratios of 1200 scf/stb or less, while volatile oils range between 1,200 and 3,500 scf/stb, and gas condensates between 8000 and 30000 scf/stb. Fluid production from the GNP2RB reservoir (shown in Figure 5.2) indicates that the produced fluids are manly volatile and condensate gas.

From available geological information and fluid saturation inferred from well logs, it is found that the location of well A8 is up dip in the structure and close to the primary gas cap, while well A9ST is located down dip in the structure and close to the water-oil contact. Both wells were completed in the reservoir’s oil leg where the gravity of the stock-tank oil is 40° API. However, the gas cap significantly affects the fluid production from well A8, whereas the fluid production from well A9ST is drastically influenced by aquifer recharge (refer to Figure 5.3).

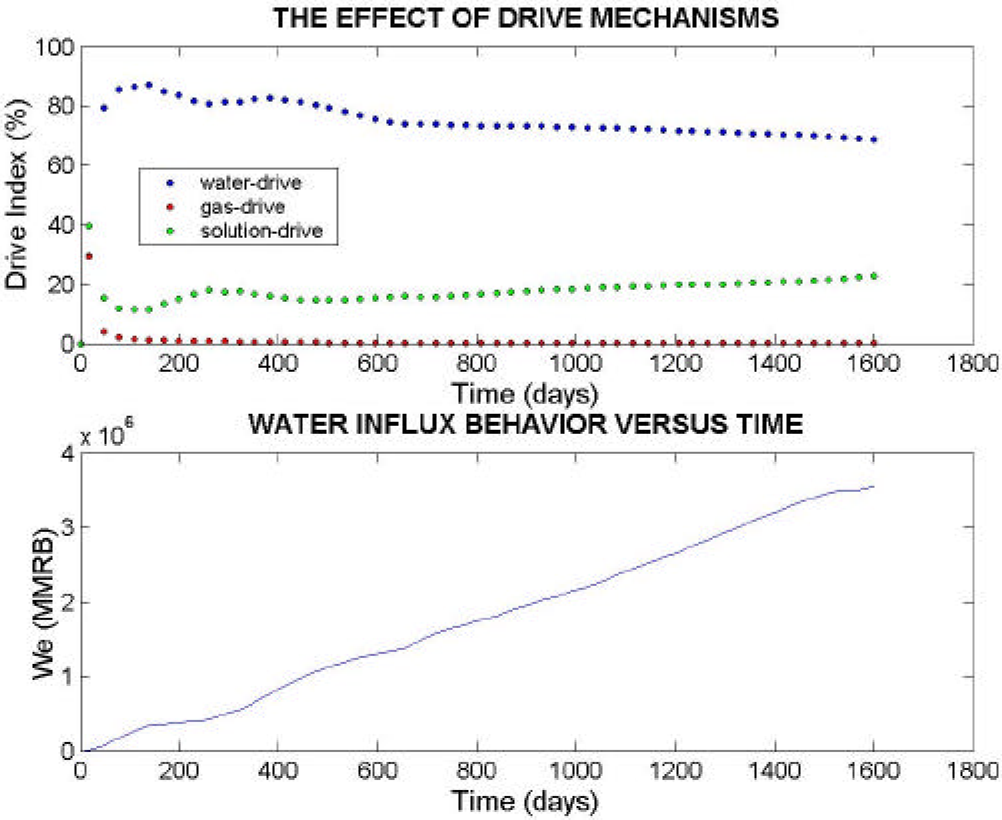

Figure 5.1: Material balance calculations. The top panel describes the estimated three drive indexes governing fluid production in the GNP2RB reservoir. The bottom panel describes the calculated cumulative water influx versus time after the onset of production. The slope of the latter plot represents the constant water influx flow-rate due to external aquifer pressure support and was used to perform the simulations of fluid-flow behavior. Refer to equation (B.20) for the formulation to estimate the water influx flow-rate.

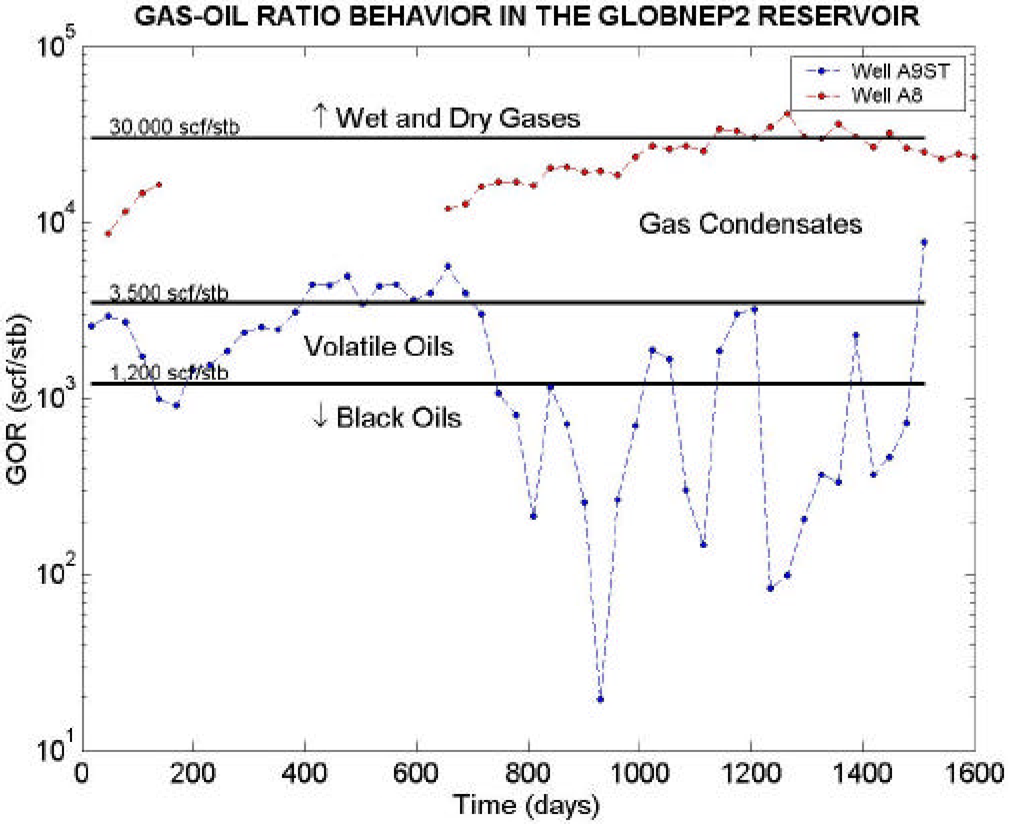

Figure 5.2: Time evolution of the measured gas-oil ratio after the onset of production for the only two producing wells in the GNP2RB reservoir.

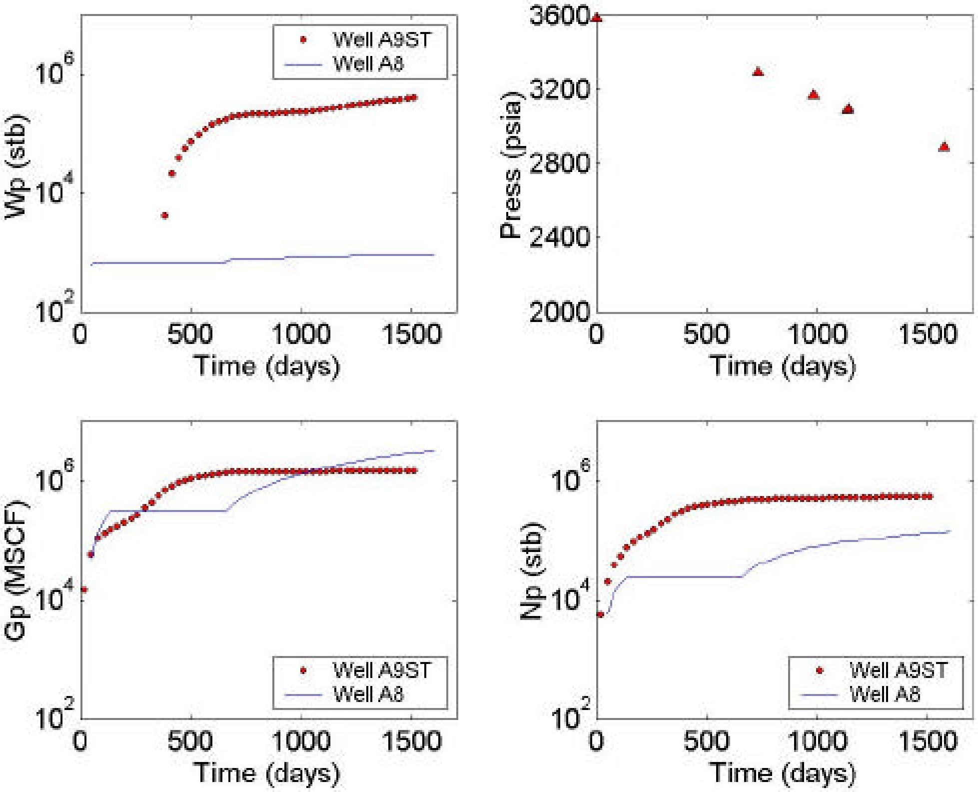

Figure 5.3: Plots of the time evolution of cumulative fluid production and reservoir pressure in the GNP2RB reservoir after the onset of production. Plots are shown of the cumulative water production (upper left-hand panel), cumulative gas production (lower left-hand panel), and cumulative oil production (lower right-hand panel) for the wells A9ST and A8. The upper right-hand panels show the time evolution of reservoir pressure.

Chapter 6: Numerical Simulation of Reservoir Behavior After The Onset of Production

We simulate the dynamic behavior of reservoir GNP2RB as a modified black-oil tank model with active aquifer recharge at the bottom and a gas cap at the top. Locations of the water-oil and gas-oil contact were defined from electrical resistivity, neutron porosity, and bulk density logs. Moreover, the reservoir was assumed to be in capillary equilibrium prior to production.

The grid dimensions used to simulate primary fluid flow recovery are the same as those used to simulate the post-stack seismic data. Upscaling was not performed on the property cells. The number of reservoir simulation cells in the x and y directions is the same as the number of seismic in-lines and cross-lines, respectively. In the z-direction, the number of reservoir simulation cells is consistent with the vertical resolution of the seismic data, i.e. 34 ft. Therefore, the numerical grid used to simulate multi-phase fluid-flow consists of 15x36x15 cells in the x, y, and z directions, respectively (8,100 reservoir cells). Table 6.1 summarizes the fluid properties, rock-fluid properties, and spatial discretization parameters associated with the hydrocarbon reservoir model considered in this dissertation.

Prior to simulating the time behavior of the reservoir after the onset of production, we performed a sensitivity analysis to assess the numerical accuracy of the finite-difference, corner-point fluid-flow grid. Simulation exercises were carried out with three finite-different grid sizes. The number of grid cells for each of these exercises was 15x36x15, 15x36x30, and 15x36x45 in the x, y, and z directions, respectively. Figure 6.1 describes time records of fluid production and pressure simulated with the three corner-point fluid-flow grids. In the three cases, the agreement between the simulations and the measurements is excellent. Based on these results, we constructed the final reservoir models with (a) a corner point fluid-flow grid of cell dimensions equal to 81x41x34 ft in the x, y, and z directions, respectively, (b) 15x36x15 grid cells in the x, y, and z directions, respectively, (c) a closed reservoir with active aquifer recharge, and (d) two producing wells. Figure 6.2 is a 3D rendering of the corner-point finite-difference grid used in the numerical simulations of fluid production and pressure depletion in the GNP2RB reservoir.

We calculated thirty independent stochastic realizations of porosity and permeability for each of the three statistical techniques used to populate the inter-well region of the reservoir. The realizations were input separately to the multiphase black-oil simulator ECLIPSE$^{\mathbf{TM}}$. Brooks-Corey type relative permeability and capillary pressure curves were used in the multi-phase fluid flow simulation (refer to Appendix A). These curves, shown in Figure 6.3, were assumed constant throughout the GNP2RB reservoir.

In this field study, 1599 days (approximately 4 years) of production history are available. Oil flow rates in each well were specified in the simulations, with water, gas production rates, and pressure depletion used to assess the agreement between the simulated and the measured time record of fluid production measurements. Because the principal drive mechanism is water-drive, plots of cumulative water production in the reservoir are used to analyze the impact of the constructed spatial distributions of porosity and permeability on the simulated time records of fluid production (refer to Appendix D for a description of the PVT correlations assumed in the fluid-flow simulations).

Figure 6.4 compares the cumulative water production versus time for the three different statistical techniques (SGS, CSGS, and GI) used to populate porosity and permeability in the GNP2RB reservoir. Results obtained from thirty independent models for each case are compared against the measured time records of water production (the latter identified with yellow dots in Figure 6.4). Sequential Gaussian simulation consistently yields the highest cumulative water production as well as the largest spread among the simulations. For the collocated Gaussian co-simulation case, both the spread and the magnitude of the simulation decrease compared to those of SGS. Therefore, we conclude that the reliability of the constructed models improves with the use of seismic amplitude data. Geostatistical inversion yields the least biased and most accurate simulation results. Models generated with the use of seismic amplitude data produced the best agreement with the time records of fluid production measurements and exhibited the smallest spread among all the simulation results. Moreover, we found a good agreement between simulated and measured time records of both cumulative gas production and reservoir pressure.

The upper panel in Figure 6.5 shows a seismic-time cross-section of a porosity realization obtained separately with the three geostatistical simulation procedures considered in this dissertation (SGS, CSGS, and GI). Different connectivity patterns of reservoir porosity are associated with each case, thereby explaining why the corresponding simulations of time records of fluid production measurements are so drastically different among themselves. The same remark applies to the case of permeability described in the lower panel of the same figure.

Table 6.1: Summary of the fluid properties, rock-fluid properties, and spatial discretization associated with the hydrocarbon reservoir model considered in this dissertation.

Properties		Values and units
Fluids	Water density	1.1 g/cm^3 at standard conditions
	Oil density	0.8251 g/cm^3 at standard conditions
	Specific gas gravity	0.65 at standard conditions
	Water viscosity	0.34 cp
	Oil viscosity	0.274 cp at 200 psia
	Gas Viscosity	0.013 cp at 14.7 psia
	Water compressibility	6.71E-6 psi^{-1} at Pb
	Oil compressibility	4.42E-05 psi^{-1} at Pb
	Gas compressibility	2.79E-04 psi^{-1} at Pb
Rock-Fluid Properties	Irreducible water saturation	12%
	Residual oil saturation	10%
	Average effective porosity	27%
	Average permeability	354 mD
	Formation compressibility	1.614e-7 psi^{-1}
	Relative permeability water end-point	0.3
	Relative permeability oil end-point	0.8
	Relative permeability gas end-point	0.9
	Vertical to horizontal permeability ratio	1.0
	Location of pressure datum	9656 ft (below the sea bottom)
	Location of gas-oil contact	9406 ft (below the sea bottom)
	Location of water-oil contact	9700 ft (below the sea bottom)
Simulation	Bubble pressure, Pb at t = 0 days	3580 psia
	Number of cells (x,y,z)	15x36x15
	Cell size (dz,dy,dz)	81ft x 41 ft x 34 ft

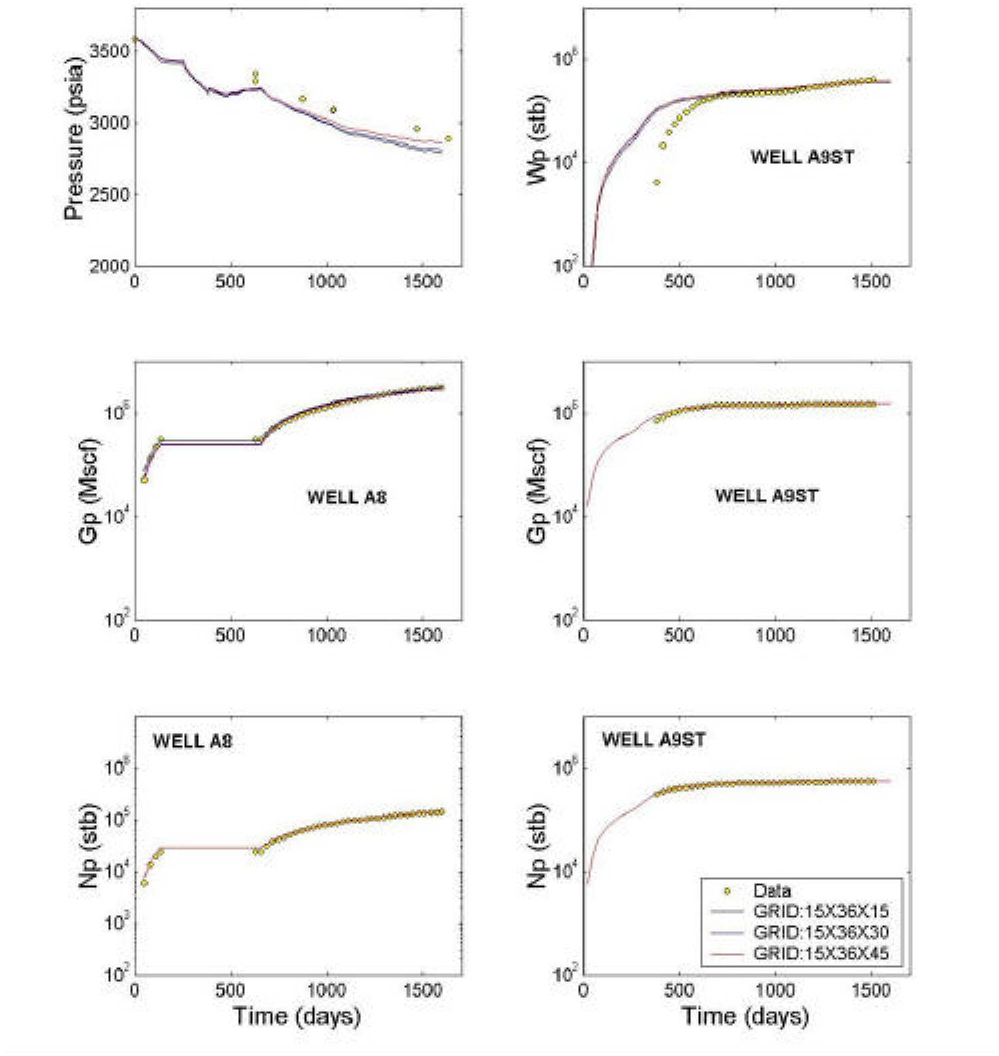

Figure 6.1: Comparison between measured and simulated pressure and fluid production data after the onset of production. The panels show the time evolution of reservoir pressure (upper left-hand panel), cumulative water (Wp), gas (Gp), and oil (Np) production individually for wells A8 and A9ST (well A8 did not manifest water production). The numerically simulated production measurements were obtained using a corner-point finite-difference grid of different cell uniform sizes in the x, y, and z directions. Numerical simulation results are shown for three cell sizes (the corresponding number of grid cells is indicated in the lower right-hand panel). Subsequent simulation studies are performed only with the coarsest finite-difference grid.

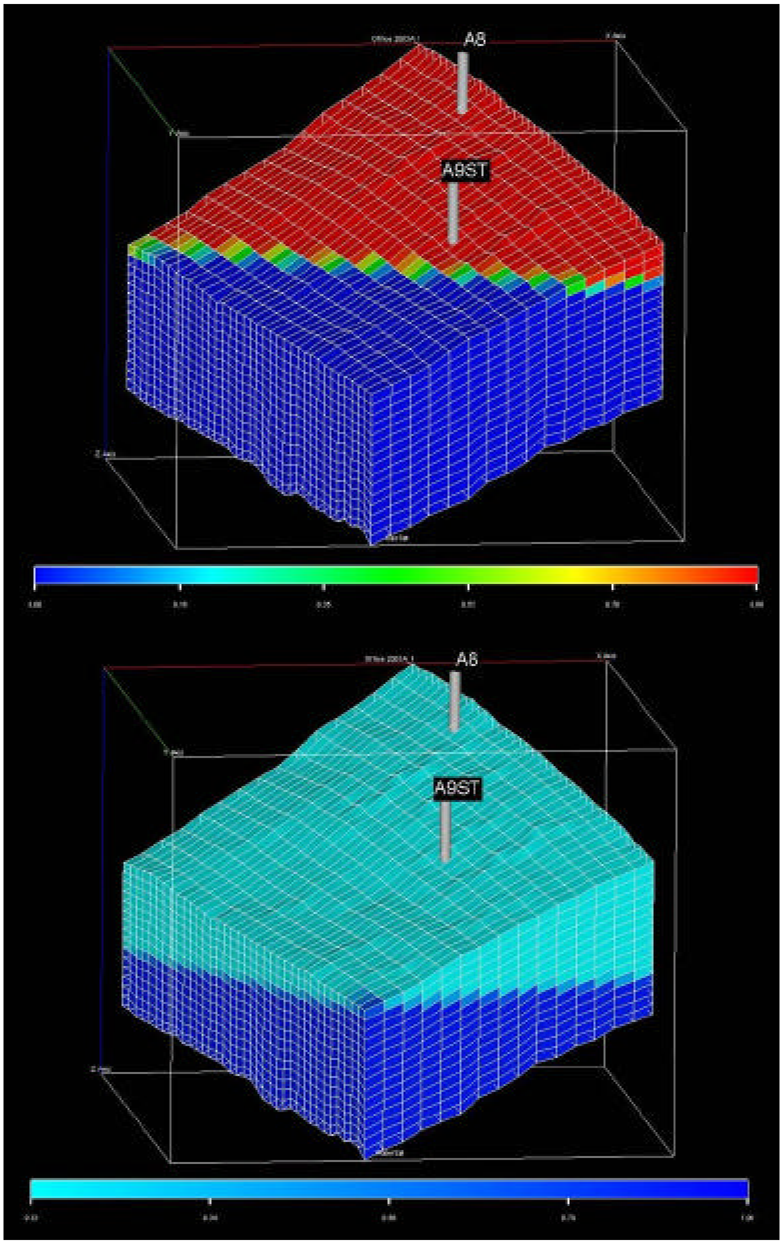

Figure 6.2: Three-dimensional rendering of the corner-point finite-difference grid used in the numerical simulations of fluid production and pressure depletion in the GNP2RB reservoir. The upper panel shows the spatial distribution of gas saturation generated by imposing vertical capillary equilibrium away from the gas-oil contact. The lower panel shows the spatial distribution of water saturation generated by imposing capillary equilibrium away from the water-oil contact.

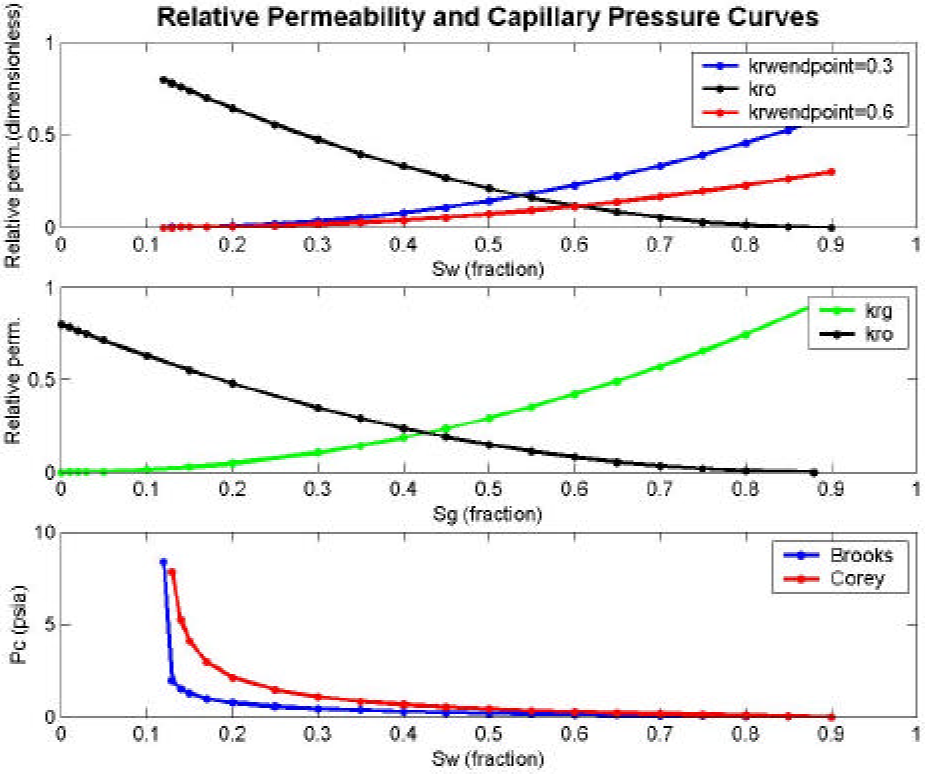

Figure 6.3: Water-oil relative permeability (upper panel), Gas-oil relative permeability (middle panel) and capillary pressure (lower panel) curves used in the simulations of multi-phase fluid-flow in the GNP2RB reservoir. The red and blue curves in the upper and lower panels describe perturbations of the reference relative permeability and capillary pressure curves used to assess the sensitivity of the simulations of fluid production to a change of rock-fluid properties.

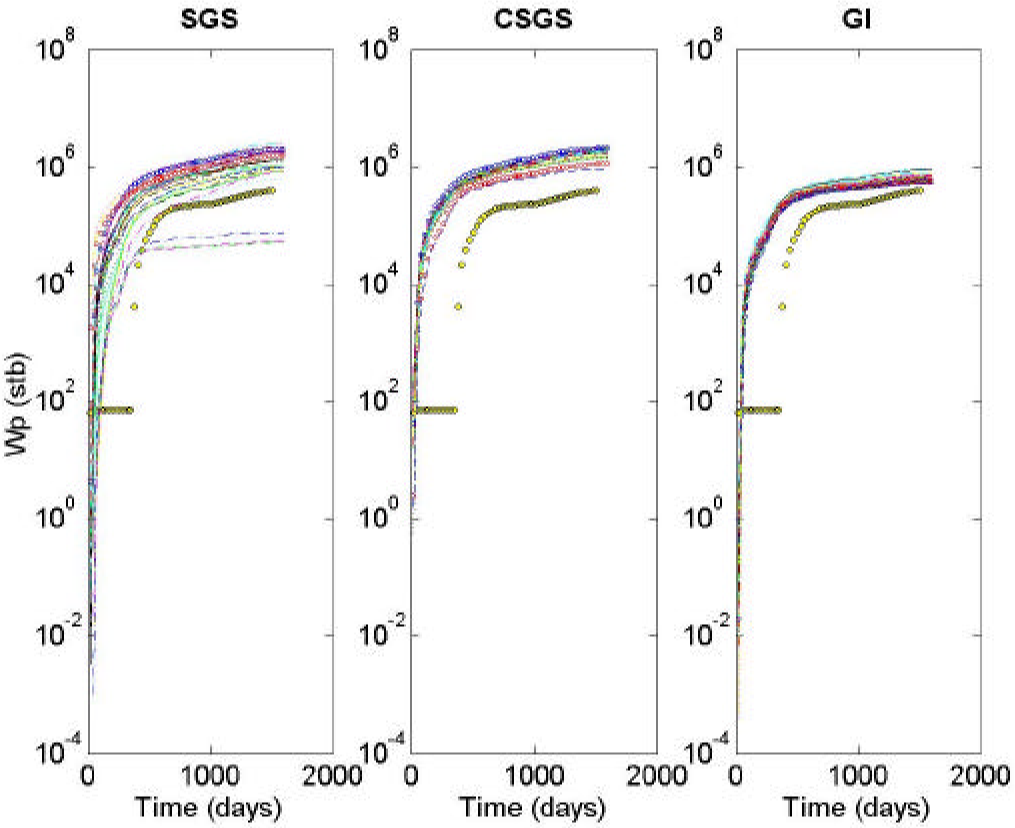

Figure 6.4: Comparison of the time evolution of measured and numerically simulated cumulative water production after the onset of production. Actual measurements of water production are identified with yellow dots. Each panel describes the cumulative water production numerically simulated for thirty independent stochastic realizations of porosity and permeability in the GNP2RB reservoir using sequential Gaussian simulation (SGS), collocated co-simulated sequential Gaussian simulation (CSGS), and geostatistical inversion (GI).

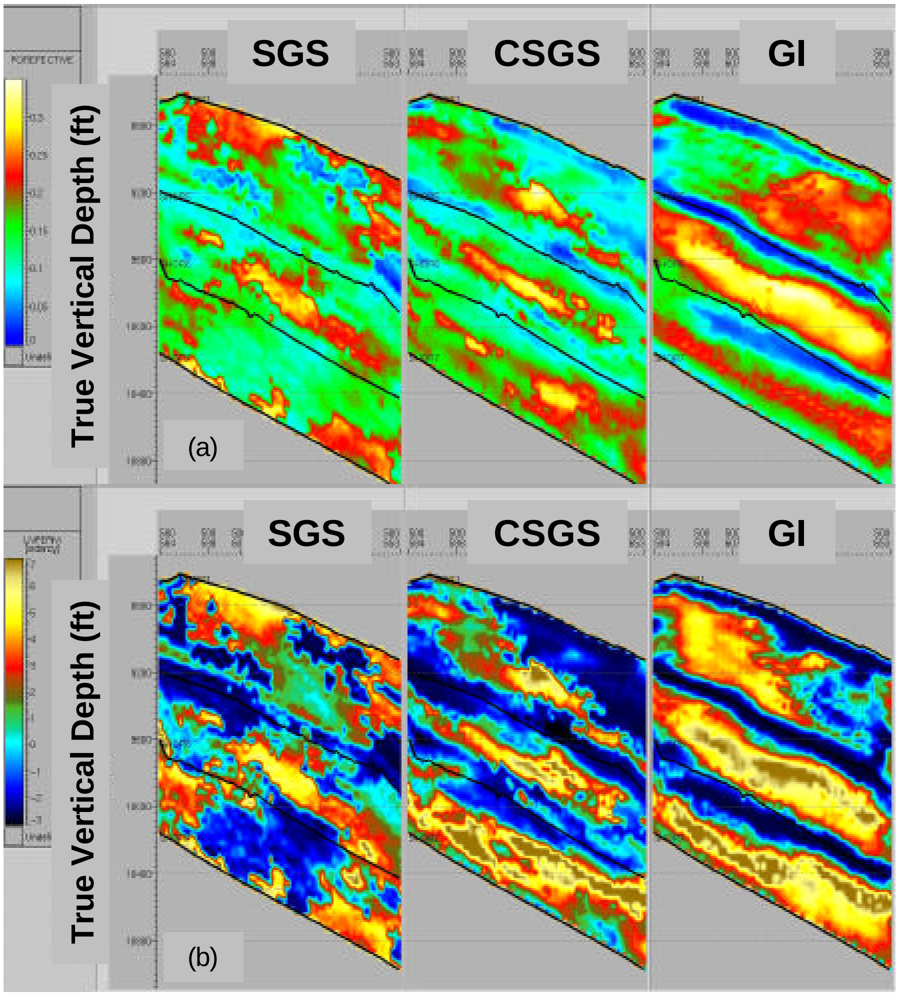

Figure 6.5: Cross-section views of one spatial realization of inter-well porosity and one realization of logarithm of permeability obtained with three different geostatistical techniques at a vertical resolution of 4ms. Panel (a) shows low values of porosity in blue and high values in yellow. From left to right, the figure shows inter-well porosity distributions rendered by sequential Gaussian simulation, collocated co-simulated sequential Gaussian simulation, and geostatistical inversion. Panel (b) shows low values of logarithm of permeability in dark blue and high values in yellow. From left to right, the figure also shows inter-well logarithm of permeability distributions rendered by sequential Gaussian simulation, collocated co-simulated sequential Gaussian simulation, and geostatistical inversion.

Chapter 7: Uncertainty Analysis and Variability of Dynamic Behavior

It has been recognized that history matching is not only a computationally challenging problem but is also riddled with non-uniqueness. Non-uniqueness means that there are multiple realizations of model parameters that honor the measured time records of fluid production (Landa et al., 2003). Therefore, it is not only desirable to estimate reservoir models that entail an acceptable agreement with the measured time records of fluid production but also to quantify their corresponding uncertainty.

7.1 Sensitivity Study of the Static Petrophysical Models

Figures 7.1, 7.7, and 7.9 show Box plots (Box et al., 1994) of normalized cumulative water production constructed with the simulated time record of fluid production for 30 independent realizations of porosity and permeability. In a Box plot (Box et al., 1994), the variability of a prediction is measured by the length of vertical boxes. Biases are detected when the median value significantly departs from the true value, or when the length of the box does not include the truth case (Varela et al., 2002).

Figure 7.1 summarizes the sensitivity analyses performed for the base cases described in Table 7.1. We measure the variability of the simulations of dynamic fluid production by making perturbations to the spatial distributions of porosity and permeability. In that figure, base cases describe the normalized cumulative water production simulated with a homogeneous reservoir model and with thirty independent reservoir models constructed with SGS, CSGS, and GI.

Average porosity and permeability values of 27% and 354 mD, respectively were estimated from the probability density functions of porosity and permeability constructed with well-log data after applying a discriminator for sands. For this homogeneous reservoir case, the simulated time records of fluid production agree closely with the actual measurements. The reason for such a good agreement is that the correlation analyses performed on every PVT parameter were done based on this homogeneous model. Calculations were also performed to quantify the degree of heterogeneity of the reservoir. Dykstra and Parsons (1950) described a method to quantify the degree of heterogeneity of a reservoir based on rock-core permeability data. For the study under consideration, the coefficient of permeability variation, also known as the Dykstra-Parson coefficient, is equal to 0.8645. By comparison, a homogeneous reservoir entails a coefficient of permeability variation that approaches zero whereas an extremely heterogeneous reservoir entails a coefficient of permeability variation that approaches one.

Figure 7.2 shows a comparative analysis performed to demonstrate that when using homogeneous models different from that used to perform the PVT analyses the match between the simulated and measured time records of fluid production is modified considerably. Among the disadvantages of simulating the reservoir as a homogeneous model, we can consider: (a) the heterogeneity patterns are not properly captured, and (b) the match with well logs is not acceptable.

On the other hand, the time records simulated from SGS reservoir models, generated through the interpolation of well logs, do not agree with the actual measurements. Reservoir models constructed with co-simulation entail considerably less spread in the corresponding time records of fluid production than reservoir models constructed with SGS. This exercise indicates that the use of seismic amplitude data has a positive impact on the constructed reservoir models. However, geostatistical inversion provided the most accurate and least biased simulations of production measurements including cumulative gas production and pressure depletion.

The bottom panel of Figure 7.1 shows Box plots of the global least-squares misfit between the measured and numerically simulated time records of cumulative water production for well A9ST. The misfit is calculated over a time segment of 4.3 years after the onset of production, and considers only spatial distributions of porosity and permeability constructed with SGS, CSGS, and GI (Base cases in Table 7.1). Specifically, the global least-squares misfit is computed with the equation

$$U(t_t) = \frac{1}{t_t}\int_{t=0}^{t=t_t} \left[d_{case}(t) - d_{caseT}(t)\right]^2 dt \, , \tag{7.1}$$

where $d_{case}(t)$ is the simulated cumulative water production, $d_{caseT}(t)$ is the measured cumulative water production, and t_t is total simulation time (1599 days). Figure 7.1 indicates that the time predictions associated with reservoir models constructed with geostatistical inversion are the most accurate and least biased.

Figures 7.3 and 7.4 represent an alternative way to compare the simulated results. Both figures are composed of four panels. The first and third panels show the cumulative production of the time records measurements for the thirty different geostatistically inverted fluid-flow simulation results, and the second and four panels display the standard deviation chart of the grouped responses in data (simulation results). The standard deviation chart (Montgomery, 1991) defines: a) a center line (CL) at the standard deviation average value of the group of data, and b) upper and lower control limits (UCL and LCL, respectively). The limits are placed at a distance ± three times the estimate of the average value of standard deviation on either side of the center line, respectively. Observing points outside the limits, it is evidence that the process is not in control. By using the geostatistically inverted models, regardless the analyzed fluid production variable, all points are within the control limits, so the variability within subgroups is reduced by constraining the inversion technique with the use of seismic information. By contrast, Figures 7.5 and 7.6 compare the statistical properties of the reservoir models constructed with sequential Gaussian simulation.

Seven sensitivity analyses were carried out in this dissertation to further appraise the accuracy and reliability of reservoir models constructed with geostatistical inversion. Table 7.1 summarizes the various exercises of sensitivity analysis designed to appraise various forms of spatial variability in the porosity and permeability models, whereas Table 7.2 summarizes the exercises of sensitivity analysis designed to assess various forms of perturbations of rock-fluid properties.

Several rock-fluid parameters can have a substantial impact on the dynamic behavior of the reservoir. However, given that the main fluid production mechanism in the GNP2RB reservoir is water-drive, for the sensitivity analysis at hand we chose to focus our attention to perturbations of both the end-point of water relative permeability and the imbibition water-oil capillary pressure curves.

In Figure 7.7, Sensitivity Analysis No. 1 indicates that the most reliable simulations of time records of fluid production are associated with geostatistically inverted reservoir models. Often, standard geostatistical simulation procedures remain highly sensitive to both the assumed semi-variogram model (and parameters thereof) and to the relative location and number of available wells. By contrast, geostatistical inversion relies heavily on the seismic amplitude variations between wells and as such, is less sensitive to the choice of semi-variogram model and related parameters as well as to the number and location of the input wells. We used spherical semi-variograms to model the spatial variability of porosity and logarithm of permeability, and adjusted the corresponding sills to a normalized value of 0.5 for each litho-type (sands and shales). Moreover, Sensitivity Analysis No. 1 was performed by changing the lateral range of the semi-variograms from 1400 ft (427 m) to 750 ft (229 m). Figure 7.8 graphically shows the impact of changing the range of the lateral semi-variogram on the spatial distributions of porosity constructed with two different geostatistical techniques (SGS and GI). Results indicate that spatial distributions constructed with GI are less sensitive to the choice of semi-variogram model than spatial distributions constructed with SGS.

Gambús and Torres-Verdín (2002) showed that geostatistical inversion could be used to adjust the vertical resolution of the simulated reservoir models anywhere between the vertical resolutions of well logs and seismic amplitude data. Sensitivity analysis No. 2 in Figure 7.7 shows Box plots of normalized cumulative water production for reservoir models constructed with a vertical resolution of 4 ms (seismic vertical resolution), 2 ms, and 1 ms. Results indicate that the spread and bias of the simulated time records of water production remain relatively unaffected by the choice of vertical sampling interval. A slight, albeit inconclusive bias in the time records of fluid production ensues when increasing the vertical resolution of the realizations of porosity and permeability.

For Sensitivity Analysis No. 3, the intention was to explore the variability of the simulated time records of fluid production due to a perturbation in the assumed porosity-permeability correlation. Such an exercise was also intended to assess whether an erroneous porosity-permeability correlation could significantly affect the simulated time record of fluid production, especially when compared to the corresponding variability of fluid production due to spatial variability of porosity and permeability. To this end, we enforced a 50% perturbation in the porosity-logarithm of permeability rock-core trend shown in Figure 2.5. Results from this exercise indicate that permeability has a strong impact on fluid production; small values of permeability not only reduce the uncertainty but also increase the bias of the simulated time records of fluid production.

Sensitivity Analysis No. 4, also described in Figure 7.7, summarizes the results of exercises performed to assess the influence of errors in (a) the assumed porosity-acoustic impedance correlation, (b) the assumed permeability-acoustic impedance correlation, or (c) both of them. As indicated in Figure 7.7, the largest variation on the simulated time record of fluid production is obtained for the case of a perturbation in the permeability-acoustic impedance correlation (refer to Table 7.1 for a definition of the cases).

Results from Sensitivity Analysis No. 5 are graphically described in Figure 7.9. This is an exercise intended to quantify the influence of variations of permeability anisotropy on the simulated time records of fluid production and pressure depletion. To this end, we consider values of 1, 0.5, and 0.1 for the assumed ratio between vertical and horizontal permeability (K_V/K_H). The simulations indicate that permeability anisotropy has a significant influence on the time records of fluid production. A 50% reduction in the value of vertical permeability entails a sizable spread in the simulated time records of fluid production. Moreover, when the vertical permeability decreases to 10% of its original value the simulated time records of fluid production exhibit a considerable bias.

Sensitivity Analysis No. 6 is intended to quantify the influence of the estimated seismic wavelet on the simulated time records of fluid production. Results form this exercise are graphically described in Figure 7.9. Time records of fluid production and pressure depletion were simulated for geostatistically inverted spatial distributions of porosity and permeability obtained separately with the two wavelets described in Figure 3.1. This exercise indicates that perturbations in the assumed wavelet increase the bias of the predicted time records of cumulative water production.

7.2 Fluid Sensitivity Study

Finally, Sensitivity Analysis No. 7, described in Figure 7.10, is intended to assess the effect of a perturbation of the fluid and rock-fluid properties on the simulated time records of fluid production. Comparison of the latter results against those of the previous cases shows that the spread and bias of the predictions are not significant.

Table 7.1: Summary of the nomenclature used to identify the numerical experiments conducted in this dissertation to study the sensitivity of the time records of fluid production measurements to spatial variations of porosity and permeability.

Sensitivity Analysis	Case	Homogeneous	Sequential Gaussian Simulation of well –logs	Collocated co-simulated sequential gaussian simulation of well-logs and AI	Geostatistical Inversion: well –logs + AI + seismic data
Key Control	Base Cases	H	SGS	CSGS	GI
Sensitivity Analysis No. 1: Lateral range of the variogram	Rx=1400 ft		SGS	C-1	GI-1
	Rx=750 ft			C-2	GI-2
Sensitivity Analysis No. 2: Seismic time sampling interval	Δt=4ms				GI-1
	Δt=2ms				GI-3
	Δt=1ms				GI-4
Sensitivity Analysis No. 3: $f - k$ **Correlation (50% - perturbation trend)**	g =1; a =7.68; b =7.24				GI-1
	g =1; a =3.84; b =3.62				GI-5
Sensitivity Analysis No. 4: Error in the correlation $f - AI$ **(3% - perturbation trend)**	$R^2 = -0.95$				GI-1
	$R^2 = -0.92$				GI-6
Error in the correlation $k - AI$ **(9% - perturbation trend)**	$R^2 = -0.91$				GI-1
	$R^2 = -0.84$				GI-7
Error in the correlations $f, k - AI$	COMBINATION OF GI-6, AND GI-7				GI-8
Sensitivity Analysis No. 5: Vertical to horizontal permeability ratio (Kv/Kh)	Kv/Kh = 1				GI-1
	Kv/Kh = 0.5				GI-9
	Kv/Kh = 0.1				GI-10
Sensitivity Analysis No. 6: Wavelets	Wavelet No. 1				GI-1
	Wavelet No. 2				GI-11

Table 7.2: Summary of the nomenclature used in this dissertation to identify the numerical experiments conducted to assess the sensitivity of the time records of fluid production measurements to fluid and rock-fluid properties.

Sensitivity Analysis No. 7	**CASE**	**Geostatistical Inversion:** **Well –logs + AI + seismic data**
Changes in end-point water relative permeability (100% - perturbation)	k_{rw}^{o} =0.3	GF-1
	k_{rw}^{o} =0.6	GF-2
Imbibition capillary pressure curve	Brooks	GF-1
	Corey	GF-3

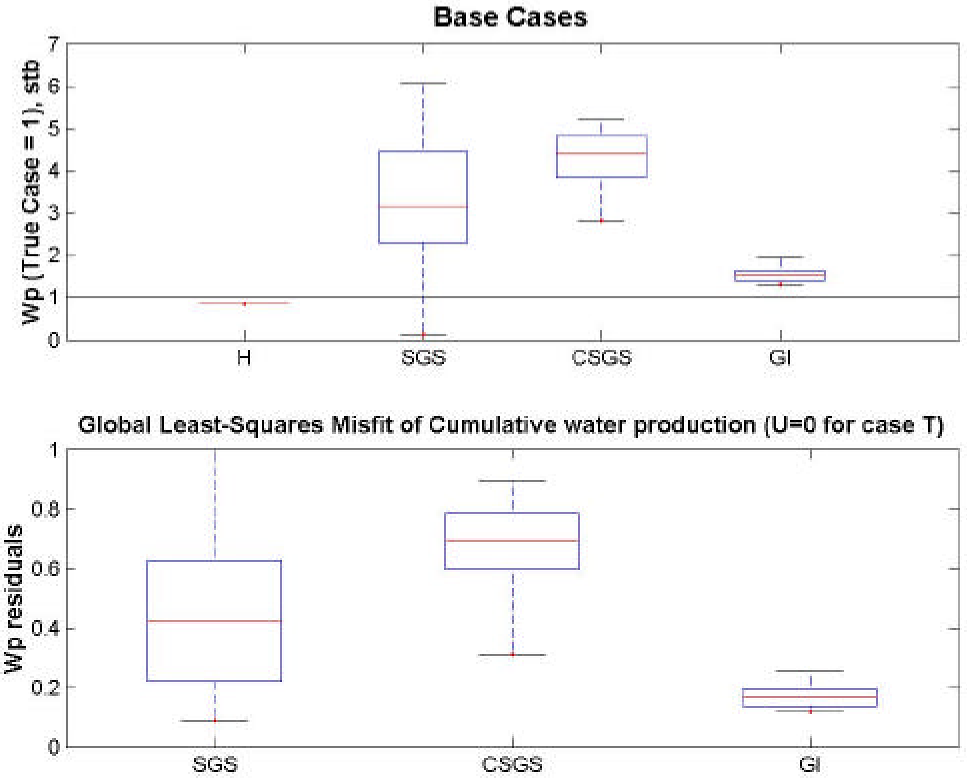

Figure 7.1: Box plots: The top panel shows the Box plots of normalized cumulative water production for the base cases referred in Table 7.1. The actual measurement of total cumulative water production is represented by the horizontal black line (Wp = 1.0). The bottom panel shows Box plots of the global least-squares misfit (U) calculated for the simulations of time records of cumulative water production measurements rendered by geostatistical inversion (case GI, refer to Table 7.1). The global misfit is computed with the formula, $U(t_t) = \frac{1}{t_t}\int_{t=0}^{t=t_t} [d_{case}(t) - d_{caseT}(t)]^2 dt$ where $d(t)$ is cumulative water production in well A9ST and t_t is total time of simulation (1599 days). Box plots were constructed using numerical simulations of water production for thirty independent realizations of inter-well porosity and permeability.

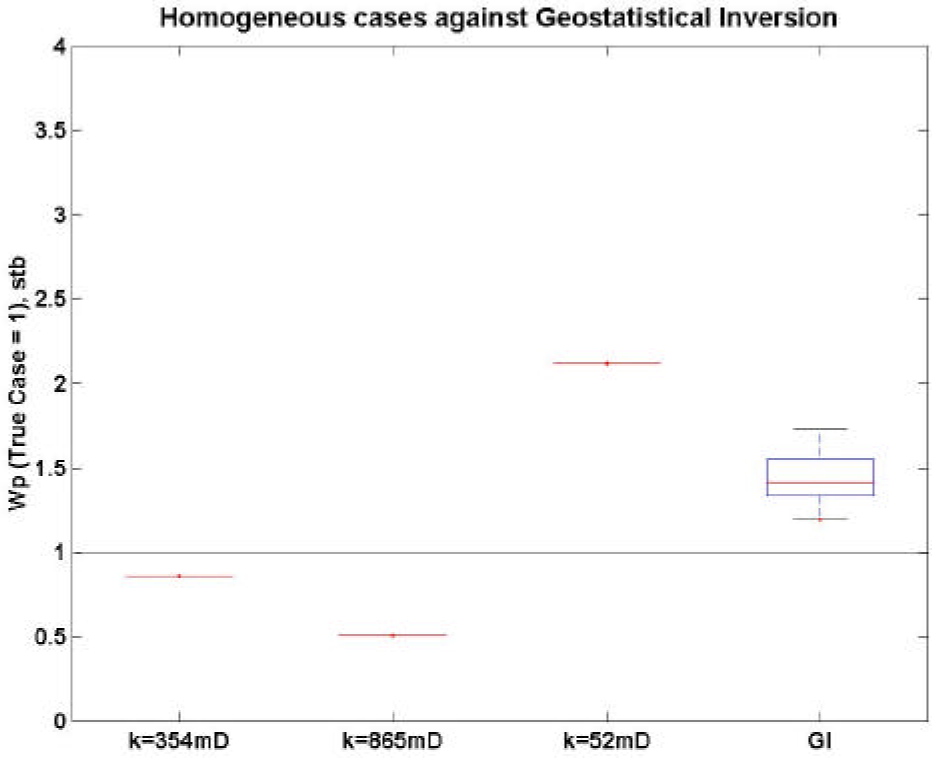

Figure 7.2: Box plots of normalized cumulative water production for different homogeneous cases compared to geostatistical inversion. The homogeneous results were generated with an average porosity value of 27% and different absolute permeabilities (i.e., k=354 mD [case H in Figure 7.1], k=865 mD, and k=52 mD). A Box plot for the case of geostatistical inversion was constructed using numerical simulations of water production for thirty independent realizations of inter-well porosity and permeability (refer to Figure 7.1). The actual measurement of total cumulative water production is represented by a horizontal black line (Wp = 1.0).

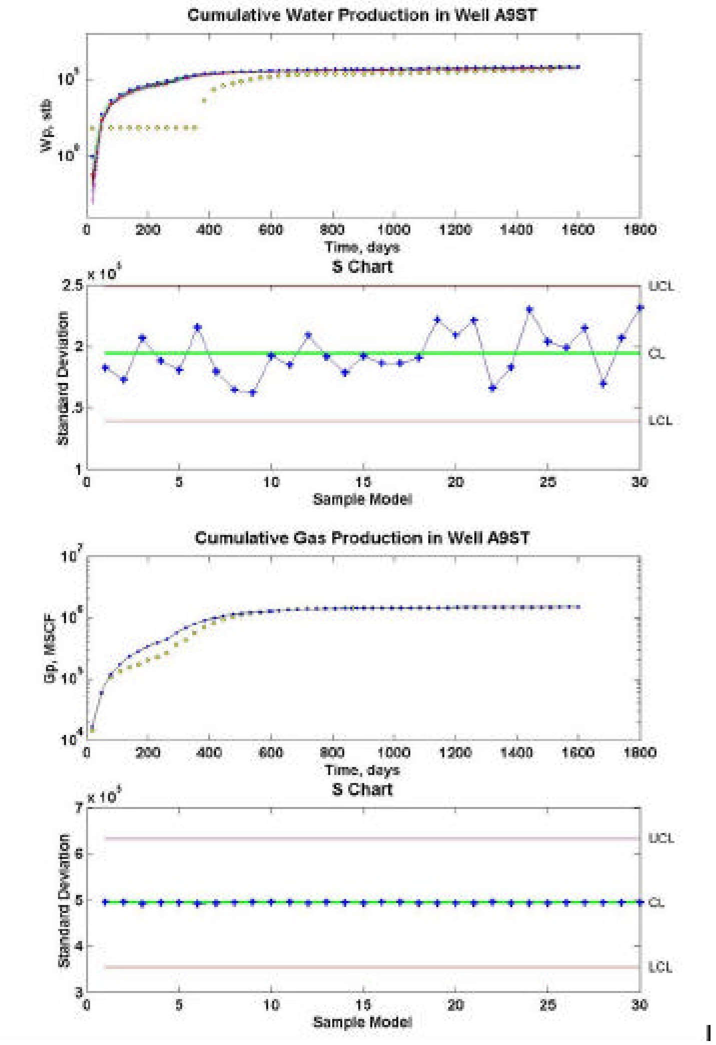

Figure 7.3: Comparison of the time evolution of measured and numerically simulated cumulative water production using geostatistical inversion (first panel from top to bottom). In the second panel, we have the standard deviation chart of the simulated cumulative water production. A green line is showing the average standard value for the data group (thirty models) and the two horizontal red solid lines above and below the average value are at a distance of ± three times the average standard deviation value (UCL and LCL, respectively). Comparison of the time evolution of measured and numerically simulated cumulative gas production using geostatistical inversion is the third panel in this figure. As fourth panel, we have the standard deviation chart of the simulated cumulative gas production. Actual measurements of cumulative water and gas production are identified with yellow dots.

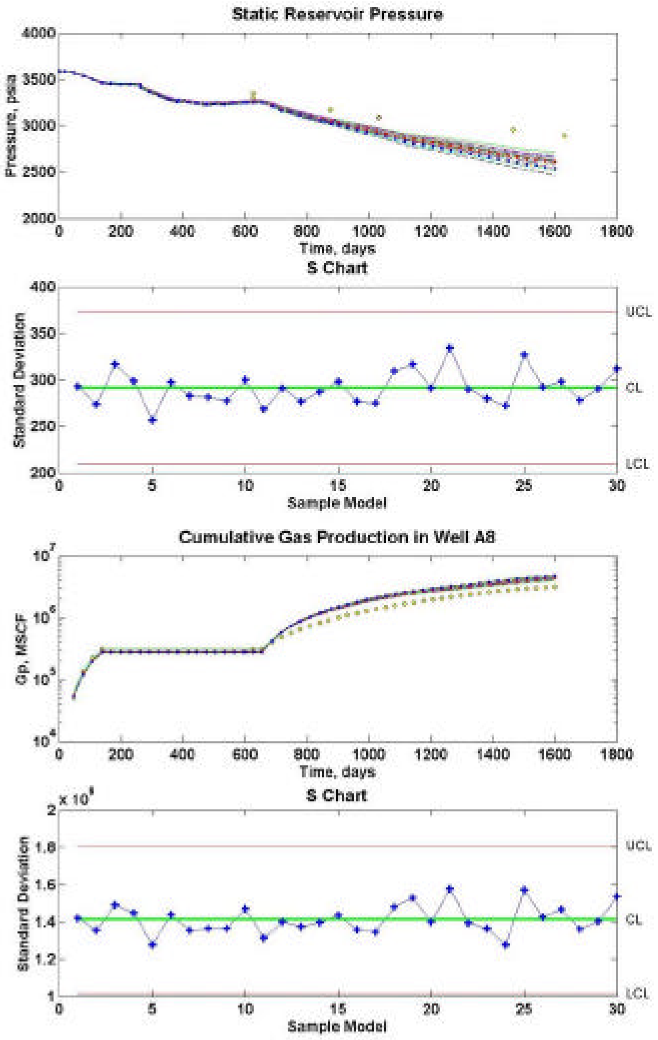

Figure 7.4: Comparison of the time evolution of measured and numerically simulated static reservoir pressure using geostatistical inversion (first panel from top to bottom). In the second panel, we have the standard deviation chart of the simulated static pressure. A green line is showing the average standard value for the data group (thirty models) and the two horizontal red solid lines above and below the average value are at a distance of ± three times the average standard deviation value (UCL and LCL, respectively). Comparison of the time evolution of measured and numerically simulated cumulative gas production using geostatistical inversion is the third panel in this figure. As fourth panel, we have the standard deviation chart of the simulated cumulative gas production. Actual measurements of cumulative water and gas production are identified with yellow dots.

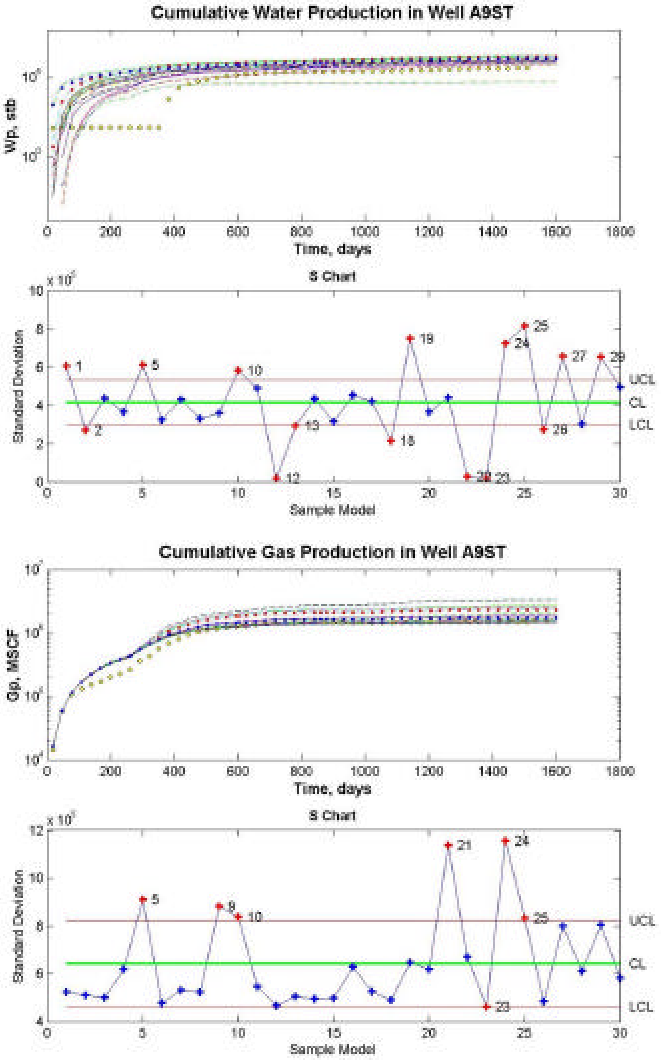

Figure 7.5: Comparison of the time evolution of measured and numerically simulated cumulative water production using sequential Gaussian simulation (first panel from top to bottom). In the second panel, we have the standard deviation chart of the simulated cumulative water production. A green line is showing the average standard value for the data group (thirty models) and the two horizontal red solid lines above and below the average value are at a distance of ± three times the average standard deviation value (UCL and LCL, respectively). Comparison of the time evolution of measured and numerically simulated cumulative gas production using geostatistical inversion is the third panel in this figure. As fourth panel, we have the standard deviation chart of the simulated cumulative gas production. Actual measurements of cumulative water and gas production are identified with yellow dots.

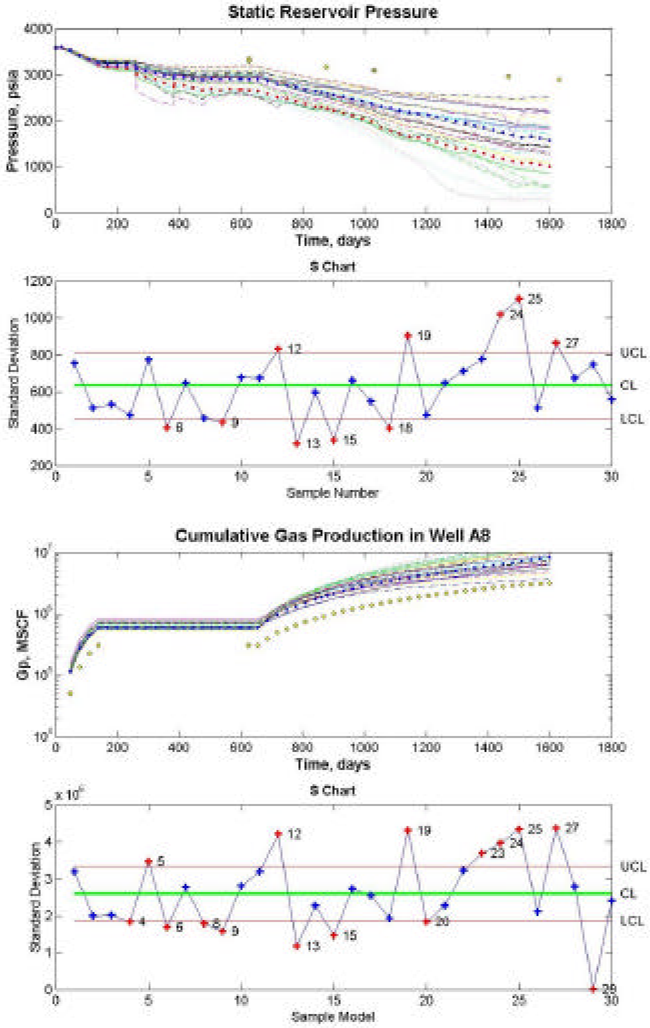

Figure 7.6: Comparison of the time evolution of measured and numerically simulated static reservoir pressure using sequential Gaussian simulation (first panel from top to bottom). In the second panel, we have the standard deviation chart of the simulated static pressure. A green line is showing the average standard value for the data group (thirty models) and the two horizontal red solid lines above and below the average value are at a distance of ± three times the average standard deviation value (UCL and LCL, respectively). Comparison of the time evolution of measured and numerically simulated cumulative gas production using geostatistical inversion is the third panel in this figure. As fourth panel, we have the standard deviation chart of the simulated cumulative gas production. Actual measurements of cumulative water and gas production are identified with yellow dots.

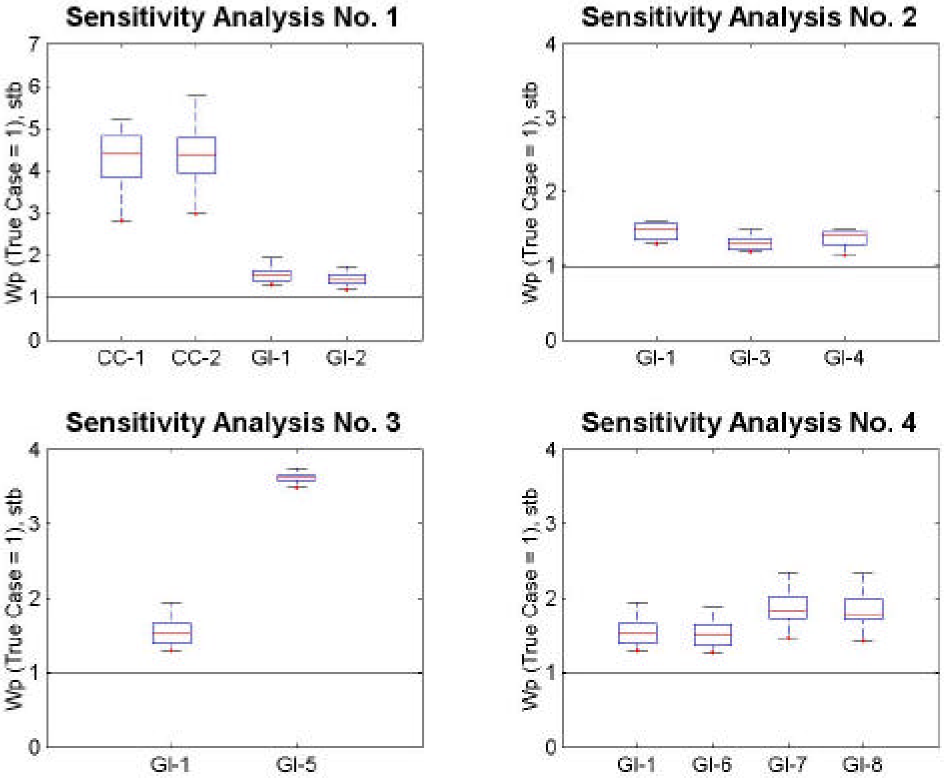

Figure 7.7: Box plots of normalized cumulative water production for various cases of sensitivity analysis. Box plots were constructed using numerical simulations of water production for thirty independent realizations of inter-well porosity and permeability. See Table 7.1 for a definition of the cases. The actual measurement of total cumulative water production is represented by the horizontal black lines (Wp = 1.0).

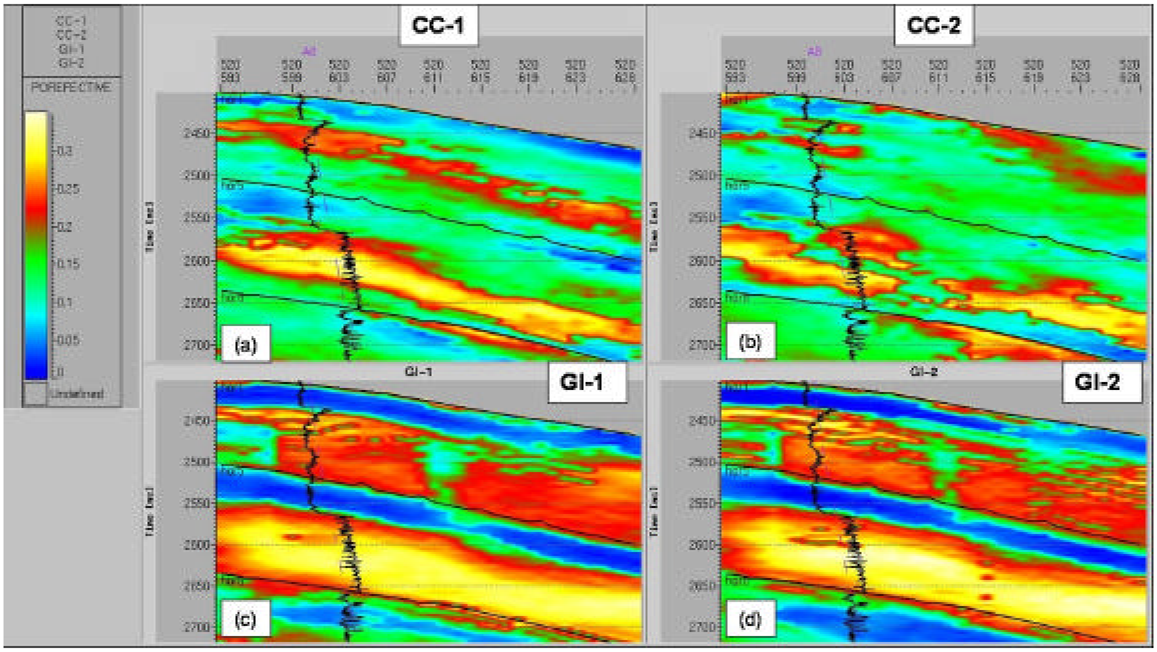

Figure 7.8: Graphical comparison of the spatial distributions of porosity constructed with Gaussian collocated co-simulation (CSGS) (Panels a and b) and geostatistical inversion (GI) (Panels c and d) in the seismic time domain. Panels a and c describe porosity distributions constructed with a spherical semi-variogram model of lateral ranges equal to 1400 ft, while Panels b and d describe porosity distribution constructed with a variogram model of lateral ranges equal to 750 ft (refer to Table 7.1 for a description of the cases). Although the Gaussian collocated co-simulation approach uses the seismic acoustic impedance inversion as secondary variable in the input of such a technique, it is evident that standard geostatistical interpolations (CSGS) are highly sensitive to a change of variogram properties; i.e. change of horizontal range (x,y), while geostatistical inversion is marginally sensitive to a change of variogram properties.

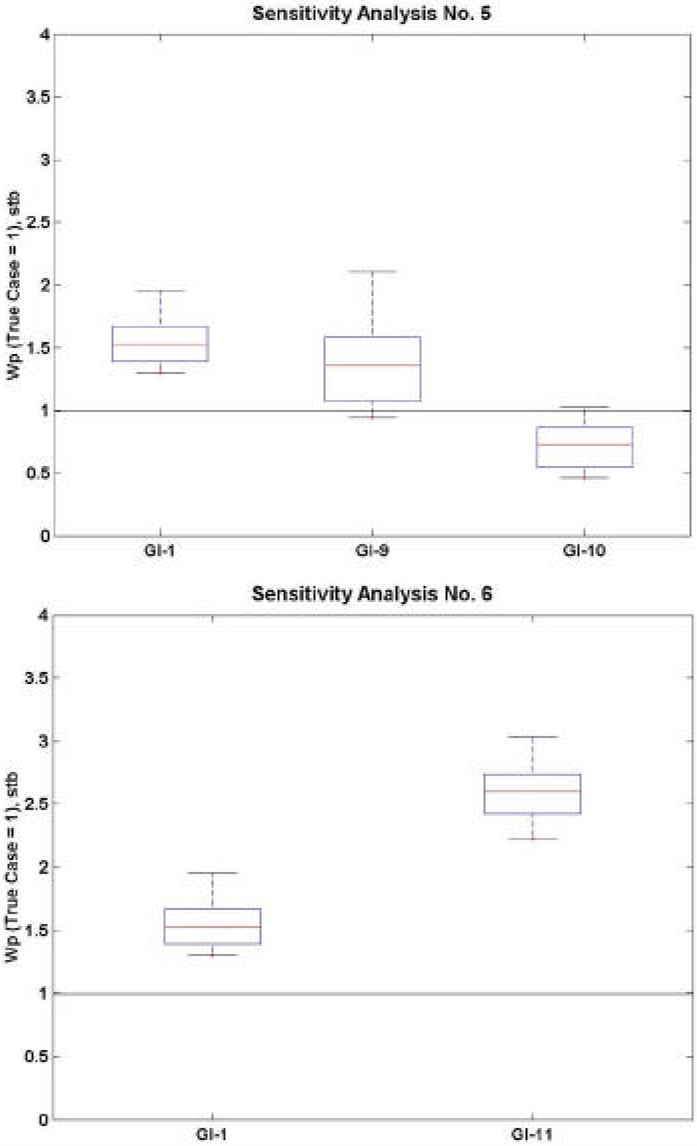

Figure 7.9: Box plots of normalized cumulative water production for various cases of sensitivity analysis. Box plots were constructed using numerical simulations of water production for thirty independent realizations of inter-well porosity and permeability. See Table 7.1 for a definition of the cases. The actual measurement of total cumulative water production is represented by the horizontal black lines (Wp = 1.0)

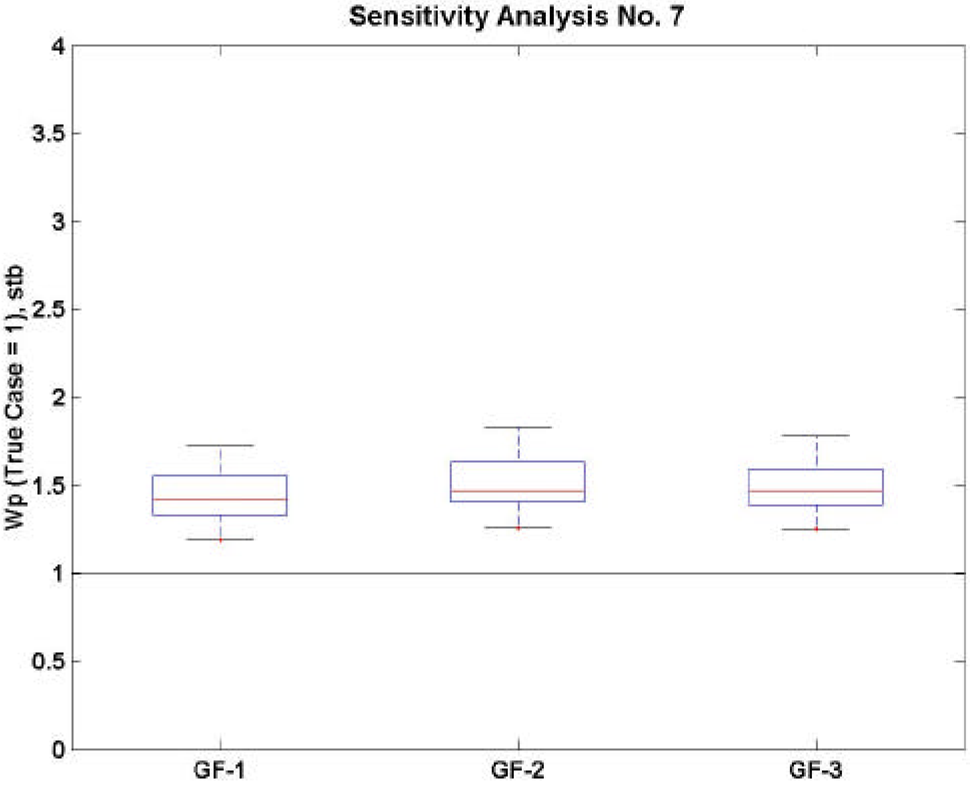

Figure 7.10: Box plots of normalized cumulative water production for various cases of sensitivity analysis. Box plots were constructed using numerical simulations of water production for thirty independent realizations of inter-well porosity and permeability. See Table 7.2 for a definition of the cases. The actual measurement of total cumulative water production is represented by the horizontal black lines (Wp = 1.0).

Chapter 8: Discussion and Conclusions

8.1 Discussion

The objective of this dissertation is to assess data sensitivity and uncertainty in the construction of static spatial distributions of porosity and permeability in the GNP2RB reservoir. To appraise reservoir models constructed with geostatistical inversion (i.e. models that honor seismic amplitude data and well logs) and conventional geostatistical simulation techniques (i.e. models that honor well logs), we performed ninety-one conditional fluid-flow simulations (Base Cases; refer to Table 7.1). The approach described in this dissertation is a step toward establishing a systematic procedure to assess non-uniqueness in the predictions of time records of fluid production and reservoir pressure depletion.

The interquartile range (IQR) indicates the variability of a prediction; it is measured by equation (8.1) and is represented by the size of the Box plots (Box et al., 1994). The median value of the sample data (i.e. normalized cumulative water production) is significant because it quantifies whether or not a bias exists in the simulated results. To calculate the interquartile range, we made use of the equation

$$IQR = Percentile_{75\%} - Percentile_{25\%} \quad . \tag{8.1}$$

Regardless of the various sensitivity analyses performed to assess the influence of spatial interpolation parameters and rock-fluid properties, geostatistical inversion provided the least biased and most accurate predictions, with a median value of normalized cumulative water production very close (1.532) to the true measured value (1.00). To compare the simulated results among the various geostatistical procedures implemented in this dissertation to construct reservoir models, and to analyze each sensitivity case with respect to the best reservoir construction method (GI), we calculated the ratio between the interquartile differences per case related to the interquartile range obtained with GI, i.e.,

$$\Delta IQR / IQR_{GI} = 100 * (IQR_{case} - IQR_{GI}) / IQR_{GI} \quad . \tag{8.2}$$

Tables 8.1 and 8.2 summarize the statistical indicators (median, percentiles, interquartile range (IQR), and interquartile differences) calculated to assess the uncertainty of the simulated time records of fluid production and pressure depletion. The benefits of incorporating seismic amplitude data in the construction of reservoir models of porosity and permeability are confirmed by the cumulative water production entailed by geostatistical inversion. By contrast, results indicate that not only a bias but also high uncertainty is associated with reservoir models constructed solely with the use of SGS and CSGS, where the median and the interquartile differences are 3.1, 4.4, 717%, and 266%, respectively (Base Cases; refer to Table 8.1).

For most of the sensitivity analyses performed with geostatistical inversion, results exhibited a reduction of uncertainty in the forecast of water production (negative interquartile differences in Table 8.1). The worst outcome was produced when the relationship porosity-permeability was perturbed by 50% with respect to that of the reference rock-core trend (GI-5; refer to Table 8.1). Uncertainty was drastically reduced because of the uniform and low values of permeability ($\Delta IQR / IQR_{GI}$=-72.1%); however, we also observed a measurable bias in the ensuing results (median=3.616). On the other hand, when the linear relationship between logarithm of permeability and acoustic impedance was perturbed with a reduction of the correlation coefficient from -0.91 to -0.84 (GI-7; refer to Table 8.1), we found that the differences in Box sizes increased by 15.7%.

Although the bias was not significant when reducing the vertical permeability to half the horizontal permeability (k_V/k_H=0.5, GI-9; refer to Table 8.1), the spread increased to a maximum (96.3%) with respect to the geostatistical inverted base case (GI-1; refer to Table 8.1), and the median value of 1.356 remained close to the median reference value of 1.53. By contrast, when vertical permeability was decreased to about 10% of the value of horizontal permeability (k_V/k_H =0.1, GI-10; refer to Table 8.1), the spread decreased to 21.4% but the bias became significant (median=0.73).

Another important sensitivity analysis was performed to assess the influence of the estimated wavelet on the variability and uncertainty of fluid production. By assuming a different length and phase for the seismic wavelet the spread of the simulations was estimated at 20% but the bias was significant (median=2.602).

From the results described above, it follows that the combined use of seismic amplitude data, well logs, and rock-core measurements drastically reduced the uncertainty and the bias in the simulated time records of fluid production and pressure depletion. However, we observed significant biases in the simulations of cumulative water production when making perturbations to the spatial distributions of porosity and permeability (Table 8.1; Figures 7.1, 7.7, and 7.9). Special attention and care must be exercised when (a) estimating permeability and establishing a relationship between porosity and acoustic impedance, (b) choosing the value of vertical to horizontal permeability ratio (anisotropy), and (c) estimating the wavelet from seismic-amplitude data and well logs.

Varela et al. (2002) stated that biased predictions of fluid recovery could be associated with pure fluid-flow phenomena to which post-stack seismic data remain insensitive. Therefore, we considered perturbations of the fluid and rock-fluid properties (i.e. end-point water relative permeability, and the water-oil imbibition capillary pressure curve) to assess the influence of these parameters on the reliability and accuracy of the predictions of fluid production. For the latter numerical experiments, we considered the geostatistical inversion case GF-1 (Table 7.2) as the base case for comparison purposes (median equal to 1.416). A change in the water end-point relative permeability (GF-2; refer to Table 7.2, Figure 7.10) did not modify the median (1.473) and the length of the Box increased by a small ratio of 4.5%. On the other hand, a change in the imbibition capillary pressure curve entailed a reduction in uncertainty (Box plot size) of the order of -7.2% while the median remained constant (1.47; refer to Table 8.2).

In summary, the results described in this dissertation consistently indicate that, for the reservoir under consideration, spatial variations of porosity and permeability remain the primary controls of the time behavior of fluid production and pressure depletion. This conclusion cannot be generalized to the analysis of other types of hydrocarbon reservoirs. However, the method described in this dissertation can still be used to systematically assess the influence of a variety of petrophysical, fluid, and rock-fluid properties, in light of spatial variations of porosity and permeability. The sensitivity analyses performed in this dissertation embody a systematic method to quantify the added value of seismic amplitude data in the inference of spatial variations of porosity and permeability.

8.2 Conclusions

The following is an itemized list of the most important conclusions stemming from this study:

(1) Post-stack seismic amplitude data improve the description of inter-well spatial distributions of reservoir porosity and permeability when the latter parameters exhibit a high degree of correlation with acoustic impedance.

(2) A detailed petrophysical analysis is necessary to assess whether acoustic impedance uniquely correlates with specific petrophysical parameters required in the construction of reservoir models. Moreover, the degree of correlation between acoustic impedance and porosity and permeability should be independent of reservoir thickness in the presence of wavelet tuning as well as of variations of water saturation and shale concentration.

(3) The methodology considered in this dissertation to construct spatial distributions of porosity and permeability would be difficult, if not impossible to implement in thin-layer, and low-porosity reservoirs where seismic amplitudes do not uniquely respond to porosity and permeability. A high degree of uncertainty in the relationship between seismic amplitudes and porosity and permeability could also exist in shaly and low-porosity sands where variations of seismic-inverted acoustic impedance alone cannot be uniquely associated with variations of porosity, permeability, shale volume, fluid saturation, and reservoir thickness.

(4) The inversion of seismic amplitudes into spatial variations of acoustic impedance considerably reduces wavelet tuning effects but does not increase the vertical resolution of seismic amplitude data.

(5) Post-stack seismic amplitude measurements introduce a high degree of inter-well heterogeneity in porosity and permeability not captured by the interpolation of well-log data with conventional geostatistical techniques. For the study considered in this dissertation, we found that the use of seismic amplitudes for estimating inter-well porosity and permeability has a substantial positive impact on the prediction of fluid production. We showed that uncertainty and bias in the prediction of reservoir production drastically decreases with the use of post-stack seismic amplitude data.

(6) Reservoir distributions of porosity and permeability constructed with geostatistical inversion entailed the most accurate and least biased predictions of reservoir production when compared to predictions performed with standard geostatistical simulation techniques.

(7) Geostatistical inversion can efficiently enforce a non-deterministic (statistical) link between acoustic impedance and porosity and permeability. Extensive sensitivity analyses of all of the variables and parameters involved in the interpolation of inter-well porosity and permeability indicated that geostatistical inversion was the most robust and reliable method for estimating inter-well distributions of porosity and permeability.

(8) For the reservoir under consideration, permeability exhibited the largest influence on the behavior of fluid production and pressure depletion with time. We also found that the perturbations to the relationship between porosity, permeability, and acoustic impedance produced significant variations in the simulated time record of fluid production. Rock-core laboratory measurements can guide the estimation of such petrophysical relationship but corrections might be necessary to account for variations in the spatial length of support of the available measurements.

(9) For the study under consideration, the degree of spatial variability of porosity and permeability was more significant than the degree of

variation of rock-fluid properties (water relative permeability, and capillary pressure) in predicting reservoir production with time.

(10) The estimation of inter-well permeability was possible because of its correlation with acoustic impedance and porosity. Quite often, a correlation between porosity and permeability does not exist. In such situations, even if a correlation exists between acoustic impedance and porosity, permeability cannot be estimated from seismic amplitude data. The estimation of inter-well permeability can only be performed with the simultaneous use of seismic amplitude data and reservoir measurements that are highly sensitive to fluid movement.

Table 8.1: Summary of the normalized statistical indicators (median, percentiles, interquartile range (IQR), and interquartile differences) considered in this dissertation to quantify uncertainty in the prediction of time records of fluid production measurements (refer to equations 8.1 and 8.2). Figures 7.1, 7.7, and 7.9 are a graphical rendering of the same results.

Sensitivity Analysis	**Case**	**Median**	**Perc75%**	**Perc25%**	**IQR**	$\Delta IQR / IQR_{GI}$**,%**
True Case: Production history	T	1	1	1	0	-----------
Base Cases	H	0.857	0.857	0.857	0	------------
	SGS	3.150	4.447	2.305	2.141	717.9
	CSGS	4.414	4.806	3.845	0.96	266.9
	GI	1.532	1.653	1.391	0.261	0
Sensitivity Analysis No. 1: **Lateral range of the semivariogram**	CC-1	4.414	4.806	3.845	0.96	266.9
	CC-2	4.384	4.758	3.944	0.814	210.9
	GI-1	1.532	1.653	1.391	0.261	0
	GI-2 = GF-1	1.416	1.554	1.335	0.218	-16.4
Sensitivity Analysis No. 2: **Seismic time sampling interval**	GI-3	1.322	1.416	1.222	0.193	-26.09
	GI-4	1.419	1.461	1.284	0.177	-32.3
Sensitivity Analysis No. 3: $f-k$ **Correlation**	GI-5	3.616	3.651	3.578	0.072	-72.1
Sensitivity Analysis No. 4: **Error in the correlation** $f - AI$	GI-6	1.512	1.64	1.356	0.284	8.47
Error in the correlation $k-AI$	GI-7	1.822	2.024	1.721	0.303	15.7
Error in the correlations $f,k-AI$	GI-8	1.783	1.985	1.709	0.276	5.72
Sensitivity Analysis No. 5: **Vertical to horizontal permeability ratio.**	GI-9	1.356	1.587	1.073	0.514	96.3
	GI-10	0.730	0.867	0.548	0.318	21.4
Sensitivity Analysis No. 6: **Wavelet**	GI-11	2.602	2.737	2.423	0.314	20.02

Table 8.2: Summary of the statistical indicators (median, percentiles, interquartile range (IQR), and interquartile differences) considered in this dissertation to quantify uncertainty in the prediction of time records of fluid production measurements (refer to equations 8.1 and 8.2). Figure 7.10 is a graphical rendering of the same results.

Sensitivity Analysis No. 7:	**Case**	**Median**	**Perc75%**	**Perc25%**	**IQR**	$\Delta IQR / IQR_{GI}$, **%**
Changes in the end-point water relative permeability	GF-2	1.473	1.635	1.407	0.228	4.52
Changes in the imbibition capillary pressure curve	GF-3	1.470	1.593	1.391	0.202	-7.29

Appendix A: Black-Oil Fluid-Flow Model

Modeling fluid-flow in a permeable porous media requires conservation of mass equations, constitutive equations, and rock-fluid relations. The conservation of mass equations for each phase are of the form

$$\frac{\partial}{\partial t}\left[f \sum_{a=1}^{n_p} r_a w_{j,a} S_a \right] + \vec{\nabla}\left[\sum_{a=1}^{n_p} r_a w_{j,a} \vec{u}_a \right] = R_j \;, \tag{A.1}$$

where the subscript j designates the component (stock tank oil, produced gas, or water), the subscript a designates the phase (oleic, gaseous, or aqueous), r is the fluid density, f is the porosity, $\vec{u}$ is the interstitial velocity, S is fluid saturation, and R is a source or sink term. The mass fractions of each phase used in this dissertation, $w_{j,a}$, are given in Table A.1 (Miller, 2000).

The constitutive equations are Darcy's law for each phase a, given by

$$\vec{u} = -\frac{k_{ra}}{m_a}\vec{\vec{k}}\left(\vec{\nabla}p_a - g_a\vec{\nabla}D_z\right), \tag{A.2}$$

where $\vec{\vec{k}}$ is the absolute permeability tensor, k_{ra} is the relative permeability of phase a, and m is viscosity of phase a. In the same equation, $g_a = \dfrac{r_a g}{g_c}$ is the specific weight of the fluid, g is the gravitational acceleration term equal to 32 ft/s^2 (9.8 m/s^2), g_c is a unit converter parameter. $\vec{\nabla}D_z$ is the direction of fluid-flow, and $\vec{\nabla}p$ is the pressure gradient.

The relationship between capillary pressure (p_c) and fluid saturation (S) is governed by

$$\begin{aligned} p_{cow} &= p_o - p_w = f(S_w), \\ p_{cgo} &= p_g - p_o = f(S_o), \end{aligned} \tag{A.3}$$

and

$$S_o + S_w + S_g = 1 \ , \tag{A.4}$$

where p_{cow} and p_{cgo} represent the imbibition water-oil capillary pressure and the drainage gas-oil capillary pressure, respectively. In equations (A.3) and (A.4), S_w, S_o, and S_g designate water, oil, and gas saturation, respectively.

The Brooks-Corey type equations are used to evaluate the fluid-flow performance of the multiphase system. Accordingly, for the drainage process (gas-oil system) the following expressions hold:

$$k_{rg} = k_{rg}^o S_D^{eg} \ , \tag{A.5}$$

$$k_{rog} = k_{ro}^o (1 - S_D)^{eo} \, , \tag{A.6}$$

and

$$S_D = \frac{S_g - S_{gc}}{1 - S_{gc} - S_{wi}} \ , \tag{A.7}$$

where k_{rg} and k_{rog} are the gas and oil-gas relative permeabilities, and k_{rg}^o and k_{ro}^o represent the gas and oil end-points relative permeability, respectively. In equation (A.7), S_{gc} is the critical gas saturation (assumed zero), and S_{wi} is the irreducible water saturation (refer to Table 6.1), S_D is the normalized saturation, and e_o and e_g are the oil and gas saturation exponents (both of them assumed equal to 2), respectively.

For the imbibition process (water-oil system), one has

$$k_{rw} = k_{rw}^{o} S_D^{ew} \ , \tag{A.8}$$

$$k_{row} = k_{ro}^{o} (1 - S_D)^{eo} \ , \tag{A.9}$$

and

$$S_D = \frac{S_w - S_{wi}}{1 - S_{wi} - S_{or}} \ , \tag{A.10}$$

where k_{rw}, k_{row} are the water and oil-water relative permeabilities, k_{rw}^{o} is the water end-point relative permeability, S_{or} is the residual oil saturation (refer to Table 6.1), and e_w is the water saturation exponent (assumed equal to 2).

The imbibition capillary pressure is given by the equation

$$p_{cow} = \frac{p_e}{(S_D)^{1/l}} \ , \tag{A.11}$$

where l is the pore size distribution index and p_e is the entry pressure.

Table 6.1 summarizes the specific rock-fluid properties associated with the hydrocarbon reservoir model considered in this dissertation.

Table A.1: Summary of the mass fractions for each phase of produced component used in the numerical simulations of reservoir dynamic behavior. Refer to equation A-1 for the formulation of the conservation of mass equations for each phase, and to the Nomenclature section for a definition of the variables listed in the table.

	PHASE		
COMPONENT	**Oleic**	**Gaseous**	**Aqueous**
Stock-tank oil	$w_{o,o} = \frac{r_o^{sc}}{r_o B_o}$	$w_{o,g} = 0$	$w_{o,w} = 0$
Produced gas	$w_{g,o} = \frac{r_g^{sc}}{r_o} \frac{R_s}{B_o}$	$w_{g,g} = 1$	$w_{g,w} = 0$
Produced brine	$w_{w,o} = 0$	$w_{w,g} = 0$	$w_{w,w} = 1$

Appendix B: Material Balance Calculations

We used material balance equations to estimate water influx and to confirm the producing mechanisms in the GNP2RB reservoir.

Walsh and Lake (2003) defined the equations necessary to calculate the drive mechanisms described in Figure 5.1 (refer to the Nomenclature page for a definition of the variables included in this Appendix):

$$I_{gd} = \frac{G_{fgi} E_g}{E_t} , \tag{B.1}$$

$$I_{sd} = \frac{N_{foi} E_o}{E_t} , \tag{B.2}$$

and

$$I_{nwd} = \frac{W_e}{E_t} , \tag{B.3}$$

where I_{gd}, I_{sd}, and I_{nwd} are the gas-cap drive, solution-gas drive, and natural water drive indices, respectively. The original surface gas in place is the sum of the resident gas in the free gas and oil phases. Therefore G_{fgi} is related to G by the equation

$$G_{fgi} = G - G_{foi} = G - N_{foi} R_{si} . \tag{B.4}$$

Analogously, the resident oil in the free oil phase is related to the original stock-tank oil in place by the equation

$$N_{foi} = N - N_{fgi} = N - G_{fgi} R_{vi} . \tag{B.5}$$

By rearranging terms in equations (B.4) and (B.5)

$$G_{fgi} = \frac{G - NR_{si}}{1 - R_{vi}R_{si}}, \tag{B.6}$$

and

$$N_{foi} = \frac{N - GR_{vi}}{1 - R_{vi}R_{si}}, \tag{B.7}$$

where G and N correspond to the original surface gas and oil in place, respectively. For the study under consideration, the volumetric estimates for G and N are 17.8 Bscf and 5.6 MMstb, respectively.

Moreover, R_{si} and R_{vi} are the corresponding initial solution gas-oil ratio and initial volatilized oil-gas ratio, respectively. Table B.1 summarizes the initial Pressure-Volume-Temperature (PVT) parameters used to perform material balance calculations.

The cumulative water influx (W_e) is a function of time that was calculated with the formula

$$W_e(t) = F(t) - G_{gfi}E_{gwf}(t) - N_{foi}E_{owf}(t), \tag{B.8}$$

where $F(t)$ is the net fluid withdrawal expressed in reservoir volume (i.e., RB) , and E_{gwf} and E_{owf} are the composite expansivities.

The generalized material balance equations can be summarized with the equation

$$F = G_p\left(\frac{B_{tg} - B_{to}R_v}{1 - R_v R_s}\right) + N_p\left(\frac{B_{to} - B_{tg}R_s}{1 - R_v R_s}\right) + W_p B_w\,, \tag{B.9}$$

where G_p, N_p and W_p are the cumulative gas, oil, and water production, respectively (refer to Figure 5.3). B_{tg}, B_{to}, and B_w are the total gas, total oil, and water formation volume factors, respectively. Also, R_s and R_v are the corresponding solution gas-oil ratio and volatilized oil-gas ratio, respectively (refer to Figure B.1 for description of the PVT parameters used in this dissertation).

The total gas, total oil, and water formation volume factor are defined by

$$B_{tg} = \frac{B_g(1 - R_{vi}R_s) + B_o(R_{vi} - R_v)}{(1 - R_s R_v)}\,, \tag{B.10}$$

and

$$B_{to} = \frac{B_o(1 - R_{si}R_v) + B_g(R_{si} - R_s)}{(1 - R_s R_v)}\,, \tag{B.11}$$

where B_g and B_o are the gas and oil formation volume factor, respectively (Figure B.1).

If the rock and water compressibilities are constant, the composite expansivities are defined by

$$E_{owf} = E_o + B_{oi}c_T\Delta p\,, \tag{B.12}$$

and

$$E_{gwf} = E_g + B_{gi}c_T\Delta p\,, \tag{B.13}$$

where E_o and E_g are the gas and oil expansivity, respectively. B_{gi} and B_{oi} are the initial gas and oil formation volume factor (Table B.1). In addition, Δp is the change in average pressure and c_T is the total or overall compressibility. The change in average pressure and the total compressibility are defined by

$$\Delta p = P_b - \overline{P}, \tag{B.14}$$

and

$$c_T = \frac{c_f + c_w S_{wi}}{1 - S_{wi}}, \tag{B.15}$$

respectively, where P_b designates the saturation pressure (also known as bubble pressure), $\overline{P}$ is the average pressure as the reservoir is depleted, c_f is the rock-formation compressibility, c_w is the water compressibility, and S_{wi} is the irreducible water saturation (refer to Table 6.1).

The gas, oil, and water expansivities are defined by

$$E_g = B_{tg} - B_{tgi}, \tag{B.16}$$

$$E_o = B_{to} - B_{toi}, \tag{B.17}$$

and

$$E_w = B_w - B_{wi}, \tag{B.18}$$

respectively.

By replacing the initial conditions in equations (B.10) and (B.11), we obtained the initial gas and oil formation volume factors as $B_{tgi} = B_{gi}$ and $B_{toi} = B_{oi}$, respectively.

Under the assumption of constant water and rock compressibilities, the total expansivity (E_t) is defined as

$$E_t = G_{fgi}E_g + N_{foi}E_o + \frac{\left(G_{fgi}B_{gi} + N_{foi}B_{oi}\right)}{\left(1 - S_{wi}\right)}\left(c_f + S_{wi}c_w\right)\Delta p + W_e - W_p B_w . \qquad \text{(B.19)}$$

The bottom panel of Figure 5.1 describes the calculated cumulative water influx (W_e) versus time. The time behavior of W_e can also be written

$$W_e(t) = \int_{t=0}^{t=t_t} q_e(t)dt \, , \qquad \text{(B.20)}$$

where $q_e(t)$ is the water influx flow-rate and t is time. Equation (B.20) shows that $W_e(t)$ exhibits a linear behavior with a zero-intercept at the origin. The slope of this line corresponds to the constant water influx flow-rate, $q_e(t)$, due to the external aquifer pressure. Such constant value of water influx flow rate is used in the form of an aquifer-recharge boundary condition to perform fluid-flow simulations in the GNP2RB reservoir described in this dissertation.

Table B.1: Summary of the Pressure-Volume-Temperature (PVT) parameters employed for the material balance calculations performed in the GNP2RB reservoir. Refer to Appendix B and to the Nomenclature section for a definition of the variables listed in the table.

PVT parameter and units	**Value**
Initial reservoir pressure, psia	3580
R_{si} , scf/stb	3176
R_{vi} , stb/MMscf	52
B_{oi} , rb/stb	2.84
B_{gi} , rb/Mscf	0.57
B_{wi} , rb/stb	1.02
Reservoir temperature, °F	189.5

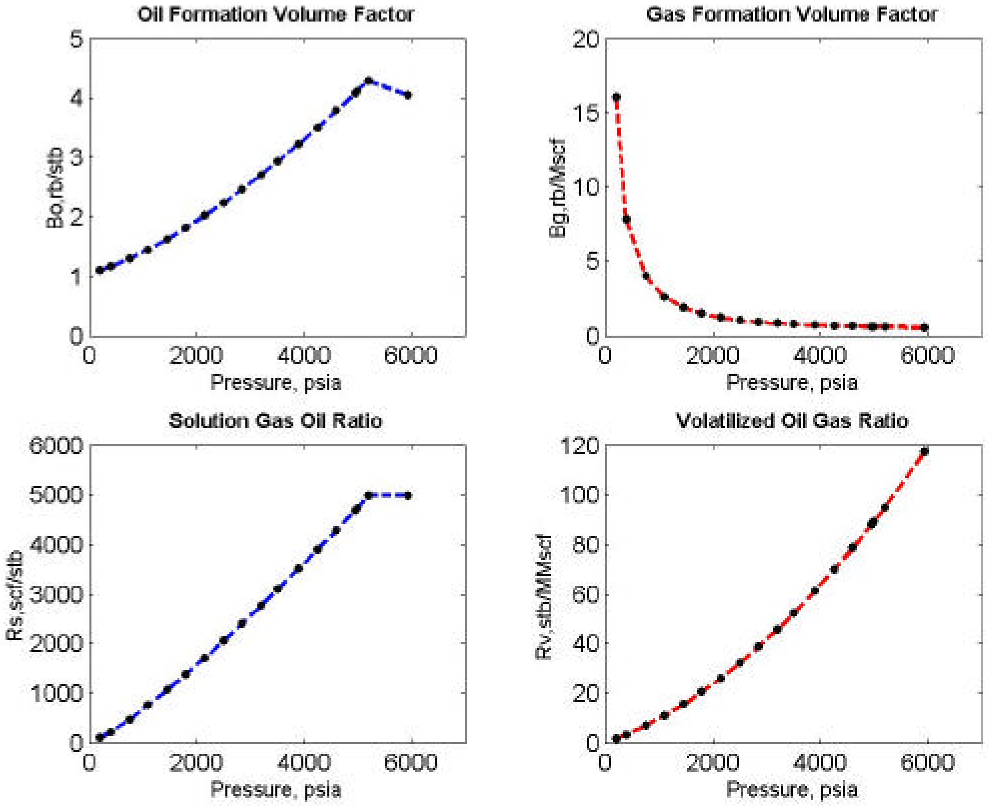

Figure B.1: Description of the PVT parameters as a function of pressure employed to perform material balance calculations in the GNP2RB reservoir. The curves describe oil formation volume factor (upper left panel), gas formation volume factor (upper right panel), dissolved gas-oil ratio (lower left panel), and volatilized oil-gas ratio (lower right panel). These PVT parameters were defined by correlation analysis (refer Appendix D).

Appendix C. Biot-Gassmann Fluid Substitution Analysis

Gassmann theory (Gassmann, 1951) is often used to calculate P- and S-wave velocities of gas- and oil-saturated rocks. The theory is strictly valid only at low frequencies (Mavko et al., 1996), and assumes that the porous rock is composed of a single, statistically homogeneous porous constituent, with single pore-space stiffness, and a single solid material. On the other hand, Biot's theory does cover the complete frequency range (Biot, 1956). Geertsma (1961) made a connection between the two theories by obtaining the low-frequency asymptote of Biot's equation. The final asymptotic solution described by Geertsma (1961) is the original equation proposed by Gassmann (1951). Results from Gassmann-Biot-Geertsma's (1951, 1956, 1961) work are summarized by the equations

$$V_p^2 = \left[k_b + \frac{4}{3} m_b + \frac{\left(1 - \frac{k_b}{k_s}\right)^2}{\frac{1}{k_s}\left(1 - f - \frac{k_b}{k_s}\right) + \frac{f}{k_f}} \right] \frac{1}{r} \ , \tag{C.1}$$

and

$$V_s^2 = \frac{m_b}{r} , \tag{C.2}$$

where V_p is compressional-wave velocity, V_s is shear-wave velocity, k_b is the dry rock bulk modulus, m_b is the dry rock bulk shear (rigidity) modulus, k_s is the solid mineral bulk modulus, k_f is the pore fluid bulk modulus, r is bulk density, and f is porosity.

The objective pursued by this Appendix is to calculate the sensitivity of both P- and S-wave velocities of reservoir sands to variations of porosity and water saturation. For reference, we consider a sand located at a depth of 9000 ft (measured depth along well A8) which is fully saturated with water. The measured P-wave velocity for this sand, V_P, is 9500 ft/s (2896 m/s), the calculated porosity is 27%, and the volumetric shale concentration is relatively low (20%). The itemized list below describes the step-by-step procedure used to calculate the dry-rock bulk modulus, the dry-rock rigidity modulus, and the pore bulk modulus, k_p (adapted from Tatham and McComack, 1991). Table C.1 is a summary of the input data required to perform such calculations for the specific case of the reference water-saturated sand, where the water, oil, and gas bulk modulus (k_w, k_o, and k_g), respectively, are estimated from Figure C.1.

(1) Calculation of fluid density (r_f):

$$r_f = S_w r_w + S_o r_o + S_g r_g , \tag{C.3}$$

(2) Calculation of bulk density (r):

$$r = f r_f + (1 - f) r_s , \tag{C.4}$$

(3) Calculation of the pore fluid bulk modulus (k_f):

$$\frac{1}{k_f} = \frac{S_w}{k_w} + \frac{S_o}{k_o} + \frac{S_g}{k_g} , \tag{C.5}$$

(4) Calculation of the elastic ratio:

$$X = 3\frac{(1-s)}{(1+s)}, \qquad \text{(C.6)}$$

(5) Calculation of the quantity:

$$M = V_P{}^2 r\,(929E^{-10}), \qquad \text{(C.7)}$$

(6) Calculation of the quantity:

$$A = X - 1, \qquad \text{(C.8)}$$

(7) Calculation of the expression:

$$B = fX\left(\frac{k_s}{k_f} - 1\right) - X + \frac{M}{k_s}, \qquad \text{(C.9)}$$

(8) Calculation of the quantity:

$$D = -f\left(X - \frac{M}{k_s}\right)\left(\frac{k_s}{k_f} - 1\right), \qquad \text{(C.10)}$$

(9) Calculation of the expression:

$$Y = \frac{\left[-B + (B^2 - 4AD)^{\frac{1}{2}}\right]}{2A}, \qquad \text{(C.11)}$$

(10) Calculation of the dry- rock bulk modulus (k_b):

$$k_b = (1-Y)k_s, \qquad \text{(C.12)}$$

(11) Calculation of the dry-rock shear (rigidity) modulus (m_b):

$$m_b = \frac{3}{4}k_b(X-1), \qquad \text{(C.13)}$$

and

(12) Calculation of the pore bulk modulus (k_p):

$$k_p = \frac{f}{\left(\frac{1}{k_b} - \frac{1}{k_s}\right)}. \tag{C.14}$$

Having calculated the pore bulk modulus for specific values of porosity and fluid saturation, the dry-rock modulus and the bulk density can be subsequently updated via equations (C.14), (C.13), and (C.4), to obtain the corresponding values of the elastic parameters for additional values of porosity and fluid saturation. The corresponding P- and S-wave velocities are then calculated using equations (C.1) and (C.2), respectively.

Subsequently, Poisson's ratio is calculated with the expression,

$$s = \frac{0.5R^2 - 1}{R^2 - 1}, \tag{C.15}$$

where

$$R = \frac{V_p}{V_s}\ . \tag{C.16}$$

Figures C.2 through C.4 consist on three panels, where the upper panel describes the calculated P- and S-wave velocities when the original fluid (water) filling the pore space is replaced with gas and oil. The mid panel shows the calculated P- and S-wave velocities when the water-saturated sand is replaced with an oil-saturated sand. Finally, the lower panels in Figures C.2 through C.4 show the calculated P- and S-wave velocities when the reference sand is fully saturated with water.

Figure C.2 describes the calculated P- and S-wave velocities as functions of water saturation for reservoir sands penetrated by well A8. The same figure shows the measured P- and S-wave velocities measured with the sonic borehole instrument as functions of water saturation. There is no significant difference between the plots shown in the upper and mid panels of Figure C.2, where the fluids saturating the pore space are gas-oil, and oil, respectively. Castagna and Backus (1993) mentioned that, for the case of gas-water mixtures, the introduction of a minor amount of gas causes a large decrease in the P-wave velocity. In addition, the presence of light oils (i.e. volatile oils) causes the P-wave velocity to decrease. Therefore, when these two fluids are present in the rock (condensate gas and volatile oil, as in the case of GNP2RB reservoir sands), the P-wave velocity will decrease regardless of the relative proportions in their saturation. By contrast, the plot shown in the lower panel of Figure C.2, defined for the case of full water-saturation, indicates that P-wave velocities will increase with an increase in gas saturation. The panels in Figure C.2 also indicate that S-wave velocities are not sensitive to variations in fluid saturation. This behavior is due to the fact that the S-wave velocity of porous rocks is primarily governed by the rigidity modulus, which remains independent of the type of pore fluid.

Figure C.3 shows plots of the calculated acoustic impedance as a function of water saturation, superimposed to acoustic impedances obtained by multiplying the measured well logs of P-wave velocity and bulk density. The behavior of acoustic impedance with respect to fluid saturation becomes clear when assuming that gas and oil are the fluids filling the pore space (upper panel), compared to only oil saturating the reservoir sand (mid panel). However, the range of variation for acoustic impedance with respect to variations in fluid saturation is relatively small. This is not the case when the reservoir sand is fully saturated with water, where acoustic impedance visibly increases with a decrease in water saturation.

Figure C.4, shows plots of Poisson's ratio versus water saturation. In that figure, the upper panel shows that when gas and oil are the saturating fluids, Poisson's ratio changes from 0.4 to 0.15 in two different ways: (a) volatilized oil makes Poisson's ratio to change from 0.4 to 0.24, and (b) presence of condensate-gas sands makes Poisson's ratio to remain constant at approximately 0.15. Therefore, gas sands entail a small decrease in Poisson's ratio below the calculated trend.

The mid panel in Figure C.4 describes the behavior of Poisson's ratio for the case of water-saturated sands, and when water is replaced with oil. In this case, Poisson's ratio varies from 0.4 to 0.24. Finally, the lower panel in Figure C.4, defined for the case of fully water-saturated sands, shows relatively high values of Poisson's ratio (0.4).

Although differences in fluid saturation in the GNP2RB reservoir cause only small changes in the magnitude of acoustic impedances, Poisson's ratio becomes a reliable indicator of the type of fluid saturating the reservoir sands.

Table C.1: Summary of the calculations performed on well-log data acquired in well A8, to estimate the dry-rock bulk modulus (k_b), the dry-rock rigidity modulus (m_b), and the pore bulk modulus, k_p, at the reference water saturation ($S_w = 1$). The values marked with an asterisk were taken from Figure C.1 (adapted from the work of Domenico, 1984).

Required Input	**Value**
Density of matrix solid [g/cm^3]	2.65
Density of water [g/cm^3]	1.1
Density of oil [g/cm^3]	0.8251
Bulk modulus of matrix [dyne/cm^2*10^{10}]	40
Bulk modulus of water [dyne/cm^2*10^{10}]	2.41*
Bulk modulus of oil [dyne/cm^2*10^{10}]	0.482*
Bulk modulus of gas [dyne/cm^2*10^{10}]	0.0383*
Dry rock poisson ratio [dimensionless]	0.12
Primary velocity [ft/s]	9500
Water saturation [fraction]	1.00
Porosity [fraction]	0.27
Computed Parameters:	
Shear-wave velocity [ft/s]	4579
Poisson's ratio [dimensionless]	0.36
Bulk modulus of dry rock [dyne/cm^2*10^{10}]	5.42
Rigidity of dry rock [dyne/cm^2*10^{10}]	5.52
Pore bulk modulus [dyne/cm^2*10^{10}]	1.69

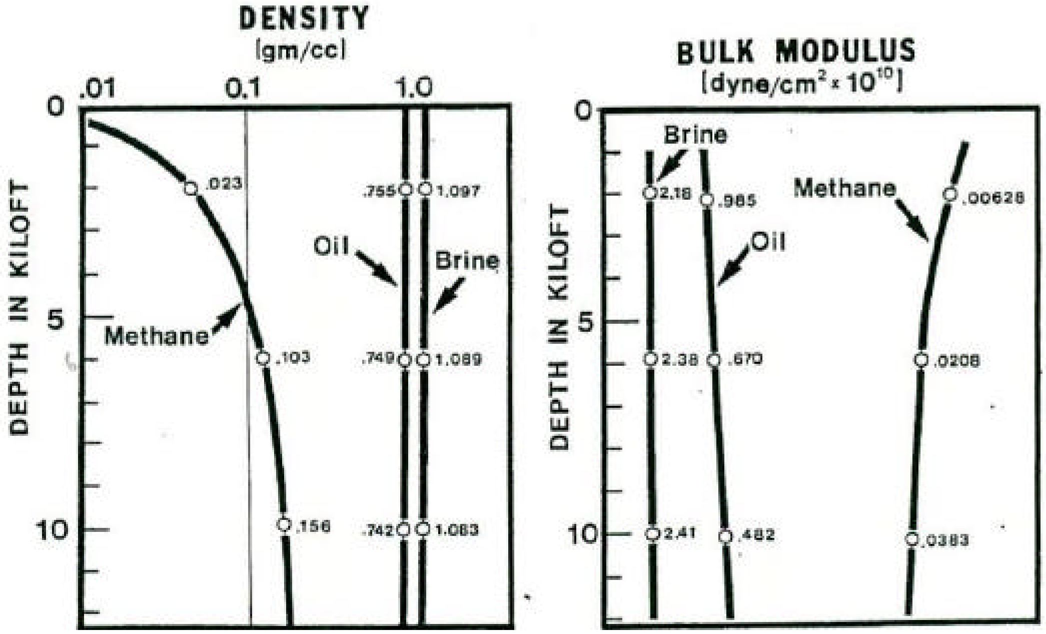

Figure C.1: Plots of hydrocarbon density and bulk modulus as a function of depth of burial for Tertiary, unconsolidated clastic sands [taken from Domenico (1984)].

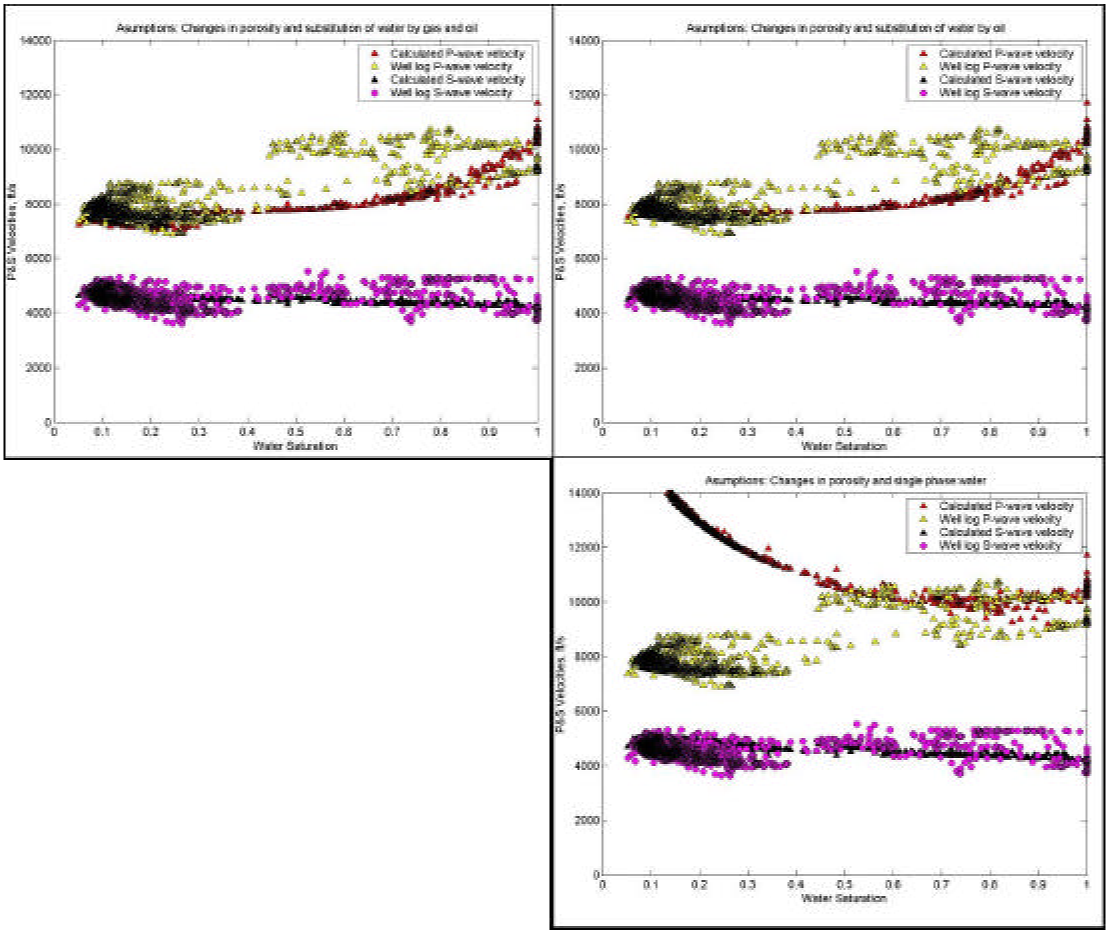

Figure C.2: P- and S-wave velocities as functions of water saturation. Red and black triangles describe the velocities calculated with equations (C.1) and (C.4) for a variety of porosity values within the GNP2RB reservoir. The yellow and magenta points describe well-log P- and S-wave velocities, respectively, for sands penetrated by wellA8 within the GNP2RB reservoir. The figure consists on three panels, where the upper panel shows the calculated velocities when the filling fluid (water) inside the pore space is replaced with gas and oil. The mid panel shows the calculated velocities when the filling fluid (water) inside the pore space is replaced with oil, and the lower panel shows the calculated velocities when the sand is fully saturated with water.

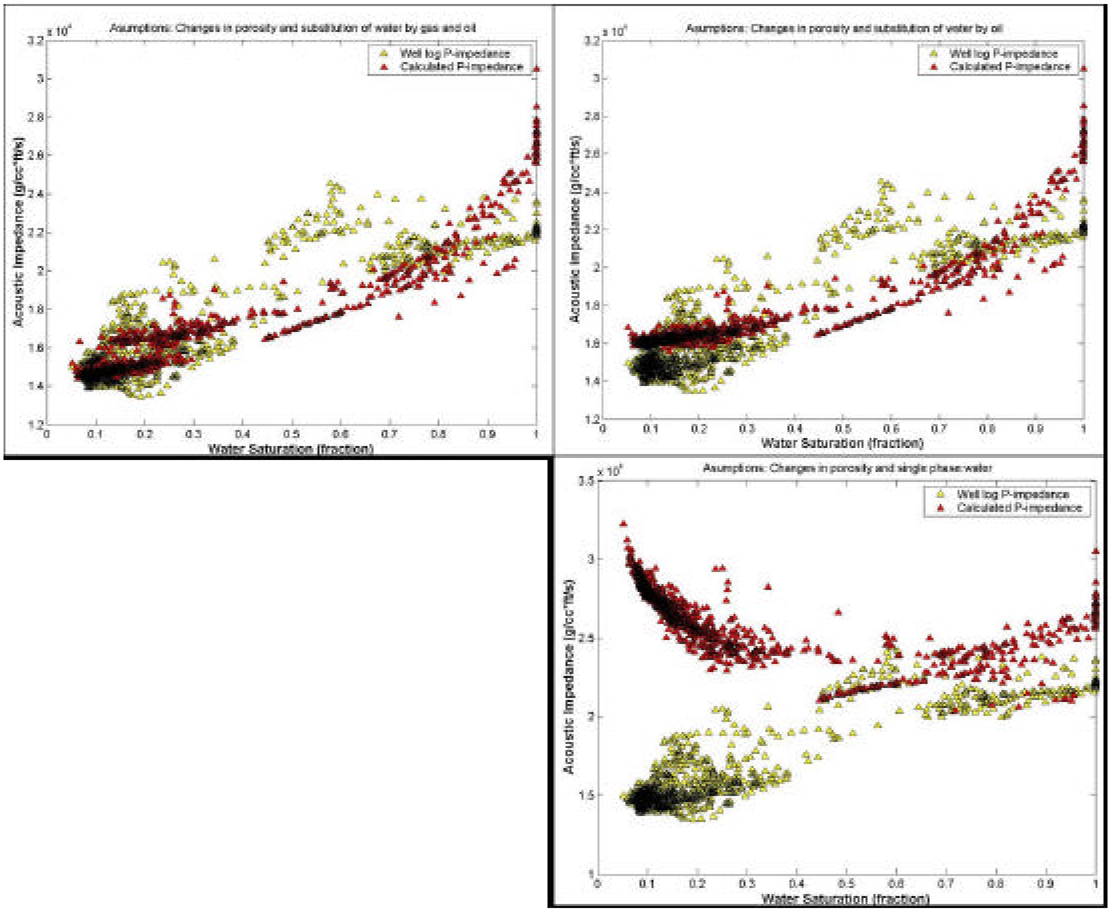

Figure C.3: Acoustic impedance as a function of water saturation. Red triangles describe the acoustic impedances calculated with equations (C.1) and (C.4) for a variety of porosity values within the GNP2RB reservoir. Yellow triangles describe the well-log impedances obtained by multiplying the measured well-log P-wave velocity and the measured bulk density for sands penetrated by wellA8 within the GNP2RB reservoir. The figure consists on three panels, where the upper panel shows the calculated impedances when the filling fluid (water) inside the pore space is replaced with gas and oil. The mid panel shows the calculated impedances when the filling fluid (water) inside the pore space is replaced with oil, and the lower panel shows the calculated impedances when the sand is fully saturated with water.

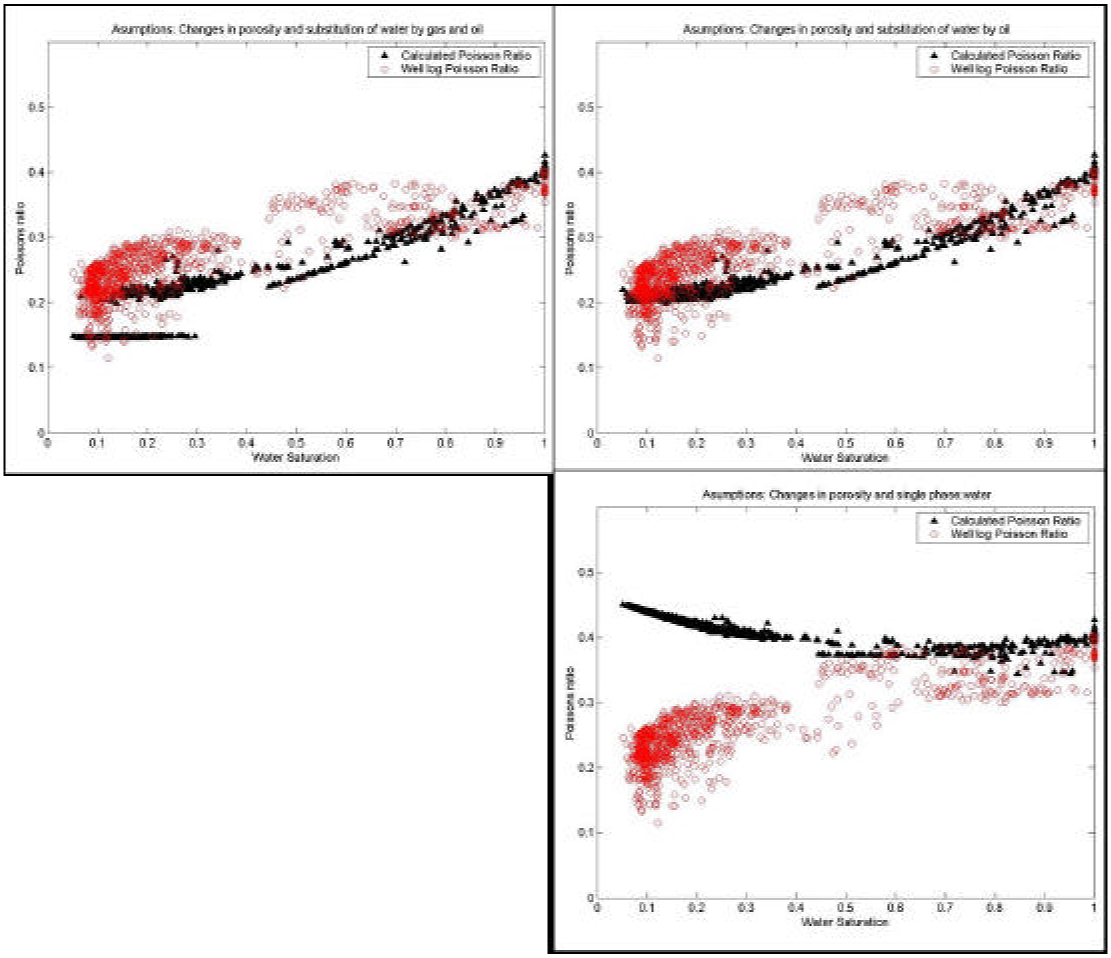

Figure C.4: Plot of Poisson's ratio as a function of water saturation. Black triangles describe Poisson's ratios calculated with equation (C.15) for a variety of porosity values within the GNP2RB reservoir, whereas the yellow dots describe Poisson's ratios calculated from measured well-log P-and S-wave velocities for sands penetrated by well A8 across the GNP2RB reservoir. The figure consists on three panels, where the upper panel describes the behavior of Poisson's ratio when the filling fluid (water) inside the pore space is replaced with gas and oil. The mid panel shows the behavior of Poisson's ratio when the filling fluid (water) inside the pore space is replaced with oil, and the lower panel describes the behavior of Poisson's ratio when the sand is fully saturated with water.

Appendix D. Pressure-Volume-Temperature Correlations

The fluids produced from the GNP2RB reservoir are a volatile oil, gas, and water. Because the composition of the volatile oil present in the GNP2RB reservoir is unknown, fluid correlations are used to approximate the PVT properties necessary to simulate fluid production. For instance, gas-oil ratios, also named dissolved gas-oil ratios can be estimated using correlations of oil properties. The gas-oil ratios is the amount of gas that evolves from the oil as the latter is transported from the reservoir to surface conditions (McCain, 1990). Volatile-oil reservoirs are associated with large produced gas-oil ratios because of the large dissolved-gas content of volatile oils.

In this dissertation, the Standing (1947) correlation is used to approximate the dissolved gas-oil ratio, R_s, to the observed values of production gas-oil ratio (GOR). The correlation is given by

$$R_s = g_g \left(\frac{P}{18*10^{y_g}} \right)^{1.204} \qquad (P \le P_b), \qquad \text{(D.1)}$$

where P_b is the bubble-point pressure (3580 psia), g_g is a dimensionless parameter that represents the gas gravity (air=1.0), y_g is the mole fraction of gas, P is reservoir pressure measured in psia, and R_s is the estimated dissolved gas-oil ratio in the units of scf/stb. The mole fraction of gas is given by the expression

$$y_g = 0.00091T - 0.0125 g_{API}, \qquad \text{(D.2)}$$

where, T is the reservoir temperature (186 °F) and $g_{API} = 40$ is the American

Petroleum Institute oil gravity.

On the other hand, the volatilized oil-gas ratio, R_v, also called the condensate-gas ratio (Walsh and Lake, 2003), depends on the molecular weights of the reservoir fluids (gas and oil). Fluid composition is unknown; however, reference values from neighboring areas were available and sensitivity analyses were performed to assess the reliability of PVT parameters (Figure D.1).

Similarly, the oil, gas, and water formation volume factors are approximated by the equation

$$B_o = 0.972 + 0.000147F^{1.175} \qquad (P \le P_b), \qquad \text{(D.3)}$$

where B_o is the oil formation volume factor, measured in rb/stb, and the correlating factor F is given by the formula

$$\text{F} = R_s(g_g / g_{osc})^{0.5} + 1.25T, \qquad \text{(D.4)}$$

where g_{osc} is the oil gravity at standard conditions, i.e.,

$$g_{osc} = \frac{141.5}{g_{API} + 131.5}. \qquad \text{(D.5)}$$

The gas formation volume factor is defined by (McCain, 1990)

$$B_g = \frac{0.005035Tz}{P}, \qquad \text{(D.6)}$$

where z is the gas-phase deviation factor. This factor is estimated from the Standing-Katz (1942) correlation chart. There are a number of generic equations that have been developed for computer applications. Standing (1977) describes the following non-iterative equation:

$$z = a + (1-a)\exp^{-b} + cP_{pr}{}^{d}\,, \tag{D.7}$$

where

$$a = 1.39\sqrt{T_{pr} - 0.92} - 0.36T_{pr} - 0.101\,, \tag{D.8}$$

$$b = [0.62 - 0.23T_{pr}]P_{pr} + \left[\frac{0.066}{T_{pr} - 0.86} - 0.037\right]P_{pr}^{2} + \frac{0.32}{10^{9(T_{pr}-1)}}P_{pr}^{6}\,, \tag{D.9}$$

$$c = 0.132 - 0.32\log_{10}(T_{pr})\,, \tag{D.10}$$

and

$$d = 10^{(0.3106 - 0.49T_{pr} + 0.1824T_{pr}^{2})}\,. \tag{D.11}$$

In the above equations, $P_{pr} = P / P_{pc}$ and $T_{pr} = (T + 460)/T_{pc}$ are called the pseudo-reduced pressure and temperature, respectively. When the fluid composition is unknown (Miller, 2000), pseudo-critical properties can be estimated from the equations

$$P_{pc} = 677 + 15g_{g} - 37.5g_{g}^{2}\,, \tag{D.12}$$

and

$$T_{pc} = 168 + 325g_{g} - 12.5g_{g}^{2}\,. \tag{D.13}$$

Finally, the water formation volume factor is defined by (McCain, 1990)

$$B_{w} = B_{wp}\frac{B_{w}}{B_{wp}}\,, \tag{D.14}$$

where

$$B_{wp} = A_{1} + A_{2}P + A_{3}P^{2}\,, \tag{D.15}$$

$$A_{1} = 0.9947 + 5.8E^{6}T + 1.02E^{6}T^{2}\,, \tag{D.16}$$

$$A_2 = -4.2E^{6} + 1.83E^{8}T - 6.77E^{11}T^{2}\,, \tag{D.17}$$

$$A_3 = 1.3E^{10} - 1.385E^{12}T + 4.285E^{15}T^{2}\,, \tag{D.18}$$

$$\frac{B_w}{B_{wp}} = 1 + \frac{C_w}{10000}\left[5.1E^{-8}P + B_1 - B_2\right], \tag{D.19}$$

$$B_1 = (5.47E^{-6} - 1.95E^{-10}P)(T - T_s)\,, \tag{D.20}$$

and

$$B_2 = (3.23E^{-8} - 8.5E^{-13}P)(T - T_s)^{2}\,, \tag{D.21}$$

where T_s is the surface temperature (87 °F) and C_w is the salt concentration of formation water (230,000 ppm).

The oil viscosity is estimated using the Beggs and Robinson's (1975) correlations following a two-step procedure: the gas-free oil viscosity is first estimated, followed by the gas-saturated oil viscosity. This procedure is summarized by the equations

$$\log\left[\log\left(m_{oD} + 1\right)\right] = 1.8653 - 0.025086g_{API} - 0.5644\log T\,, \tag{D.22}$$

$$m_o = Am_{oD}^{B}\,, \tag{D.23}$$

$$A = 10.715(R_s + 100)^{-0.515}\,, \tag{D.24}$$

and

$$B = 5.44(R_s + 150)^{-0.338}\,, \tag{D.25}$$

where, m_{oD} and m_o are gas-free oil viscosity at standard conditions and the gas-saturated oil viscosity, respectively, both measured in centipoises.

The gas viscosity, m_g, was estimated using Lee et al.'s (1966) procedure, which is summarized by the formulas

$$m_g = 10^{-4} A \exp(B \hat{r}_g^C) , \qquad \text{(D.26)}$$

$$A = \frac{(9.379 + 0.01607 M_{wg}) T^{1.5}}{209.2 + 19.26 M_{wg} + T} , \qquad \text{(D.27)}$$

$$B = 3.448 + \frac{986.4}{T} + 0.01009 M_{wg} , \qquad \text{(D.28)}$$

and

$$C = 2.447 - 0.2224 B , \qquad \text{(D.29)}$$

where $M_{wg} = 28.966 g_g$ is the molecular weight of gas and $\hat{r}_g = PM_{wg} / zRT$ is mass density.

Finally, the water viscosity was estimated with the formula (McCain, 1990)

$$m_w = \exp(1.003 - 0.01479T + 0.00001982T^2) . \qquad \text{(D.30)}$$

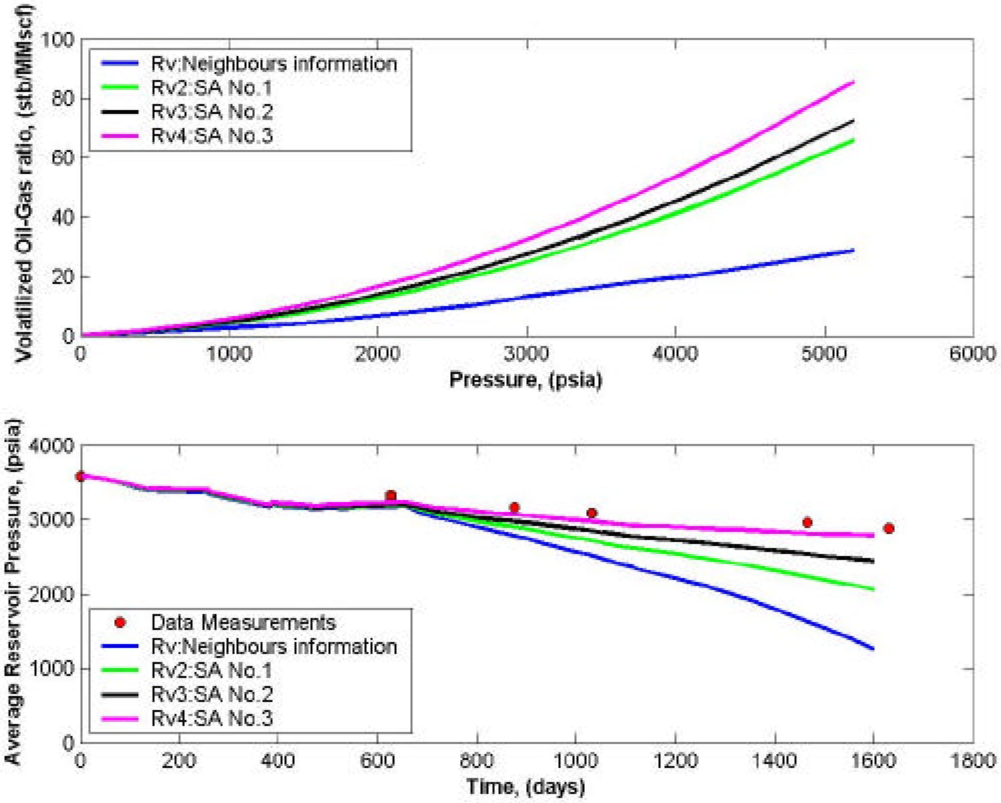

Figure D.1: Graphical description of the estimation of the volatilized oil-gas ratio. The top panel shows the volatilized oil-gas ratio as a function of pressure. The bottom panel compares the simulated average reservoir pressure against the measured time records of pressure. Due to the unknown composition of the volatile oil present in the GNP2RB reservoir, sensitivity analyses (SA) were performed to study the effect of the volatilized oil-gas ratio on the simulated pressure. The blue solid line in both panels designates data available from neighboring areas, while the red dots describe the actual time records of reservoir pressure.

Nomenclature

B_o = Oil formation volume factor [L^3/L^3]
B_g = Gas formation volume factor [L^3/L^3]
B_w = Water formation volume factor [L^3/L^3]
B_{to} = Total oil formation volume factor [L^3/L^3]
B_{tg} = Total gas formation volume factor [L^3/L^3]
c_T = Total compressibility [Lt^2/m]
c_f = Formation compressibility [Lt^2/m]
c_w = Water compressibility [Lt^2/m]
E_g = Gas expansivity [L^3/L^3]
E_o = Oil expansivity [L^3/L^3]
E_w = Water expansivity [L^3/L^3]
E_t = Total expansivity [L^3/L^3]
E_{gwf}, E_{owf} = Composite expansivities [L^3/L^3]
e_o = Oil saturation exponent [dimensionless]
e_g = Gas saturation exponent [dimensionless]
e_w = Water saturation exponent [dimensionless]
F = Net fluid withdrawal [L^3]
G = Gas in place [L^3]
G_p = Cumulative gas production [L^3]
G_{fgi} = Resident gas in the free gas phase [L^3]
$GR_{\min}$ = Minimum value obtained from the Gamma Ray log [gAPI]
$GR_{\max}$ = Maximum average value obtained from the Gamma Ray log [gAPI]
g = Gravitational acceleration term [L/t^2]
g_c = Unit converter parameter [mL/Ft^2]
I_{gd} = Gas-cap drive index [fraction]
I_{sd} = Solution-gas drive index [fraction]
I_{nwd} = Natural water drive index [fraction]
$\vec{\vec{k}}$ = Absolute permeability tensor [L^2]
k_b = Dry rock bulk modulus [m/Lt^2]
k_s = Solid mineral bulk modulus [m/Lt^2]

k_f = Pore fluid bulk modulus [m/Lt^2]
k_p = Pore bulk modulus [m/Lt^2]
k_g = Gas bulk modulus [m/Lt^2]
k_o = Oil bulk modulus [m/Lt^2]
k_w = Water bulk modulus [m/Lt^2]
k_{ra} = Relative permeability of each phase [L^2/ L^2]
k_{rg} = Gas relative permeability [L^2/ L^2]
k_{rog} = Oil-gas relative permeability [L^2/ L^2]
k_{rg}^o = Gas end-point relative permeability [L^2/ L^2]
k_{ro}^o = Oil end-point relative permeability [L^2/ L^2]
k_{rw} = Water relative permeability [L^2/ L^2]
k_{row} = Oil-water relative permeability [L^2/ L^2]
k_{rw}^o = Water end-point relative permeability [L^2/ L^2]
$n(t)$ = Additive noise
N = Oil in place [L^3]
N_p = Cumulative oil production [L^3]
N_{foi} = Resident oil in the free oil phase [L^3]
p_e = Entry pressure [m/Lt^2]
$\overline{P}$ = Average pressure [m/Lt^2]
P_b = Saturation pressure (Bubble pressure) [m/Lt^2]
P_{cow} = Water-oil capillary pressure [m/Lt^2]
P_{cgo} = Gas-oil capillary pressure [m/Lt^2]
q_e = Water influx flowrate [L^3/t]
$r(t)$ = Reflection coefficient [L/t*m/L^3]
R_s = Solution gas-oil ratio [L^3/L^3]
R_v = Volatilized oil-gas ratio [L^3/L^3]
R = Source/sink term [L^3]
R_{wa} = Apparent water resistivity [ohm-m]
R_w = Water resistivity [ohm-m]
R_t = Deep resistivity in front of a sand [ohm-m]
$R_t(ws)$ = Deep resistivity in front of a water sand [ohm-m]
R_{sh} = Shale resistivity [ohm-m]
$s(t)$ = Post-stack seismic trace sampled at a constant time interval

S = Fluid saturation [L^3/L^3]
S_{gc} = Critical gas saturation [L^3/L^3]
S_{wi} = Irreducible water saturation [L^3/L^3]
S_D = Normalized saturation [L^3/L^3]
S_w = Water saturation [L^3/L^3]
S_o = Oil saturation [L^3/L^3]
S_g = Gas saturation [L^3/L^3]
S_{or} = Residual oil saturation [L^3/L^3]
T = Reservoir Temperature
$\vec{u}$ = Interstitial velocity [L/t]
$\vec{V}$ = Average P-wave velocity [L/t]
V_{sh} = Volumetric concentration of shale [fraction]
V_p = P-wave velocity [L/t]
V_s = S-wave velocity [L/t]
W_e = Cumulative water influx [L^3]
W_p = Cumulative water production [L^3]
$w(t)$ = Scaled wavelet
$Z_p(t)$ = Acoustic impedance [m/V*L/t]

Greek Symbols

Δh = Depth sampling interval [L]
Δt = Time sampling interval [t]
$\vec{\nabla} D_z$ = Direction of fluid-flow [L]
$\vec{\nabla} p$ = Pressure gradient [m/L^2t^2]
f = Porosity [L^3/L^3]
$f\,(ws)$ = Porosity in front of a water sand [L^3/L^3]
$f_N(sh)$ = Neutron average porosity across shales [L^3/L^3]
$f_D(sh)$ = Density average porosity across shales [L^3/L^3]
m_a = Viscosity of each fluid phase [mL/t]
m_b = Dry rock bulk shear modulus [m/Lt^2]
g_a = Specific weight of the fluid [$m/L^2\ t^2$]
s = Poisson ratio [dimensionless]

r = Fluid density [m/L^3]
r_b = Bulk density [m/L^3]
r_{ma} = Matrix density [m/L^3]
r_{sh} = Shale density [m/L^3]
r_w = Water density [m/L^3]
r_o = Oil density [m/L^3]
r_g = Gas density [m/L^3]
g, a , and b = Regression parameters [dimensionless]
l = Pore size distribution index [dimensionless]
$w_{o,o}$ = Oil mass fraction present in the oil phase [dimensionless]
$w_{o,g}$ = Oil mass fraction present in the gas phase [dimensionless]
$w_{o,w}$ = Oil mass fraction present in the water phase [dimensionless]
$w_{g,o}$ = Gas mass fraction present in the oil phase [dimensionless]
$w_{g,g}$ = Gas mass fraction present in the gas phase [dimensionless]
$w_{g,w}$ = Gas mass fraction present in the water phase [dimensionless]
$w_{w,o}$ = Water mass fraction present in the oil phase [dimensionless]
$w_{w,g}$ = Water mass fraction present in the gas phase [dimensionless]
$w_{w,w}$ = Water mass fraction present in the water phase [dimensionless]

Superscripts

i = Initial conditions
sc = Standard conditions
(t) = Time domain

References

Al-Najjar, N., Brevik, I., Psaila, D., and Doyen, P., 1999, 4D seismic modeling of the Statfjord field: Initial results: SPE No. 56730 presented at the Annual Technical Conference and Exhibition held in Houston, Texas.

Balan, B., Mohaghegh, S., and Ameri, S., 1995, State-of-the-art in permeability determination from well log data: Part-1 a comparative study, model development: SPE No. 30978 presented at the Eastern Regional Conference and Exhibition, Morgantown, West Virginia.

Bashore, W., Araktingi, U., Levy M., and Schweller W., 1993, The importance of the geological model for reservoir characterization using geostatistical techniques and the impact on subsequent fluid flow: SPE No. 26474 presented at the 68th Annual Technical Conference and Exhibition of the Society of Petroleum Engineers held in Houston, Texas.

Bassiouni, Z., 1994, Theory, measurement, and interpretation of well logs: SPE Textbook Series Vol. 4.

Beggs, H. and Robinson, J., 1975, Estimating the viscosity of crude oil systems: JPT, **9**, 1140-1142.

Biot, M., 1956, The theory of propagation of elastic waves in fluid-saturated solids, I lower frequency range, II higher frequency range: J. Acoust. Soc. Am., **107**, 3018-3027.

Box, G., Jenkins G., and Reinsel, G., 1994, Time Series Analysis: Prentice Hall.

Castagna, J. and Backus, M., 1993, Offset dependent reflectivity- theory and practice of AVO analysis: Society of Exploration Geophysicists.

Debeye, H., and Van Riel, P., 1990, Lp-norm deconvolution: Geophysical Prospecting, **38**, 381-403.

Debeye, H., Sabbah, E., and Van der Made, P., 1996, Stochastic inversion: SEG 66 Annual International Meeting held in Denver, Colorado.

Deutsch, C., and Journel, A., 1998, GSLIB, Geostatistical Software Library and User's Guide: Oxford University Press.

Domenico, S., 1984, Rock lithology and porosity determination from shear and compressional wave velocity: Geophysics, **49**, 1188-1195.

Doyen, P., 1988, Porosity from seismic data: A geostatistical approach: Geophysics, **53**, 1263-1275.

Dykstra, H., and Parsons, R., 1950, The prediction of oil recovery by waterflood: Secondary recovery of oil in the United States, principles and practice, 2nd Edition, American Petroleum Institute, 160-174.

Gambús, M., and Torres-Verdín, C., 2002, High-resolution geostatistical inversion of a 3D seismic data set acquired in a Gulf of Mexico gas field: 72nd Annual Technical Conference and Exhibition , SEG, Expanded Abstracts.

Gassmann, F., 1951, Elastic waves through a packing of spheres: Geophysics, **16**, 673-685.

Geertsma, J., 1961, Velocity-log interpretation: The effect of rock bulk compressibility: Soc. Pet. Eng., **1**, 235-248.

Grijalba-Cuenca, A., Torres-Verdín, C., and Debeye, H., 2000, Geostatistical inversion of 3D seismic data to extrapolate wireline petrophysical variables laterally away from the well: SPE No. 63283 presented at the Annual International Technical Conference, Dallas, Texas.

Haas, A., and Dubrule, O., 1994, Geostatistical inversion: a sequential method for stochastic reservoir modeling constrained by seismic data: First Break, **12**, 561-569.

Journel, A., and Huijbregts, C., 1978, Mining Geostatistics: Academic Press Inc.

Kelkar, M., and Huang, X., 1996, Reservoir characterization by integration of seismic and dynamic data: SPE/DOE No. 35415 presented at the Tenth Symposium on Improved Oil Recovery held in Tulsa, Oklahoma.

Lake, L., and Carroll, H., 1986, Reservoir Characterization: Academic Press Inc.

Landa, J., and Horne, R., 1997, A procedure to integrate well test data, reservoir performance history and 4-D seismic information into a reservoir description: SPE No. 38653 presented at the SPE Annual Technical Conference and Exhibition held in San Antonio, Texas.

Landa, J., and Guyaguler, B., 2003, A methodology of history matching and the assessment of uncertainties associated with flow prediction: SPE No. 84465 presented at the SPE Annual Technical Conference and Exhibition held in Denver, Colorado.

Lee, A., Gonzalez, M., and Eakin, B., 1966, The Viscosity of Natural Gases: Trans. AIME, **237**, 997-1000.

Lortzer, G., and Berkhout, A., 1992, An integrated approach to lithologic inversion – Part1: Geophysics, **57**, 233-245.

Maureau, G., and Van Wijhe, D., 1979, The prediction of porosity in the Permian carbonate of eastern Netherlands using seismic data: Geophysics, **44**, 1502-1517.

Mavko, G., Mukerji, T., and Dvorkin, J., 1996, Rock Physics Handbook: Stanford University.

McCain, W., 1990, The Properties of Petroleum Fluids: PennWell.

Merkel, R., Barree, R., and Towle, G., 2001, Seismic response of Gulf of Mexico reservoir rocks with variations in pressure and water saturation: The Leading Edge, **20**, 290-299.

Miller, M., 2000, Advanced reservoir course: Lecture notes: Department of Petroleum and Geosystems Engineering, The University of Texas at Austin.

Montgomery, D., 1991, Introduction to Statistical Quality Control: John Wiley and Sons.

Oldenburg, D., Scheuer, T., and Levy, S., 1983, Recovery of the acoustic impedance from reflection seismograms: Geophysics, 4**8**, 1318-1330.

Pendrel, J., and Van Riel, P., 1997, Estimating porosity from 3D seismic inversion and 3D geostatistics: Presernted at the 67th Annual International Meeting, SEG.

Standing, M., and Katz, D., 1942, Density of natural gases: Trans. AIME, **146**, 140-144.

Standing, M., 1947, A Pressure-Volume-Temperature correlation for mixtures of California oils and gases: Drill. and Prod. Prac., API.

Standing, M., 1977, Volumetric and phase behavior of oil field hydrocarbon systems: Society of Petroleum Engineers, Richardson, Texas.

Tatham, R., and McComack, M., 1991, Multicomponent seismology in petroleum exploration: SEG Publication.

Torres-Verdín, Victoria, M., Merletti, G., and Pendrel, J., 1999, Trace-based and geostatistical inversion of 3D seismic data for thin-sand delineation: An application to San Jorge Basin, Argentina: The Leading Edge, **18**, 1070-1076.

Varela, O., Torres-Verdín, C., and Lake L., 2002, Assessing the value of 3D seismic data in reducing uncertainty in reservoir production forecasts: SPE No. 77359 presented at the SPE Annual Technical Conference and Exhibition, San Antonio, Texas.

Waggoner, J., Cominelli, A., and Seymour, R., 2002, Improved reservoir modeling with time-lapse seismic in a Gulf of Mexico gas condensate reservoir: SPE No. 77514 presented at the SPE Annual Technical Conference and Exhibition held in San Antonio, Texas.

Walsh, P., and Lake, L., 2003, A Generalized Approach to Primary Hydrocarbon Recovery: Elsevier Publication.

Vita

Maika Karen Gambús Ordaz was born in Maracaibo, state of Zulia, Venezuela, on July 22nd, 1972, the daughter of Mr. Jorge Eliecer Gambús and Mrs. Angela Graciela Ordaz. She received the degree of Petroleum Engineer from La Universidad del Zulia in 1994 and a Master of Science degree in Petroleum Engineering from La Universidad del Zulia in 1998. She has one year of industry experience with the Venezuelan National Oil Company (PDVSA, 1994-1995) working as a reservoir engineer. She worked as a lecturer for La Universidad del Zulia during the following four years (1995-1999). She began graduate studies at the University of Texas at Austin during the Fall 1999.

In July 1999, she married Rafael Hernández from Punto Fijo, state of Falcón, Venezuela.

Permanent address: Urbanización La Rotaria. Avenida 81G No. 83-08
Cuarta etapa, Maracaibo, Zulia, Venezuela.

This dissertation was typed by the author.